CARBON DIOXIDE ADSORPTION BY NaOH IMPREGNATED ACTIVATED CARBON FROM LONGAN FRUIT SEED AND THE ADAPTIVE SAMPLING APPROACH FOR PROCESS SIMULATION-BASED OPTIMIZATION

PRAPATSORN BORISUT

A Thesis Submitted in Partial Fulfillment of the Requirements for the Degree of Doctor of Philosophy in Mechanical and Process System Engineering
Suranaree University of Technology
Academic Year 2023

การดูดซับคาร์บอนไดออกไซด์โดยถ่านกัมมันต์จากเมล็ดลำไยจุ่มแช่โซเดียมไฮดรอกไซด์และวิธีการสุ่มตัวอย่างแบบปรับสำหรับการหาค่าที่เหมาะสมที่สุดบนการจำลองกระบวนการ

นางสาวประภัสสร บริสุทธิ์

มหาวิทยาลัยเทคโนโลยีสุรนารี

วิทยานิพนธ์นี้เป็นส่วนหนึ่งของการศึกษาตามหลักสูตรปริญญาวิศวกรรมศาสตรดุษฎีบัณฑิต
สาขาวิชาวิศวกรรมเครื่องกลและระบบกระบวนการ
มหาวิทยาลัยเทคโนโลยีสุรนารี
ปีการศึกษา 2566

CARBON DIOXIDE ADSORPTION BY NaOH IMPREGNATED ACTIVATED CARBON FROM LONGAN FRUIT SEED AND THE ADAPTIVE SAMPLING APPROACH FOR PROCESS SIMULATION-BASED OPTIMIZATION

Suranaree University of Technology has approved this thesis submitted in partial fulfillment of the requirements for the Degree of Doctor of Philosophy.

Thesis Examining Committee

(Asst. Prof. Dr. Ratanawan Kiattikomol)
Chairperson

(Dr. Aroonsri Nuchitprasittichai)
Member (Thesis Advisor)

(Prof. Dr. Chaiyot Tangsathitkulchai)
Member

(Assoc. Prof. Dr. Atichat Wongkoblap)
Member

(Assoc. Prof. Dr. Lek Wantha)
Member

(Assoc. Prof. Dr. Yupaporn Ruksakulpiwat)
Vice Rector for Academic Affairs
and Quality Assurance

(Assoc. Prof. Dr. Pornsiri Jongkol)
Dean of Institute of Engineering

มหาวิทยาลัยเทคโนโลยีสุรนารี

ประภัสสร บริสุทธิ์ : การดูดซับคาร์บอนไดออกไซด์โดยถ่านกัมมันต์จากเมล็ดลำไยจุ่มแช่โซเดียมไฮดรอกไซด์และวิธีการสุ่มตัวอย่างแบบปรับสำหรับการหาค่าที่เหมาะสมที่สุดบนการจำลองกระบวนการ (CARBON DIOXIDE ADSORPTION BY NaOH IMPREGNATED ACTIVATED CARBON FROM LONGAN FRUIT SEED AND THE ADAPTIVE SAMPLING APPROACH FOR PROCESS SIMULATION-BASED OPTIMIZATION)
อาจารย์ที่ปรึกษา : อาจารย์ ดร.อรุณศรี นุชิตประสิทธิชัย, 206 หน้า.

คำสำคัญ: การดูดซับ/คาร์บอนไดออกไซด์/ถ่านกัมมันต์/เทคนิคการเลือกกลุ่มตัวอย่าง/การหาค่าที่เหมาสมที่สุด/การออกแบบการทดลอง

วิทยานิพนธ์ฉบับนี้ศึกษาประสิทธิภาพการดูดซับคาร์บอนไดออกไซด์ด้วยถ่านกัมมันต์และการพัฒนาเทคนิคการเลือกกลุ่มตัวอย่างเพื่อใช้ในการออกแบบการทดลอง งานวิจัยถูกแบ่งออกเป็นสี่ส่วน โดยในส่วนที่หนึ่งเป็นการศึกษาประสิทธิภาพการดูดซับคาร์บอนไดออกไซด์ในเบดนิ่งด้วยถ่านกัมมันต์ที่มีขนาดของรูพรุนแตกต่างกันที่สังเคราะห์มาจากเมล็ดลำไย และมีการจุ่มแช่ในสารละลายโซเดียมไฮดรอกไซด์ โดยการทดลองการดูดซับในเบดนิ่งมีการพิจารณาตัวแปรที่ส่งผลต่อประสิทธิภาพการดูดซับประกอบไปด้วย ชนิดของถ่านกัมมันต์ ซึ่งแสดงค่าเป็นสัดส่วนโดยปริมาตรของรูพรุนขนาดเล็กต่อรูพรุนขนาดกลาง อุณหภูมิการดูดซับ น้ำหนักของโซเดียมไฮดรอกไซด์ต่อน้ำหนักของถ่านกัมมันต์ อัตราการไหลของแก๊สขาเข้าคอลัมน์เบดนิ่ง และปริมาณของถ่านกัมมันต์ ผลการศึกษาพบว่าน้ำหนักของโซเดียมไฮดรอกไซด์ต่อน้ำหนักของถ่านกัมมันต์แสดงค่าที่เหมาะสมที่สุดเพื่อให้ได้มาซึ่งค่าที่สูงที่สุดของตัวแปรเบรกทรู ปริมาณการดูดซับคาร์บอนไดออกไซด์เพิ่มขึ้นร้อยละ 45 เมื่อใช้ถ่านกัมมันต์ที่มีการจุ่มแช่สารละลายโซเดียมไฮดรอกไซด์ความเข้มข้นร้อยละหนึ่ง สภาวะการทดลองที่ใช้ถ่านกัมมันต์ที่มีสัดส่วนโดยปริมาตรของรูพรุนขนาดเล็กต่อรูพรุนขนาดกลางเท่ากับ 2.83 อุณหภูมิการดูดซับเท่ากับ 20 องศาเซลเซียส น้ำหนักของโซเดียมไฮดรอกไซด์ต่อน้ำหนักของถ่านกัมมันต์เท่ากับ 76.5 มิลลิกรัมต่อกรัม อัตราการไหลของแก๊สขาเข้าคอลัมน์เบดนิ่งเท่ากับ 156 กิโลกรัมต่อชั่วโมงต่อตารางเมตร และปริมาณของถ่านกัมมันต์เท่ากับ 51 กิโลกรัมต่อตารางเมตร ให้ค่าการดูดซับที่เวลาเบรกทรูสูงที่สุดเป็น 33.58 มิลลิกรัมต่อกรัม

สำหรับงานในส่วนที่สอง ศึกษาการดูดซับคาร์บอนไดออกไซด์ของถ่านกัมมันต์สี่ชนิด โดยแบ่งเป็นถ่านกัมมันต์ที่มีรูพรุนส่วนใหญ่เป็นรูพรุนขนาดเล็กสองชนิดและถ่านกัมมันต์ที่มีรูพรุนขนาดใหญ่กว่าอีกสองชนิด โดยทำการดูดซับที่ความดันมากกว่าความดันบรรยากาศ ที่อุณหภูมิ 0 องศาเซลเซียส และศึกษาความเข้มข้นของสารละลายโซเดียมไฮดรอกไซด์ที่ใช้จุ่มแช่ถ่านกัมมันต์ทั้งสี่ชนิดที่ความเข้มข้นของสารละลายแตกต่างกัน ประกอบไปด้วยความเข้มข้นร้อยละ 1, 4, 7, 10, และ 13

จากผลของพื้นที่เบทพบว่าพื้นที่เบทลดลงเมื่อความเข้มข้นของสารละลายที่ใช่จุ่มแช่เพิ่มขึ้น และเกิดการปิดกั้นรูพรุนขนาเล็กทำให้ปริมาณรูพรุนทั้งหมดและปริมาณการดูดซับคาร์บอนไดออกไซด์ลดลง ถ่านกัมมันต์ที่ผ่านการกระตุ้นเป็นเวลารวมทั้งสิ้น 180 นาที และออกซิไดซ์เป็นเวลา 720 นาที และจุ่มแช่ในสารละลายโซเดียมไฮดรอกไซด์ความเข้นข้นร้อยละ 1 โดยมวล มีปริมาณการดูดซับคาร์บอนไดออกไซด์สูงที่สุด แบบจำลองแกรนคาร์โนนิคัลมอนติคาร์โลถูกนำมาใช้ในการหาการกระจายขนาดของรูพรุนของถ่านกัมมันต์ ผลการศึกษาแสดงให้เห็นว่าการจุ่มแช่ถ่านกัมมันต์ในสารละลายโซเดียมไฮดรอกไซด์ส่งผลให้ปริมาตรของรูพรุนขนาดเล็กลดลงอย่างรวดเร็วและมีนัยสำคัญ

สำหรับงานในส่วนที่สาม เป็นการศึกษาการผลิตเมทานอลผ่านกระบวนการไฮโดรจีเนชั่นของคาร์บอนไดออกไซด์ งานในส่วนนี้มีวัตถุประสงค์ที่จะนำคาร์บอนไดออกไซด์มาผลิตเป็นสารละลายเมทานอล การศึกษาในส่วนนี้เป็นการสร้างแบบจำลองในโปรแกรมคอมพิวเตอร์ กระบวนการผลิตเมทานอลสามกระบวนถูกศึกษาและเปรียบเทียบราคาการผลิตเมทานอล โดยทำการวิเคราะห์ต้นทุนการผลิตและหาค่าที่เหมาะสมที่สุดโดยใช้โมเดลโครงข่ายประสาทเทียม โดยพบว่าโครงข่ายที่มีจำนวนโหนดแปดโหนดนั้นมีความคาดเคลื่อนของการประมาณค่าน้อยที่สุด ผลจากการศึกษาพบว่าการผลิตเมทานอลโดยใช้รีแอคเตอร์สองหน่วยต่อกันแบบอนุกรมมีต้นทุนการผลิตต่ำที่สุดเป็น 885.85 ดอลล่าร์ต่อตันเมทานอล ทั้งนี้พบว่าราคาของวัตถุดิบโดยเฉพาะอย่างยิ่งราคาของไฮโดรเจนส่งผลอย่างมากต่อต้นทุนการผลิตเมทานอล

และงานส่วนสุดท้ายนั้นเป็นการพัฒนาเทคนิคการเลือกกลุ่มตัวอย่างเพื่อใช้ในการออกแบบการทดลอง โดยเทคนิคการเลือกกลุ่มตัวอย่างนี้พัฒนามาจากเทคนิคการเลือกกลุ่มตัวอย่างแบบละตินไฮเปอร์คิวบ์ เทคนิคนี้สามารถเพิ่มสภาวะการทดลองเข้ามายังชุดข้อมูลที่มีอยู่โดยใช้ค่าสูงสุดของความแตกต่างระหว่างค่าที่ทำนายและค่าจริงของสภาวะนั้นเป็นเกณฑ์ การศึกษาได้ทำการประยุกต์ใช้เทคนิคการเลือกกลุ่มตัวอย่างนี้ในการหาค่าที่เหมาะสมที่สุดของกระบวนการทางเคมีสามกระบวนการประกอบไปด้วยกระบวนการผลิตเมทานอลผ่านกระบวนการไฮโดรเจเนชั่นของคาร์บอนไดออกไซด์ กระบวนการผลิตแอมโมเนีย และกระบวนการดูดซึมคาร์บอนไดออกไซด์โดยใช้สารละลายเมทานอลและใช้โมเดลโครงข่ายปราสาทเทียม ทั้งนี้ผลของการศึกษายังถูกนำไปเปรียบเทียบกับเทคนิคการเลือกกลุ่มตัวอย่างแบบสุ่ม ผลการศึกษาแสดงให้เห็นว่าเทคนิคการเลือกกลุ่มตัวอย่างที่ถูกพัฒนาขึ้นนั้นสามารถใช้ในกระบวนการการหาค่าที่เหมาะสมที่สุดได้และใช้จำนวนสภาวะการทดลองน้อยกว่าการออกแบบการทดลองแบบสุ่มเมื่อเปรียบเทียบการให้ค่าที่เหมาะสมที่สุด เมื่อนำเทคนิคการเลือกกลุ่มตัวอย่างที่ถูกพัฒนาไปประยุกต์ใช้กับกระบวนการทั้งสามกระบวนการที่กล่าวมาข้างต้น พบว่าสามารถประยุกต์ใช้ได้กับทั้งสามกระบวนการและได้ค่าที่เหมาะสมที่สุดของแต่กระบวนการ

สาขาวิชา <u>วิศวกรรมเคมี</u> ลายมือชื่อนักศึกษา.....

ปีการศึกษา <u>2566</u> ลายมือชื่ออาจารย์ที่ปรึกษา.....

PRAPATSORN BORISUT : CARBON DIOXIDE ADSORPTION BY NaOH IMPREGNATED ACTIVATED CARBON FROM LONGAN FRUIT SEED AND THE ADAPTIVE SAMPLING APPROACH FOR PROCESS SIMULATION-BASED OPTIMIZATION.
THESIS ADVISOR : AROONSRI NUCHITPRASITTICHAI, Ph.D., 206 PP.

Keywords: Adsorption/Carbon dioxide/Activatedcarbon/Sampling technique/ Optimization/Experimental design

This dissertation aims to study the enhancement of CO_2 adsorption by employing NaOH impregnated activated carbon prepared from longan fruit seed and to develop the sampling technique for use in simulation-based optimization. This dissertation was divided into four parts. In the first part, the prepared microporous and mesoporous activated carbon were used to adsorb CO_2 in a fixed bed column. Five parameters were studied for their effects on the adsorption amount including the volume ratio of microporous and mesoporous, adsorption temperature, sodium hydroxide loading, gas feed rate, and the adsorbent amount. The CO_2 adsorption amount increased by 45% when the activated carbon was impregnated with 1% of NaOH solution.The optimal conditions that provided the maximum adsorbed amount of CO_2 in a fixed bed (33.58 mg/g) were volume ratio of microporous and mesoporous of 2.83, NaOH loading of 76.5 mg/g, 51 kg/m^2 of amount of activated carbon, adsorption temperature of 20°C, and the gas feed rate of 156 kg/h-m^2.

For the second part, four types of activated carbons consisting of two types of microporous activated carbon and two types of mesoporous activated carbon were employed to study the adsorption of CO_2 at high pressure. The activated carbon samples were impregnated with NaOH solutions of 1, 4, 7, 10, and 13% by weight. Activated carbon which was activated with a total time of 180 min, oxidized with 720 min, and impregnated by 1% NaOH solution provided the highest CO_2 adsorption amount. The Grand Canonical Monte Carlo simulation was used to determining pore size distribution of each activated carbon. The result indicate that after impregnated with 1% by weight of NaOH, the microporous of activated carbon dramatically decreased. The highest amount of CO_2 adsorption of microporous activated carbon takes place in 1.4 nm pores after impregnated, followed by mesopores. Mesoporous

activated carbon can adsorbed at pore diameter less than 2 nm. However, most adsorption takes place in pores smaller than 1 nm due to the strong interaction in the small pores.

The third part of this dissertation involved the simulation-based optimization of methanol production via CO_2 hydrogenation process. Three configurations of methanol production were studied to obtain the minimum methanol production cost using cost analysis. The artificial neural network with eight nodes was used as a surrogate model for process optimization. The cost of methanol production was shown to be significantly impacted by the price of raw materials, particularly the price of hydrogen. It was found that the minimum methanol production cost was $885.85 per tonne which was obtained from the optimization of methanol production with two reactors in series design.

The final part of the dissertation focused on developing a sampling technique for sample selection to be used in experimental design. This sampling technique is derived from the Latin hypercube sampling method. It allows for the incorporation of additional points into existing data sets by using the maximum deviation between predicted and actual values of a given point as a criterion. This sampling technique was applied to find the optimal conditions for three chemical processes which are methanol production via carbon dioxide hydrogenation, ammonia production, and carbon dioxide absorption via the Rectisol process. An artificial neural network was utilized for this purpose. Additionally, the results of the study were compared with those obtained using a random sampling method. The findings demonstrate that the developed Latin hypercube sampling can efficiently determine optimal values and requires fewer experimental conditions compared to the random sampling design. When applied to all three processes, the developed technique proved to be applicable and yielded optimal values for each process.

School of Chemical Engineering Student's Signature.....

Academic Year 2023 Advisor's Signature.....

ACKNOWLEDGEMENTS

This dissertation and my Ph.D. career would not have been achieved without many people, who always support and encourage me. I appreciate and am thankful for all of them.

First, I sincerely thank my advisors, Dr. Chaiyot Tangsathitkulchi and Dr. Aroonsri Nuchitprasittichi for their belief and unending support, encouragement, and patience over the six years of my Ph.D. career. Dr. Tangsathitkulchai gave me a great opportunity that I had not expected, and that opportunity shaped me into a new one. Dr. Nuchitprasittichai, I would like to express the deepest appreciation. I deeply passionate about her research area that was the reason of my decision to start my Ph.D. career. In the many years since undergrad school, she always motivated me and advised me to step past the problem I faced. I never feel alone when I faced the research problems. My special thanks go to Dr. Selen Cremaschi, a supervisor during my research time at Auburn University, AL, United States. She is an excellent professor, I never found. I learned both how to conduct good research and how to be a good researcher from her. The time I spent during this period of the visiting scholar program was the greatest time of my life. This time, this work, and people changed my perspective on the Ph.D. career forever. In addition, I would like to thank Dr. Atichat Wongkoblap, my co-advisor. He gave me a great advice since undergrad school. My work cannot be finished if I have not receive his suggestion and advice.

I would like to thank my committee members, Dr. Ratanawan Kiattikomol and Dr. Lek Wantha for agreement to the part of my committee for my thesis defense. Thank you for a valuable comments and recommendations. I would like to thank Dr. Panarat Rattanaphanee. She is my role model who inspired me to think about becoming a good professor one day. From the first class I studied with her, I started thinking about my Ph.D. career since that time. I also appreciate Dr. Supunnee Junpirom, who encouraged and advised me when I was stuck in a difficult time.

I also appreciate the assistance from the technical and secretary staff at the School of Chemical Engineering, SUT, especially, Mr. Saran Dokmaikun for his help in

มหาวิทยาลัยเทคโนโลยีสุรนารี

my research works. Mrs. Amporn Ladnongkhun for her skill in the secretarial work of our school.

I sincerely give thanks to my seniors in the Carbon and Adsorption Research (CAR) group, Dr. Krittamet Photong, Dr. Panuwat Lawtae, and Mr. Tarathorn Limsiri for their helpful to my research work. My colleagues in the Cremaschi group at Auburn University, Dr. Shuang Xu, Dr. Yuchi Deng, Mr. Shinmoy Basak, Mr. Shenbageshwaran Rajendiran, Miss Poojazen Santhamoorthy, Mr. Yasuhiro Shoji, Miss Su Meyra Tatar, Mr Erfan Hosseini, Mr Micheal Fokuo, Mr Chukuma Nwanazoba, Miss Parvane Saeid also deserve my thanks for their extremely helpful, endless teaching me in the machine learning field. I also thanks all of my friends. I cannot tell how good they are but they also encourage and give me advice and their hand when I felt lost.

I gratefully acknowledge the financial support from the National Research Council Thailand (NRCT) via the Royal Golden Jubilee Ph.D. (RJG) program, grant number PHD/0214/2561 for sponsoring and supporting research through my Ph.D. career.

Finally, I am deeply grateful to my parents and my beloved sister for their unwavering love, support, and encouragement. They have never given up on me, steadfastly standing by my side during life's toughest challenges.

Prapatsorn Borisut

มหาวิทยาลัยเทคโนโลยีสุรนารี

TABLE OF CONTENTS

Page

ABSTRACT (THAI) I
ABSTRACT (ENGLISH) III
ACKNOWLEDGEMENTS V
TABLE OF CONTENTS VII
LIST OF TABLES XII
LIST OF FIGURES XIV
SYMBOLS AND ABBREVIATIONS XX
CHAPTER
I INTRODUCTION 1
1.1 Background 1
1.2 Research objectives 4
1.3 Scope and Limitation of Research Work 5
1.3.1 Preparation and adsorption of activated carbon impregnated with sodium hydroxide solution 5
1.3.2 Investigation of the behavior of carbon dioxide adsorption in slit pore model using GCMC simulation 5
1.3.3 Development of experimental design and simulation based optimization approach 6
1.4 Output of Research 6
1.5 Organization 6
1.6 References 8
II THE DYNAMIC ADSORPTION OF CO_2 IN A FIXED BED COLUMN OF LONGAN-BASED ACTIVATED CARBON WITH NaOH LOADING 10
2.1 Abstract 10
2.2 Introduction 11
2.3 Fixed-Bed Adsorption Theory 13

TABLE OF CONTENTS (Continued)

Page

2.4 Materials and Methods 15
2.4.1 Raw Material Preparation 15
2.4.2 Raw Material Characterization 16
2.4.3 Activated Carbon Preparation 16
2.4.4 NaOH Impregnated Activated Carbon Preparation 17
2.4.5 Porous Properties of Activated Carbon 18
2.4.6 CO_2 Adsorption Isotherms 18
2.4.7 Dynamic of CO_2 Adsorption in a Fixed-Bed Column 19
2.5 Results and Discussion 21
2.5.1 Precursor Characterization 21
2.5.2 Surface Morphology of Prepared Activated Carbon 23
2.5.3 N_2 Adsorption/Desorption Isotherms of Prepared Activated Carbon 25
2.5.4 Porous Properties of Prepared Activated Carbon 27
2.5.5 Experimental CO_2 Breakthrough Curves 31
2.5.6 Development of Correlations for q_B and t_B By the RSM 40
2.5.7 The Breakthrough Model 45
2.6 Conclusions 50
2.7 References 51
III INVESTIGATION THE BEHAVIOR OF CARBON DIOXIDE ADSORPTION BY NaOH IMPREGNATED LONGAN SEED ACTIVATED CARBON USING GCMC 56
3.1 Abstract 56
3.2 Introduction 57
3.3 Methods 58
3.3.1 Experimental Isotherms 58
3.3.2 The Kernel of Equilibrium Adsorption Isotherms 60

TABLE OF CONTENTS (Continued)

Page

3.3.3 Determining Pore Size Distribution 61
3.3.4 Calculation of CO_2 Absolute Isotherms 62
3.4 Results and Discussion 63
3.4.1 Experimental Adsorption Results 63
3.4.2 Simulation Results 72
3.4.3 Effects of Pore Width on CO_2 Adsorption 76
3.4.4 Effects of %NaOH on CO_2 Adsorption 77
3.4.5 Effects of Functional Group Allocation on CO_2 Adsorption 78
3.4.6 Pore Size Distributions 81
3.5 Conclusions 86
3.6 References 86
IV PROCESS CONFIGURATION STUDIES OF METHANOL PRODUCTION VIA CARBON DIOXIDE HYDROGENATION: PROCESS SIMULATION -BASED OPTIMIZATION USING ARTIFICIAL NEURAL NETWORKS 89
4.1 Abstract 89
4.2 Introduction 90
4.3 Process Simulation and Economic Evaluation 93
4.3.1 Process Simulation 94
4.3.2 Economic Evaluation 97
4.4 Simulation-Optimization Methodology 97
4.4.1 Latin Hypercube Sampling 100
4.4.2 Artificial Neural networks 101
4.4.3 Optimization Formulation 101
4.5 Results and Discussion 102
4.5.1 Price Sensitivity 102
4.5.2 Comparison of Different Process Configurations 103
4.5.3 The Optimal Solutions 105

TABLE OF CONTENTS (Continued)

Page

4.6 Conclusion 108
4.7 References 108
V ADAPTIVE LATIN HYPERCUBE SAMPLING FOR SURROGATE-BASED OPTIMIZATION WITH ARTIFICIAL NEURAL NETWORK 112
5.1 Abstract 112
5.2 Introduction 112
5.3 Sampling Technique and Surrogate Modeling 115
5.3.1 Latin Hypercube Sampling 116
5.3.2 Random Sampling 120
5.4 Methodology 121
5.4.1 Proposed Adaptive Latin Hypercube Sampling for Surrogated-based Optimization 121
5.4.2 Adaptive Latin Hypercube for Optimization 123
5.4.3 Verification of the Optimal Solution Using Random Sampling technique 124
5.4.4 Case Studies 125
5.5 Results and Discussion 129
5.5.1 The Results of Random Sampling 130
5.5.2 The Convergence of the Proposed Adaptive LHS Optimization 130
5.5.3 Comparison of Optimal Solutions Between Proposed Sampling and Random Sampling 133
5.6 Conclusion 136
5.7 References 137
VI CONCLUSIONS AND RECOMMENDATIONS 143
6.1 Conclusions 143
6.2 Recommendations 144

TABLE OF CONTENTS (Continued)

Page

6.2.1 The Proper Amount of Micropores and Mesopores 144
6.2.2 Applying Adaptive LHS Approach to Advanced Surrogate Model Techniques 144
6.2.3 Comparison of the Adaptive LHS Approach with Other Sequential Sampling and Application to More Complex Problems 145
6.2.4 Application of Adaptive LHS to Various Fields of Study 145
APPENDIX
APPENDIX A SUPPLEMENTARY INFORMATION 146
APPENDIX B ESTIMATION OF EQUIPMENT COSTS 201
APPENDIX C LIST OF PUBLICATIONS 204
BIOGRAPHY 206

มหาวิทยาลัยเทคโนโลยีสุรนารี

LIST OF TABLES

Table **Page**

2.1 Values of decision variables used for studying CO_2 adsorption in a fixed bed of activated carbon (using 3 g activated carbon in 25 cm^3 NaOH solution, and adsorption column ID of 1 cm) 21

2.2 Proximate and ultimate analyses of longan seed precursor used in this work 23

2.3 Porous properties of prepared activated carbons calculated from N2 adsorption/desorption isotherms at -196°C 29

2.4 Effect of concentration of impregnant solution on porous properties of various porous adsorbents 30

2.5 Effects of process variables on the breakthrough parameters of CO_2 adsorption in a fixed bed of longan-seed activated carbon (diameter of adsorption column = 1 cm) 37

2.6 CO_2 adsorption capacity in a fixed bed of alkali-impregnated porous adsorbents 40

2.7 The optimal adsorption conditions that provide the maximum adsorption capacity of CO_2 at breakthrough time 43

3.1 Porous properties of prepared activated carbons using nitrogen adsorption/desorption at -196.15°C 70

4.1(a) Range of the decision variables of configuration I 99

4.1(b) Range of the decision variables of configuration II 99

4.1(c) Range of the decision variables of configuration III 100

4.2(a) Results of fitting data with artificial neural networks for configuration I: once-through reactor methanol production 104

4.2(b) Results of fitting data with artificial neural networks for configuration II: methanol production with a recycle 104

LIST OF TABLES (Continued)

Table **Page**

4.2(c) Results of fitting data with artificial neural networks for configuration III: methanol production with two reactors in series 105
4.3 Optimal operating conditions and minimum methanol production cost of three configurations 106
4.4 Energy consumption and energy cost for equipment for three configurations 107
5.1 The approach for constructing optimal Latin hypercube sampling 118
5.2 Range of decision variables of case study 1 127
5.3 Range of decision variables of case study 2 128
5.4 Range of decision variables of case study 3 129
5.5 Result of random sampling of three case studies 130
5.6 Comparison the results of proposed adaptive Latin hypercube sampling and random sampling 134

มหาวิทยาลัยเทคโนโลยีสุรนารี

LIST OF FIGURES

Figure **Page**

2.1 Experimental set up for the study of CO_2 adsorption in a fixed bed of activated carbon prepared from longan seed 20

2.2 TG and DTG curves of longan seed used as the raw material in this work 22

2.3 SEM micrographs of prepared activated carbons; series (a), (b), (c), and (d) stands for AC850-2, AC900-3, AC-OTA1, and AC-OTA2, respectively, with magnification of 1K. The columns a1-a3, b1-b3, c1-c3 and d1-d3 indicate the different concentrations of NaOH solution of 0, 1, and 2 weight%, respectively 24

2.4 Results of SEM-EDX analysis of sample AC-OTA2-1 25

2.5 N_2 adsorption/desorption isotherms of microporous activated carbons prepared by the conventional activation method, (a) and (c), and mesoporous activated carbons prepared by the OTA method, (b) and (d) 26

2.6 Pore size distributions of various activated carbon samples (a) – (c), the microporous carbon series and (d) – (f), the mesoporous carbon series, with varying NaOH loadings 31

2.7 Effect of NaOH impregnation loading on CO_2 adsorption isotherms at 273 K (0°C) of longan-seed activated carbon, where Po is the saturation vapor pressure of CO_2 at 273 K (3.5 MPa), for (a) microporous carbon series and (b) mesoporous carbon series 35

2.8 Effects of process variables on CO_2 breakthrough curves; (a) carbon type (X_1), (b) temperature (X_2), (c) NaOH loading (X_3), (d) gas feed rate (X_4), and (e) adsorbent amount (X_5) 36

LIST OF FIGURES (Continued)

Figure **Page**

2.9 Effects of process variables on t_B and q_B for the adsorption of CO_2 in a fixed-bed of activated carbon; (a) X_2 = 30°C, X_3 = 67 mg/g, X_4 = 135 kg/m^2-h, X_5 = 76 kg/m^2 (6g), (b) X_1 = 3.15 kg/m^2-h, X_3 = 67 mg/g, X_4 = 135 kg/m^2-h, X_5 = 76 kg/m^2 (6g), (c) X_1 = 3.15, X_2 = 30°C, X_4 = 135 kg/m^2-h, X_5 = 76 kg/m^2-h (6g), (d) X_1 = 3.15, X_2 = 30°C, X_3 = 67 mg/g, X_5 = 76 kg/m^2 (6g), (e) X_1 = 3.15, X_2 = 30°C, X_3 = 67 mg/g, X_4 = 135 kg/m^2-h 39

2.10 Typical response surface plots showing (a) the effect of NaOH loading and V_{mic}/V_{mes} on q_B for adsorption temperature of 20°C, total gas flow rate of 156 kg/m^2-h, and adsorbent amount of 51 kg/m^2, and (b) the effect of total gas flow rate and adsorption temperature on q_B for V_{mic}/V_{mes} of 2.83, NaOH loading of 76.5 mg/g, and adsorbent amount of 51 kg/m^2 44

2.11 Typical response surface plots showing (a) the effect of NaOH loading and V_{mic}/V_{mes} on t_B for adsorption temperature of 30°C, total gas flow rate of 135 kg/m^2-h, and adsorbent amount of 76 kg/m^2, and (b) the effect of adsorbent amount and adsorption temperature on t_B for V_{mic}/V_{mes} of 2.83, NaOH loading of 76.5 mg/g, and total gas flow rate of 135 kg/m^2 44

2.12 The fitting of the Klinkenberg's breakthrough equation to the experimental breakthrough data for, (a) Effect of NaOH loading (X_3) for X_1 = 3.15, X_2 = 30°C, X_4 = 135 kg/m^2-h, X_5 = 76(6) kg/m^2(g), and (b) Effect of adsorbent amount (X_5) for X_1 = 4.39, X_2 = 30°C, X_3 = 67 mg/g, X_4 = 135 kg/m^2-h 48

LIST OF FIGURES (Continued)

Figure **Page**

2.13 Effect of process variables on the breakthrough model parameters;
(a) X_2 = 30°C, X_3 = 67 mg/g, X_4 = 135 kg/m^2-h, X_5 = 76 kg/m^2 (6g),
(b) X_1 = 3.15, X_3 = 67 mg/g, X_4 = 135 kg/m^2-h, X_5 = 76 kg/m^2 (6g),
(c) X_1 = 3.15, X_2 30°C, X_4 =135 kg/m^2-h, X5 = 76 kg/m^2 (6g),
(d) X_1 = 3.15, X_2 = 30°C, X_3 = 67 mg/g, X_5 = 76 kg/m^2 (6g),
(e) X_1 = 3.15, X_2 = 30°C, X_3 = 67 mg/g, X_4 = 135 kg/m^2-h 49
2.14 Relationship between Henry's constant of the linear isotherm (K) and pore diffusivity (D_e) 50
2.15 Effect of V_{mic}/V_{mes} on the effective pore diffusivity (D_e) 50
3.1 Steps of activated carbon preparation 59
3.2 The slit pore model: (a) absence of NaOH molecules and (b) presence of NaOH molecules 61
3.3 Nitrogen adsorption/desorption isotherms of original activated carbon 64
3.4 N_2 adsorption/desorption isotherms at -196.15°C of original and impregnated activated carbon prepared by total impregnation method of four different types of activated carbon consisting of (a) A850-120, (b) A850-180, (c) O230-120 and (d) O200-180 66
3.5 CO_2 adsorption isotherms at 0°C of original and impregnated activated carbon prepared by total impregnation method of four different types of activated carbon, including (a) A850-120, (b) A850-180, (c) O230-120 and (d) O200-180 68
3.6 SEM images of original activated carbon and impregnated activated carbon with NaOH solutions 72
3.7 The kernels of GCMC simulated equilibrium adsorption isotherms of N_2 at -196.15°C in the model of carbon slit pores of 54 pore sizes; (a) original carbon slit pores and (b) carbon slit pores with 1% NaOH, (c) carbon slit pores with 4 weight% NaOH solution and (d) carbon slit pores with 7 weight% NaOH solution 74

LIST OF FIGURES (Continued)

Figure **Page**

3.8 The kernels of GCMC simulated equilibrium adsorption isotherms of CO_2 at 0°C in model carbon slit pores of 53 pore sizes; (a) original carbon slit pores, (b) carbon slit pores with 1% NaOH, (c) carbon slit pores with 4% NaOH and (d) carbon slit pores with 7% NaOH 76

3.9 Effect of pore width on CO_2 adsorption amount with various %NaOH at pressure (a) 0.1 kPa, (b) 10 kPa, (c) 100 kPa and (d) 3500 kPa 77

3.10 Effect of %NaOH on CO_2 adsorption amount with various pore width at pressure (a) 0.1 kPa, (b) 10 kPa, (c) 100 kPa and (d) 3500 kPa 78

3.11 Effects of functional group allocation on CO_2 adsorption isotherms at 0°C for the carbon slit pore model of 0.65 nm width at (a) plotted in semi-log scale and (b) plotted in linear scale 79

3.12 Effects of functional group allocation on CO_2 adsorption isotherms at 0°C for the carbon slit pore model of 1.5 nm width at (a) plotted in semi-log scale and (b) plotted in linear scale 80

3.13 Snapshots of CO_2 molecules in carbon slit pore model of 0.65 nm. CO_2 adsorption at 0°C and 1% of NaOH functional groups with random topology. In these figures, the large brown spheres represent the solid model of carbon, yellow and blue spheres represent the functional group, and black and red spheres represent atoms of C and O of CO_2 molecule, respectively 80

3.14 Snapshots of CO_2 molecules in carbon slit pore model of 0.65 nm CO_2 adsorption at 0°C and 1% of NaOH functional groups with Fixed topology. In these figures, the large brown spheres represent The solid model of carbon, yellow and blue spheres represent The functional group, and black and red spheres represent atoms of C and O of CO_2 molecule, respectively. 80

LIST OF FIGURES (Continued)

Figure **Page**

3.15 Snapshots of CO_2 molecules in carbon slit pore model of 1.5 nm CO_2 adsorption at 0°C and 1% of NaOH functional groups with random topology. In these figures, the large brown spheres represent the solid model of carbon, yellow and blue spheres represent the functional group, and black and red spheres represent atoms of C and O of CO_2 molecule, respectively 81

3.16 Snapshots of CO_2 molecules in carbon slit pore model of 1.5 nm CO_2 adsorption at 0°C and 1% of NaOH functional groups with fixed topology. In these figures, the large brown spheres represent the solid model of carbon, yellow and blue spheres represent the functional group, and black and red spheres represent atoms of C and O of CO_2 molecule, respectively 81

3.17 Effect of NaOH loading on pore size distribution computed by DFT using adsorption of N_2 at -196.15°C of four type activated carbons: (a) A850-120, (b) A850-180, (c) O230-120 and (d) O200-180 83

3.18 Effect of NaOH loading on pore size distribution computed by GCMC simulation using adsorption isotherms of CO_2 at 0°C for four type activated carbons: (a) A850-120, (b) A850-180, (c) O230-120 and (d) O200-180 85

4.1 Process simulation of the methanol production via carbon dioxide hydrogenation: (a) configuration I; (b) configuration II; and (c) configuration III 96

4.2 Algorithm for Latin hypercube design for Artificial neural network training 98

4.3 Experimental design: Latin hypercube sampling 100

4.4 The schematic of the feed-forward neural network with a single hidden layer 101

LIST OF FIGURES (Continued)

Figure **Page**

4.5 The impact of carbon dioxide and hydrogen price on methanol production cost 103
5.1 Illustration of Latin hypercube sampling for N = 10 of (a) good filling design (b) poor filling design 117
5.2 Illustration of random sampling for (a) N = 10, (b) N = 100 120
5.3 Proposed adaptive Latin hypercube sampling for surrogate-based optimization 122
5.4 Additional sample points using maximum deviation 123
5.5 Random sampling for optimization 124
5.6 Process simulation of ammonia production from syngas 126
5.7 Process simulation of methanol production via carbon dioxide hydrogenation 128
5.8 Process simulation of CO_2 captured via Rectisol process 129
5.9 The convergence of the proposed algorithm for all three case studies: (a) ammonia production from syngas, (b) the production of methanol from carbon dioxide hydrogenation, (c) carbon dioxide absorption by methanol via Rectisol process 132

มหาวิทยาลัยเทคโนโลยีสุรนารี

SYMBOLS AND ABBREVIATIONS

A	Specific area (m^2/g)
AC	Activated Carbon
A_c	Column cross-section area (m^2)
ANN	Artificial neural network
A_v	Avogadro number (6.02214076×10^{23} molecule/mol)
BET	Brunauer-Emmett-Teller theory
B1	Biases of input layer
B2	Biases of output layer
C	Concentration of adsorbate at the column exit (Volume of CO_2 per Volume of N_2)
CCD	Central composite design
C_0	Inlet concentration of adsorbate (Volume of CO_2 per Volume of N_2)
D_c	Column diameter (m)
D_e	Effect pore diffusivity (m^2/s)
D_m	Molecular diffusivity of the diffusing species (m^2/s)
DoE	Design of experiment
d_p	Particle diameter (nm)
DTG	Derivative Thermogravimetric
f	Fugacity (Pa)
FF	Fluid-Fluid (a.k.a. Adsorbate-Adsorbate)
G	Mass velocity of gas (kg/m^2s)
GCMC	Grand Canonical Monte Carlo
HPVA	High-pressure volumetric analyzer
IUPAC	International Union of Pure and Applied Chemistry
K	Affinity constant
K	Henry's constant of linear isotherm
k_B	Boltzmann constant (1.380649×10^{-23} J/K)
k_C	Film mass transfer coefficient (m/s)

มหาวิทยาลัยเทคโนโลยีสุรนารี

SYMBOLS AND ABBREVIATIONS (Continued)

k_P	Particle-mass transfer coefficient (s^{-1})
LB	Lorentz-Berthelot mixing rule
LJ	Lennard-Jones
L_B	Bed height (m)
LDF	Linear transfer driving force
LHS	Latin hypercube sampling
L_{MTZ}	Length of mass transfer zone (m)
MSE	Mean square error
N	Number of sample points
k	number of decision variables
OTA	Oxidation Thermal destruction and Activation
P	Pressure (Pa)
P°	Bulk coexistence pressure (Pa) (a.k.a. Saturation vapour pressure)
P/P°	Relative pressure
PSD	Pore Size Distribution
Q	Volumetric flow rate of the feed stream (cm^3/s)
q	Excess adsorption amount (mol/g)
q’	Absolute adsorption amount (mol/g)
q_B	CO_2 adsorption capacity at breakthrough time (mg/g)
q_E	CO_2 adsorption capacity at equilibrium time (mg/g)
q^{exp}	Experimental adsorbed amount (mol/g)
q'_m	Parameter of solid coverage surface
q^{sim}	Simulation adsorbed amount (mol/g)
r	Number of neurons in hidden layer
R_P	Particle radius (m)
RSM	Response surface methodology
S_{BET}	BET specific area (m^2/g)
SF	Solid-Fluid (a.k.a. Adsorbent-Adsorbate)
t	Time (s)

SYMBOLS AND ABBREVIATIONS (Continued)

t_B	Breakthrough time (s)
t_E	Equilibrium time (s)
TGA	Thermogravimetric Analysis
u	gas interstitial velocity (m/s)
v	Volume fraction of each pore width
v_a	Volume of adsorbate in adsorbed phase (m^3/g)
V_{mes}	Mesopore volume (cm^3/g)
V_{mic}	Micropore volume (cm^3/g)
V_{tot}	Total pore volume (cm^3/g)
w	Pore width (nm)
W1	Input weight of hidden layer
W2	Input weight of output layer
α	Level of significant
β_0	2nd order model constant
β_i	Coefficient of linear term in 2nd order model
β_{ii}	Coefficient of quadratic term in 2nd order model
β_{ij}	Coefficient of interaction term in 2nd order model
ε_b	Bed porosity
$\varepsilon_{f\text{-}f}$	Well depth of fluid (K)
$\varepsilon_{s\text{-}s}$	Well depth of solid (K)
$\varepsilon_{s\text{-}f}$	Cross-well depth of solid and fluid (K)
μ	Fluid viscosity
μ	Bulk chemical potential of the adsorbate of bulk fluid
ξ	Dimensionless length in the Klinkenberg's equation
ρ	Fluid density
ρ_g	Bulk gas density
ρ_s	Density of adsorbent particles (38.2 nm^{-2})
σ_{ff}	Collision diameter of fluid (nm)

มหาวิทยาลัยเทคโนโลยีสุรนารี

SYMBOLS AND ABBREVIATIONS (Continued)

σ_m	Projection area of the adsorbate molecule (nm^2/molecule)
$\sigma_{s\text{-}s}$	Collision diameter of solid (nm)
$\sigma_{s\text{-}f}$	Cross-collision diameter between solid and fluid (nm)
τ	Dimensionless time in the Klinkenberg's equatio

มหาวิทยาลัยเทคโนโลยีสุรนารี

CHAPTER I
INTRODUCTION

1.1 Background

Carbon dioxide (CO_2) is one of the most anthropogenic greenhouse gases, which causes global warming. A large quantity of carbon dioxide is released from power plants burning fossil fuels (Russell 2014; Nanda et al. 2016). An increase in the quantity of carbon dioxide in the atmosphere leads to a challenge for its capture and utilization. Typically, carbon dioxide capture involves three different processes: pre-combustion, post-combustion, and oxy-combustion (Metz, et al. 2005; Mukherjee et al. 2019). For the more practical post-combustion method, four technologies including absorption, adsorption, cryogenic, and membrane, are currently employed for efficient carbon dioxide capture (Li et al. 2013).

Carbon dioxide absorption by liquid amine has been widely used due to its high removal efficiency (Aghel et al. 2022). However, this process has many shortcomings such as high corrosion, high power consumption for amine recovery, and high cost. Consequently, carbon dioxide capture by adsorption with solid adsorbent has emerged to be more attractive alternative. The adsorption process is one of the interesting technologies for several reasons, i.e., the low cost of materials used as adsorbents, low energy for adsorbent regeneration, and extremely high efficiency (Mohd et al. 2022). Activated carbon is a porous carbon material that is widely used as an adsorbent due to its high internal surface area and large amounts of micropores, leading to high adsorption capacity. Generally, activated carbon can be prepared by two-step physical activation method and chemical activation method. Many researchers have reported the preparation of activated carbon from a variety of agricultural products such as coconut shells, walnut shells, eucalyptus, argan fruit shells, longan seeds, corn stalks, etc. (Chen et al. 2012; Chen et al. 2016; Naksusuk and Tangsathitkulchai 2019; Phothong et al. 2021). Activated carbon, which consists mostly of micropores, is typically used for gas adsorption, including carbon dioxide. To increase carbon dioxide capture efficiency,

attempts have been made by a number of researchers to synthesize activated carbons with superior adsorption capacity (Aghel et al. 2022; Chen et al. 2016).

Since carbon dioxide is an acid gas, using an adsorbent with more active basic sites will help improve the capacity and selectivity of carbon dioxide adsorption. The simplest technique used for introducing basic sites on the surface of an adsorbent is by impregnating the adsorbent with basic alkali solutions. Many researchers have investigated the role and efficiency of various impregnation solutions, for example, sodium hydroxide, potassium hydroxide, metal oxide, and amine solutions, on carbon dioxide adsorption capacity (Tan et al. 2014; Mohammad et al. 2019).

Therefore, this research aims to study the improvement of activated carbon from longan seed for carbon dioxide adsorption by applying an impregnation technique with sodium hydroxide solution. However, the proportion of various pore sizes in activated carbon is also a determining factor that can influence the transport of the impregnant molecules inside the pores, and hence the uptake amounts in various pore sizes that, in turn, can affect the performance of carbon dioxide capture. Interesting according to the porous properties, which are more appropriate with the impregnation method and can prevent the phenomena of pore blockage. As a result of this consideration, two types of activated carbon, that is, one containing mostly micropores and the other containing mostly mesopores are also tested for carbon dioxide adsorption in a fixed bed mode. Moreover, gas adsorption is also studied using computer simulation to verify and identify the effect of impregnate molecules on the adsorption behavior.

Besides the attempt to improve the capture efficiency for carbon dioxide by the alkali-impregnated activated carbon, the utilization of captured carbon dioxide as a value-added product is also of considerable interest. This is explored in this work by studying a methanol production via carbon dioxide because it is an environmentally friendly fuel and has a high demand for use as a solvent (Zander et al. 2013; Bowker 2019). However, the cost of direct conversion via carbon dioxide hydrogenation is relatively high due to the large amount of hydrogen consumption (Tidona et al. 2013). As a result, the design and optimization of methanol production via carbon dioxide hydrogenation are necessary to determine the suitable configuration and operating conditions. Therefore, this research performed three different configurations of

methanol production for a simulation-based optimization process aimed at finding the optimal conditions that can reduce methanol production costs. The simulation-based optimization algorithm has four basic steps including process variable selection, sample generation, mathematical model construction, and optimization. For many engineering problems, a mathematical model is an important way to interpret the output of a system as a function of their output, e.g. operating conditions of the process or/and chemical properties (Avula, 2003). The mathematical model can be generated by using the set of input-output data obtained from simulation or experiment. The input-output data set is the most important for constructing a mathematical model. Therefore, the study of the design of the experiment (DoE) is necessary to select the numbers and locations of sample points (Montgomery, 2017). Factorial design, Box-Behnken design, central composite design, and Latin hypercube design are widely used as experimental designs. These sampling techniques can cover most of the considered regions of variables. However, in a more complex system, the response of the system cannot be represented by a low-order polynomial model. Hence, developing a complex model with proper experimental design is an attractive aspect of this study.

Therefore, the final part of this research also introduced an adaptive Latin hypercube sampling technique, which can generate the sample points for representing the design space of a simulation-based optimization problem to achieve the feasible optimal solution with the fewest sample points. This algorithm started with the small sample point generating using Latin hypercube sampling, and then additional sample points were generated and sequentially added to the data set. The artificial neural networks (ANNs) are employed as a surrogate model. Three chemical processes are used as case studies to represent problems with varying complexity and number of process variables.

1.2 Research Objectives

The overall objective of the reseach is to examine the effect of mesoporosity and alkali loading of activated carbon from longan seed on its carbon dioxide adsorption capacity and to develop an adaptive sampling technique for simulation-based optimization problems. The study is divided into three parts consisting of (1) the equilibrium and dynamic adsorption of carbon dioxide in a fixed bed column by alkali impregnated activated carbon derived from longan seed, (2) an investigation of the behavior of carbon dioxide adsorption at high pressure by alkali impregnated longan-seed activated carbon using the Grand Canonical Monte Carlo (GCMC) simulation, and (3) the development of an adaptive Latin hypercube sampling technique for an experimental design and application on different case studies. The specific objectives of the thesis work are as follows.

1.2.1 To prepare and characterize the char and activated carbon from longan seed by the two-step physical activation with carbon dioxide.

1.2.2 To prepare and characterize the mesoporous activated carbon from longan seed by the consecutive process of air oxidation, thermal destruction of surface functional groups, and carbon activation (OTA) method.

1.2.3 To study the CO_2 adsorption equilibrium and test the adsorption dynamic of carbon dioxide in a fixed bed column using the prepared microporous and mesoporous activated carbon.

1.2.4 To study the effect of alkali loading and mesoporosity on carbon dioxide adsorption capacity using experimental design.

1.2.5 To study the behavior of carbon dioxide adsorption in a slit pore with sodium hydroxide functional group using GCMC simulation.

1.2.6 To analyze process design and optimization of three different configurations of methanol production using simulation-based optimization.

1.2.7 To develop an adaptive sampling technique for simulation-based optimization problems and apply it to the simulation case studies.

1.2.8 To analyze process modeling and optimization of three different chemical process case studies.

1.3 Scope and Limitation of the Research Work

The scope of this research is separated into three parts: (1) preparation and adsorption of activated carbon impregnated with sodium hydroxide solution; (2) investigation of the behavior of carbon dioxide adsorption in slit pore model using GCMC simulation; and (3) development of experimental design and simulation-based optimization approach.

1.3.1 Preparation and adsorption of activated carbon impregnated with sodium hydroxide solution

Longan seed was used as a precursor to produce microporous and mesoporous activated carbon under various preparation conditions. Microporous activated carbon was prepared using the two-step activation method with carbon dioxide being used as the oxidizing agent. Mesoporous activated carbon was prepared by the OTA method using carbon dioxide and air. Both microporous and mesoporous activated carbon were impregnated with various concentrations of sodium hydroxide solutions. The prepared activated carbons were characterized by nitrogen adsorption/desorption at −195.8°C, Scanning Electron Microscopy, thermogravimetric analysis, and an element analyzer. The obtained activated carbons were further used to study the equilibrium and dynamic adsorption of carbon dioxide, which was performed in a fixed bed column by adsorption of carbon dioxide/nitrogen mixture. The collected data were analyzed to construct the breakthrough curves and breakthrough parameters for evaluating the adsorption dynamic performance.

1.3.2 Investigation of the behavior of carbon dioxide adsorption in slit pore model using GCMC simulation

Gas adsorption simulation of carbon dioxide and nitrogen was performed in Visual Basic Studio 2010 using Fortran compiler. A slit pore model with the absence and presence of a sodium hydroxide functional group was performed for gas adsorption. The mesoporous model was used to simulate gas adsorption by varying the pore width of the graphitic layer. The presence of sodium hydroxide functional groups was generated by randomly placing them with a random number. The molecular simulation results were also compared against the experimental data.

1.3.3 Development of experimental design and simulation-based optimization approach

An adaptive Latin hypercube sampling technique was applied to build process modeling of three case studies: methanol production via carbon dioxide hydrogenation, ammonia production, and carbon dioxide capture using the Rectisol process. These cases were simulated in Aspen HYSYS process simulator V10.1. Artificial Neural networks were used as surrogate models. The objective of simulation-based optimization of three case studies is to minimize the cost of the process. The prediction accuracy of the adaptive Latin hypercube sampling technique was compared with the existing sampling technique.

1.4 Output of Research

First, the expected output of the research is to produce an alkali impregnated activated carbon from longan seed for enhancing carbon dioxide adsorption. The effects of porous properties of activated carbon and sodium hydroxide loading are investigated to obtain an efficient adsorbent for carbon dioxide adsorption in a fixed bed column. It was demonstrated that sodium hydroxide impregnation in a mesoporous activated carbon could promote carbon dioxide adsorption capacity. Second, the molecular simulation results can be employed to gain an insight into the behavior of carbon dioxide adsorption in activated carbon impregnated with sodium hydroxide solution. Finally, an adaptive Latin hypercube sampling technique can be used as a sampling generation tool for optimization algorithms to predict the best optimal solutions of any response surface. It is expected that an adaptive Latin hypercube sampling technique will be more efficient than existing sampling techniques.

1.5 Organization

The dissertation consists of 6 chapters. The detail of each chapter is briefly provided here.

Chapter 1 Introduction

This chapter provides the introduction, objectives, scope and limitation, research output, and the dissertation's structure.

Chapter 2 The dynamic adsorption of CO_2 in a fixed bed of longan-based activated carbon with NaOH loading

An investigation of the performance of CO_2 adsorption in a fixed bed by microporous and mesoporous activated carbon from longan seed biomass impregnated with NaOH solution is presented in this chapter. The optimal conditions for providing the maximum CO_2 adsorption capacity are also determined using RSM.

Chapter 3 Investigation the behavior of CO_2 adsorption by NaOH impregnated logan seed activated carbon using GCMC

This chapter provides the impact of pore sizes of activated carbon on their adsorption performance and the proportion amount of NaOH molecules on the carbon surface to prevent early pore blockage. The CO_2 adsorption at high pressure was studied. The simulation model of CO_2 adsorption was performed using the Grand Canonical Monte Carlo (GCMC) simulation.

Chapter 4 Process configuration studies of methanol production via carbon dioxide hydrogenation: process simulation-based optimization using artificial neural networks

Three configurations of methanol production via CO_2 hydrogenation were studied to compare the methanol production cost. The simulation models were performed using Aspen HYSYS simulator. The performance of ANNs for simulation-based optimization is provided in this chapter.

Chapter 5 Adaptive Latin hypercube sampling for a surrogate-based optimization with artificial neural network

This chapter proposes an adaptive Latin hypercube sampling technique to use as a sampling technique for sample point generation in computer experimental design. The simulation-based optimization with an artificial neural network model was applied to investigate the minimum production cost corresponding to the optimal conditions of three different case studies.

Chapter 6 Conclusions and Recommendations

The final chapter summarizes the important results derived from the dissertation. The scopes of future work are also proposed in this chapter.

1.6 References

Aghel, B., S. Janati, S. Wongwises and M. S. Shadloo (2022). Review on CO_2 capture by blended amine solutions. International Journal of Greenhouse Gas Control 119: 103715.

Avula, X. J. R. (2003). Mathematical Modeling. Encyclopedia of Physical Science and Technology (Third Edition). R. A. Meyers. New York, Academic Press: 219-230.

Bowker, M. (2019). Methanol Synthesis from CO_2 Hydrogenation. ChemCatChem 11(17): 4238-4246.

Chen, J., J. Yang, G. Hu, X. Hu, Z. Li, S. Shen, M. Radosz and M. Fan (2016). Enhanced CO_2 Capture Capacity of Nitrogen-Doped Biomass-Derived Porous Carbons. ACS Sustainable Chemistry & Engineering 4(3): 1439-1445.

Chen, S., Q. Yue, B. Gao, Q. Li, X. Xu and K. Fu (2012). Adsorption of hexavalent chromium from aqueous solution by modified corn stalk: A fixed-bed column study. Bioresource Technology 113: 114-120.

Li, B., Y. Duan, D. Luebke and B. Morreale (2013). Advances in CO_2 capture technology: A patent review. Applied Energy 102: 1439-1447.

Metz, B., O. R. Davidson, H. d. Coninck, M. Loos, L. Meyer and I. P. o. C. C. R. S. W. Group (2005). Carbon dioxide capture and storage.

Mohammad, N. K., A. Ghaemi and K. Tahvildari (2019). Hydroxide modified activated alumina as an adsorbent for CO_2 adsorption: Experimental and modeling. International Journal of Greenhouse Gas Control 88: 24-37.

Mohd Azmi, N. Z., A. Buthiyappan, A. A. Abdul Raman, M. F. Abdul Patah and S. Sufian (2022). Recent advances in biomass based activated carbon for carbon dioxide capture – A review. Journal of Industrial and Engineering Chemistry 116: 1-20.

Montgomery, D. C. (2017). Design and analysis of experiments, John wiley & sons.

Mukherjee, A., J. A. Okolie, A. Abdelrasoul, C. Niu and A. K. Dalai (2019). Review of post-combustion carbon dioxide capture technologies using activated carbon. Journal of Environmental Sciences 83: 46-63.

Naksusuk, S. and C. Tangsathitkulchai (2019). Carbon Dioxide Capture in a Fixed Bed of Coconut Shell Activated Carbon Impregnated With Sodium Hydroxide: Effects of Carbon Pore Texture and Alkali Loading. Engineering Journal 23(4): 29-48.

Nanda, S., A. K. Dalai, F. Berruti and J. A. Kozinski (2016). Biochar as an Exceptional Bioresource for Energy, Agronomy, Carbon Sequestration, Activated Carbon and Specialty Materials. Waste and Biomass Valorization 7: 201-235.

Phothong, K., C. Tangsathitkulchai and P. Lawtae (2021). The Analysis of Pore Development and Formation of Surface Functional Groups in Bamboo-Based Activated Carbon during CO_2 Activation. Molecules 26: 5641.

Russell, L. M. (2014). 5.11 - Carbonaceous Particles: Source-Based Characterization of Their Formation, Composition, and Structures. Treatise on Geochemistry (Second Edition). H. D. Holland and K. K. Turekian. Oxford, Elsevier: 291-316.

Tan, Y. L., M. A. Islam, M. Asif and B. H. Hameed (2014). Adsorption of carbon dioxide by sodium hydroxide-modified granular coconut shell activated carbon in a fixed bed. Energy 77: 926-931.

Tidona, B., C. Koppold, A. Bansode, A. Urakawa and P. Rudolf von Rohr (2013). CO_2 hydrogenation to methanol at pressures up to 950 bar. The Journal of Supercritical Fluids 78: 70-77.

Zander, S., E. L. Kunkes, M. E. Schuster, J. Schumann, G. Weinberg, D. Teschner, N. Jacobsen, R. Schlögl and M. Behrens (2013). The Role of the Oxide Component in the Development of Copper Composite Catalysts for Methanol Synthesis. Angewandte Chemie International Edition 52(25): 6536-6540.

CHAPTER II

THE ADSORPTION DYNAMIC OF CO_2 IN A FIXED BED OF LONGAN–SEED ACTIVATED CARBON IMPREGNATED WITH NaOH LOADING

2.1 Abstract

CO_2 adsorption from simulated flue gas in a fixed-bed column using microporous and mesoporous activated carbon derived from longan-seed biomass, which were impregnated with NaOH, was investigated in this study. The volume ratio of microporous and mesoporous (V_{mic}/V_{mes}), adsorption temperature, NaOH loading, gas feed rate, and the adsorbent amount were considered as the process variables. All five process variables affected the two important breakthrough parameters including breakthrough time (t_B), which corresponds to CO_2 adsorption capacity at breakthrough time (q_B), with different trends and degrees. The NaOH loading only showed a characteristic of an optimum loading that provided the maximum of the breakthrough parameters. The results showed that the amount of CO_2 approximately increased 45% could be achieved with the activated carbon impregnated with around NaOH 1 weight % solution as compared to the case of the non-impregnated carbon. The relationship between the breakthrough parameters and process variables was studied by applying the response surface methodology (RSM). The maximum predicted q_B of 33.58 mg/g was derived at the NaOH loading of 76.5 mg/g carbon, V_{mic}/V_{mes} of 2.83, adsorption temperature of 20°C, gas feed rate of 156 kg/m^2-h and adsorbent amount of 51 kg/m^2 of column cross-section area. The CO_2 breakthrough curves could be described well by Klinkenberg's breakthrough model. The analysis of the two model parameters including the affinity constant (K) and the effect pore diffusivity (D_e) showed that the optimum V_{mic}/V_{mes} that provided the maximum K value was around 2.90, corresponding to the activated carbon that contains 74% and 26% by volume of micropores and mesopores, respectively. The maximizing of CO_2 adsorption in a fixed- bed adsorption system related to the proper volume ratio of micropores and mesopores along with alkali

addition into activated carbon.

2.2 Introduction

Carbon dioxide (CO_2) is the major greenhouse gas that contributes to global warming. CO_2 has a substantial long-term impact on global climate change and extreme weather phenomena such as storms, droughts, and flooding (Rosado, 2020; Pagani, Huber et al., 2014). One of the main causes of CO_2 emissions into the atmosphere is the burning of fossil fuels in power plants and industrial sectors (Russell 2014; Nanda, Dalai et al., 2016). The capture and utilization of carbon dioxide are becoming increasingly important as atmospheric CO_2 concentrations rise. Pre-combustion, post-combustion, and oxy-combustion techniques are among the CO_2 capture technologies that are currently in use (Mukherjee et al., 2016; Metz et al., 2005). Alternative strategies for more economically and efficiently capturing CO_2 are being actively investigated by researchers. There are four primary processes that are frequently employed in post-combustion capture technology: membrane-based separation, cryogenic separation, adsorption, and absorption (Li et al., 2013).

The high CO_2 removal efficiency of liquid amines has led to a widespread application of CO_2 capture by absorption in recent years. (Ooi et al., 2020; Adeyemi et al., 2017; Kikkawa et al., 2022; Aghel et al., 2022). However, this process has few drawbacks, including high corrosion, high power consumption for amine recovery, and high operating expenses (Ma'mum et al., 2005). Alternatively, the use of solid adsorbents for CO_2 capture by adsorption has become an interesting choice. Adsorption is an attractive technology for a number of reasons, including relatively low adsorbent costs, process simplicity, low energy consumption for adsorbent regeneration, and high capture efficiency (Sun et al., 2021; Mohd Azmi et al., 2022). A widely used porous adsorbent with a high internal surface area and adsorption capacity is activated carbon. Either chemical or physical activation can be used to prepare it. According to its numerous advantageous qualities, activated carbon presents a feasible alternative for CO_2 adsorption. (Mohd Azmi et al., 2022). Activated carbon can be produced from a variety of agricultural waste materials, such as coconut shells (Huang et al., 2015; Chen et al., 2016; Naksusuk and Tangsathitkulchai, 2019; Jaber et al., 2022), rice husks (Xu et

al., 2014; Hanum et al., 2017), and sawdust (Oladimeji et al., 2021; Rahman et al., 2022). Physical activation typically involves heating the precursor in the absence of oxygen, a process known as carbonization, which converts the precursors into charcoal. A network of interconnected pores and channels that expands the carbon surface area is created when the resulting charcoal is activated in the presence of an oxidizing gas, such as carbon dioxide or steam. When a precursor is subjected to a chemical activation method, such as soaking it in phosphoric acid or potassium hydroxide, it is carbonized in an inert atmosphere, resulting in the dehydration and intercalation processes to produce interior pores. (Tan et al., 2014).

Generally, these activated carbon adsorbents contain a high proportion of micropores, which make them effective for carbon dioxide adsorption due to strong interaction forces in narrow pores. Researchers are investigating strategies to enhance the porosity characteristics of the adsorbents by utilizing various preparation procedures in order to further increase their adsorption capacity (Mohd Azmi et al. 2022). The use of adsorbent materials with more active basic sites is advantageous for increasing the adsorption capacity and selectivity of CO_2 acid gas. Impregnating an adsorbent with a basic or alkali substance is a commonly used technique for adding basic sites to its surface. Several researchers have reported the favorable effects of many impregnant solutions on carbon dioxide adsorption capacity, such as sodium hydroxide (Tan et al., 2014; Dehkordi et al., 2022), potassium hydroxide (Mohammad et al., 2019; Tu et al., 2020), metal oxides (Bhatti et al., 2023), and amine solutions (Masinga et al., 2022).

The main purpose of the present work is to investigate the capture performance of CO_2 from a simulated flue gas by adsorption in a fixed bed of NaOH impregnated activated carbon prepared from longan seed biomass. Activated carbons with varying proportionate volumes of micropores and mesopores, temperature at which adsorption occurs, gas feed rate, amount of adsorbent, and NaOH loading were the variables studied. The response surface methodology (RSM) was applied to the adsorption data in order to identify the optimal conditions for providing the maximum CO_2 adsorption capacity. The design of experiments (DoE) was utilized to statistically ascertain the number of process variables necessary for conducting the adsorption experiment. Furthermore, the significance of the proportionate quantities of micropores and

mesopores on the ability to transport and adsorb carbon dioxide in a fixed bed of activated carbon was emphasized.

2.3 Fixed-Bed Adsorption Theory

The adsorption dynamic of a continuous fixed-bed operation can be assessed by collecting the concentration of adsorbate at the column exit (C) as a function of time (t) until the adsorbate concentration approaches the inlet concentration (C_0). The plot of C/C_0 on the Y-axis vs t on the X-axis is called the breakthrough curve, which generally assumes a characteristic of an S-shaped curve. The slope and position on the time scale of the breakthrough curve are used to evaluate the performance of fixed-bed adsorption. The higher the slope, the lower the mass transfer resistance of transporting the adsorbate through internal pores, whereas a longer period on the time scale indicates stronger adsorption affinity, and hence a larger adsorption capacity. The characteristic parameter for the time scale of the breakthrough curve is the breakthrough time (t_B) which is defined as the time at which the concentration ratio C/C_0 is equal to 0.05. The breakthrough time indicates the maximum allowable operating time before the regeneration of the adsorbent bed. The equilibrium time (t_E) is when C/C_0 is equal to 0.95, by which time the bed is fully saturated with the adsorbate molecules.

The adsorption capacity at t_B (q_B) and t_E (q_E) can be calculated, respectively, from the breakthrough data by the following equations.

$$q_B = \left(\frac{C_0 Q}{w}\right)\int_0^{t_B}\left[1-\frac{C}{C_0}\right]dt \tag{2.1}$$

and

$$q_E = \left(\frac{C_0 Q}{w}\right)\int_0^{t_E}\left[1-\frac{C}{C_0}\right]dt \tag{2.2}$$

where C is the outlet concentration of the adsorbate, C_0 is the inlet concentration of the adsorbate, w is the weight of adsorbent, and Q is the volumetric

flow rate of the feed stream. The integral terms in Equations (2.1) and (2.2) represent the area above the breakthrough curve at time t_B and t_E, respectively.

The degree of bed saturation at t_B can be estimated as the percentage ratio of q_B and q_E, as shown in Equation (2.3).

$$\% \text{ bed saturation} = 100\left(\frac{q_B}{q_E}\right) \tag{2.3}$$

The length of mass transfer zone (MTZ) at t_B, which is the bed length at the breakthrough time where adsorption is taking place, can be computed by Equation (2.4).

$$L_{MTZ} = L_B\left(\frac{t_E - t_B}{t_E}\right) \tag{2.4}$$

where L_{MTZ} is the length or width of mass transfer zone and L_B is the bed height.

The breakthrough equation proposed to predict the breakthrough curve in this work is the Klinkenberg's equation for long bed. It is the simplest breakthrough model that is based on the linear driving force (LDF) concept with negligible axial dispersion effect (Ruthven 1984). The equation reads

$$\frac{C}{C_0} = \frac{1}{2}\left[1 + \text{erf}\left(\sqrt{\tau} - \sqrt{\xi} + \frac{1}{8\sqrt{\tau}} + \frac{1}{8\sqrt{\xi}}\right)\right] \tag{2.5}$$

where the dimensionless terms: $\xi = k_p K L_B(1-\varepsilon_b)/u\varepsilon_b$ and $\tau = k_p[t-(L_B/u)]$, where k_p = particle-mass transfer coefficient(s^{-1}), K = Henry's constant of linear isotherm (dimensionless), L_B = bed height (m), ε_b= bed porosity, u = gas interstitial velocity (m/s), and t = time (s).

The term k_PK is related to the external and internal mass transfer resistances which are characterized by the film mass transfer coefficient (k_C) and the effective pore diffusivity (D_e), respectively, as follows:

$$\frac{1}{k_PK} = \frac{R_P}{3k_C} + \frac{R_P^2}{15D_e} \tag{2.6}$$

The film mass transfer coefficient (k_c) can be estimated from the correlation of Sherwood number with correction for axial dispersion as proposed by Wakao and Funazkri (Wakao and Funazkri, 1978), as shown in Equation (2.7).

$$N_{Sh} = \frac{k_C d_P}{D_m} = 2 + 1.1\left(\frac{d_P G}{\mu}\right)^{0.6}\left(\frac{\mu}{\rho D_m}\right)^{\frac{1}{3}} \tag{2.7}$$

where d_P is particle diameter (1.095 mm in the present work), D_m is molecular diffusivity of the diffusing species, G is the mass velocity of gas, μ is fluid viscosity, and ρ is fluid density. Equation (2.6) is used to compute D_e with the known values of k_c, k_P, K and particle radius (R_p).

2.4 Materials and Methods

2.4.1 Raw Material Preparation

The raw material used in this study was longan seed which is the inner round black seed of longan fruit. It was purchased from a fruit processing factory in the region of Chiangmai in northern Thailand. After giving the longan seed a thorough rinse with deionized water, it was left overnight to dry at 110°C in an electric oven. The pre-dried sample was crushed and sieved to obtain an average particle size of 1.095 mm (16x18 mesh). This particle size was selected, as compared to the adsorption column diameter of 10 mm, to provide reasonable void volume of the adsorbent bed for sufficient contact time between particles and the gas stream and to prevent excessive bed pressure drop and possibly the carryover of particles out of the column. Sodium

hydroxide in pellet form (99.00 weight % AR grade) was supplied by QREC, New Zealand. Nitrogen gas (99.995 vol% purity) and carbon dioxide (99.99 vol% purity) were supplied by Thai Special Gas and Linde, Thailand, respectively.

2.4.2 Raw Material Characterization

The moisture content, fixed carbon, volatile matter, and ash content of the longan seed were determined by the method of proximate analysis, using a thermogravimetric analyzer (TGA/DSC-1 Star System, Mettler-Toledo, Greifensee, Switzerland) and the heating program set by the ASTM method (D7582-15, 2015). In addition, an ultimate analysis was ascertained using a CHN analyzer (CHN628, Leco Corporation, St. Joseph, MI, USA) to determine the weight percentage of carbon, hydrogen, and nitrogen. The oxygen content in weight % was derived by the equation, O(wt%) = 100 – C(wt%) – H(wt%) - N(wt%).

A thermogravimetric analyzer (TGA/DSC-1 Star System, Mettler-Toledo, Greifensee, Switzerland) was used to analyze the thermal degradation behavior of longan seed. The weight loss of the sample was continuously recorded as a function of time while 22.31 mg of longan seed particles were heated at a rate of 5°C/min from room temperature to 950°C. The end results were displayed as a TG curve, which indicated how the weight percentage remaining changed depending on the heating temperature or heating time, and a DTG curve, which displayed the TG curve's first derivative, which represented the rate at which the heated sample decomposed.

2.4.3 Activated Carbon Preparation

2.4.3.1 Microporous Activated Carbon

A horizontal tube furnace (CTF 12/75/700, Carbolite, Staffordshire, UK) was used to heat about 40 g of longan seed from room temperature to 550°C at a heating rate of 10°C/min while keeping a constant flow of nitrogen gas (100 cm^3/min). The temperature was held at this value for 90 minutes to produce char, which was labeled as C550-90. The sample of char was then activated using CO_2 in a quartz tube that was placed in a vertical tube furnace (30 mm ID and 1200 mm length) and heated to 850°C for one hour. This microporous activated carbon that was initially produced (named AC850-1) was used to prepare a series of microporous carbon by activating it under different activation times and temperatures. Each derived carbon

product was designated as ACX-Y, where AC is the activated carbon prepared by the two-step carbonization/activation method at the activation temperatures of X (850°C or 900°C), and activation time Y in hour. The initial microporous activated carbon (AC850-1) was also used to prepare two types of mesoporous activated carbon, using the OTA method as described in the next section.

2.4.3.2 Mesoporous Activated Carbon

Two samples of mesoporous activated carbons were produced using the OTA preparation technique (Lawtae and Tangsathitkulchai, 2021). About 15 g of activated carbon were initially produced by the two-step activation method at the activation temperature and time of 850°C and 1 h, respectively. The prepared activated carbon (AC850-1) was then oxidized in a quartz tube reactor by heating the sample from ambient temperature to 230°C in a stream of air flowing at 100 cm^3/min and held at this temperature for 12 h in order to form additional oxygen functional groups on the carbon surfaces. Next, the oxidized carbon was heated under N_2 gas (100 cm^3/min) at 900°C for 2 h to remove most of the surface functional groups, thus leading to the increase in the surface reactivity due to the creation of a number of unpaired electrons caused by chemical bond disruption. The resulting activated carbon was then re-activated with CO_2 at 850°C for another 1 h to create a greater mesopore volume by the widening of the pre-existing micropores, as well as the creation of new micropores, thereby completing the first cycle of the OTA method. The resulting mesoporous carbon was designated as AC-OTA1. The OTA method was further applied for the second cycle on the AC-OTA1 to produce the mesoporous carbon with increased porous properties, and the resulting carbon product was designated as AC-OTA2.

2.4.4 NaOH Impregnated Activated Carbon Preparation

To prepare activated carbon samples impregnated with NaOH, 3 g of the activated carbon sample (either microporous AC or mesoporous AC) were mixed with 20 cm^3 of NaOH solution with the desired concentration in weight % of NaOH solution, thus the NaOH loading in mg NaOH/g carbon could then be computed. The resulting mixture was shaken at room temperature in a temperature-controlled water bath using a shaking speed of 150 rpm for 120 min to ensure that an equilibrium condition was attained. Subsequently, the entire suspension was dried in an electric oven at 110°C

for 24 h. The prepared alkali-impregnated carbon was designated by the type of activated carbon followed by the weight % of NaOH used in the impregnation. For example, for impregnation with 1 weight % NaOH solution, the sample codes were given as AC850-1-1 and AC-OTA1-1 for the microporous and the mesoporous activated carbons, respectively.

2.4.5 Porous Properties of Activated Carbon

The porous properties of the prepared activated carbon samples were computed from the measured adsorption/desorption isotherms of nitrogen at -196°C using a high-performance adsorption analyzer (3Flex, Micromeritics, Norcross, GA, USA). Prior to the isotherm measurement, the sample was degassed at 300°C under vacuum pressure for 12 h. The isotherm data were measured at increasing pressure up to 1 atm at the temperature of -196°C. The specific BET surface area (S_{BET}) was determined using the Brunauer-Emmett-Teller (BET) equation (Gregg, Sing et al. 1967) based on the isotherm data for the relative pressure (P/P°) ranging from 0.05 to 0.25, where P° is the saturation vapor pressure of N_2 at -196°C, which is equal to 1 atm. The total pore volume (V_{tot}) was first derived from the volume of nitrogen adsorbed at a relative pressure of 0.98 and then converted to the volume of liquid nitrogen at -196°C. The micropore volume (V_{mic}) was calculated using the Dubinin-Raduskevich equation (Misra 1969) for pore sizes smaller than 2.0 nm. The mesopore volume, which refers to pore sizes larger than 2.0 nm, was obtained by subtracting the micropore volume from the total pore volume. Finally, the average pore diameter was calculated using the equation $4V_{tot}/S_{BET}$, assuming a cylindrical-shaped pore. Pore size distribution data of the activated carbon samples were also provided by the adsorption analyzer based on the DFT theory.

2.4.6 CO_2 Adsorption Isotherms

The measurement of CO_2 adsorption isotherms was conducted on the activated carbon samples using a high-pressure volumetric analyzer (HPVAII, Micromeritics, Norcross, GA, USA) at 0°C (273 K) as a function of pressure up to the saturation vapor pressure of 3500 kPa. Prior to the measurement, the activated carbon sample was subjected to degassing at 300°C for 12 h under a high vacuum to remove any moisture and residual substances which may have been present in the activated carbon.

2.4.7 Dynamic of CO_2 Adsorption in a Fixed-Bed Column

The study of CO_2 adsorption in a fixed bed of activated carbon was carried out in an acrylic column of 1 cm in diameter and 60 cm in height. The experimental setup of the adsorption system is displayed in Figure 2.1. The adsorption experiment commenced by loading the known amount of carbon sample into the column and nitrogen gas was allowed to flow in for ten minutes to purge the column. Next, the feed gas consisting of 13% CO_2 and 87% N_2 by volume, which simulates the average composition of flue gases burning a solid fuel (Song, Pan et al., 2004), was introduced into the column from the bottom and the exit concentration of CO_2 was then recorded as a function of time using a gas analyzer (BIOGAS 5000, Geotech, UK) until the exit concentration approached the inlet CO_2 concentration. The collected data between the CO_2 concentration at the column exit and the operation time were used to plot the breakthrough curves for the subsequent analysis of the fixed-bed adsorption performance.

The number of experiments for running the adsorption tests were chosen based on the design of experiments (DoE). The central composite design (CCD) was used in this work for the experimental design because previous reports have shown that only a small number of sample points can be used to provide an acceptable match between the experimental and predicted values by the tested models (Bezerra et al., 2008). The number of experimental runs (N) can be calculated from the relation, $N = 2^{k-1} + 2(2(k-1)) + 4$, where k is the number of decision (process) variables. With five decision variables being studied (k=5), a total of 36 experimental test runs were performed for studying the CO_2 adsorption in a fixed bed of activated carbon. In this work, the decision variables studied included the types of activated carbons as distinguished by the different proportional volumes of micropores and mesopores, adsorption temperature to check for the nature of adsorption forces (physical adsorption or chemical adsorption), total gas flow rate which determines the gas-solid contact time, amounts of activated carbon, and NaOH loading in the activated carbon. The results from the equilibrium adsorption study of CO_2, as outlined in section 2.5.5, demonstrated that the maximum adsorption capacity of CO_2 was achieved when the activated carbon was impregnated with 1 weight % NaOH solution. Therefore, the concentration of NaOH used in this work was chosen to cover the range from 0-2 % by weight of NaOH in the

solution, which is equivalent to the NaOH loading of 0-136 mg NaOH/g carbon. Three different adsorption temperatures of 20°C, 30°C, and 40°C were tested, by circulating water from a temperature-controlled water bath through the jacket of the adsorption column. The weights of activated carbon samples used for studying adsorption performance in the fixed-bed column were 4 g, 6 g, and 8 g, corresponding to the average bed height of 18, 34, and 46 cm, respectively. Table 2.1 summarizes the values of decision variables used in the present study.

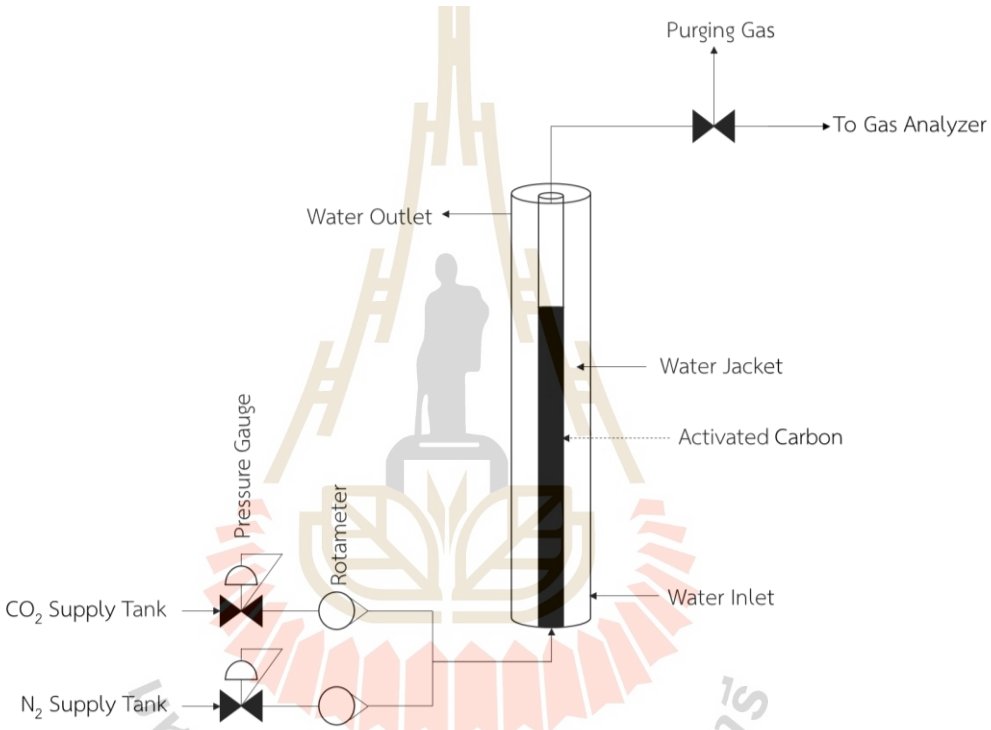

Figure 2.1 Experimental set up for the study of CO_2 adsorption in a fixed bed of activated carbon prepared from longan seed.

Table 2.1 Values of decision variables used for studying CO_2 adsorption in a fixed bed of activated carbon (using 3 g activated carbon in 25 cm^3 NaOH solution, and adsorption column ID of 1 cm)

Decision Variables [unit]		Value
X_1	V_{mic}/V_{mes} [-]	2.83 3.15 4.39 4.94
X_2	Adsorption temperature [°C]	20 30 40
X_3	Weight % of NaOH impregnant solution (NaOH loading, [mg NaOH/g carbon])	0 (0) 1 (67) 2 (136)
X_4	Total gas flow rate [kg/m^2-h] (Gas velocity, [m/s])	124 (0.021) 135 (0.023) 156 (0.026)
X_5	Amount of activated carbon [g] (Amount of activated carbon per column cross-section area, [kg/m^2])	4 (51) 6 (76) 8 (102)

2.5 Results and Discussion

2.5.1 Precursor Characterization

2.5.1.1 Thermal Decomposition Behavior of Longan Seed Precursor

Figure 2.2 shows the typical residual weight (TG) and its first derivative (DTG) resulting from the thermal decomposition of longan seed. The first small peak of the DTG curve appeared at 110°C and this was attributed to the vaporization of residual moisture from the longan seed, resulting in about 8% weight loss at this temperature, as observed from the TG curve. The following major peak occurred over the temperature range of 280 to 360°C which corresponded to the main devolatilization process caused by the decomposition of cellulose and hemicellulose (Guo and Lua 2001). The maximum devolatilization rate of the longan seed over this temperature range occurred at 320°C. For the temperatures higher than 360°C, a slow

decrease in the decomposition rate and the weight remaining was observed, giving a final weight remaining of about 20% at 850°C.

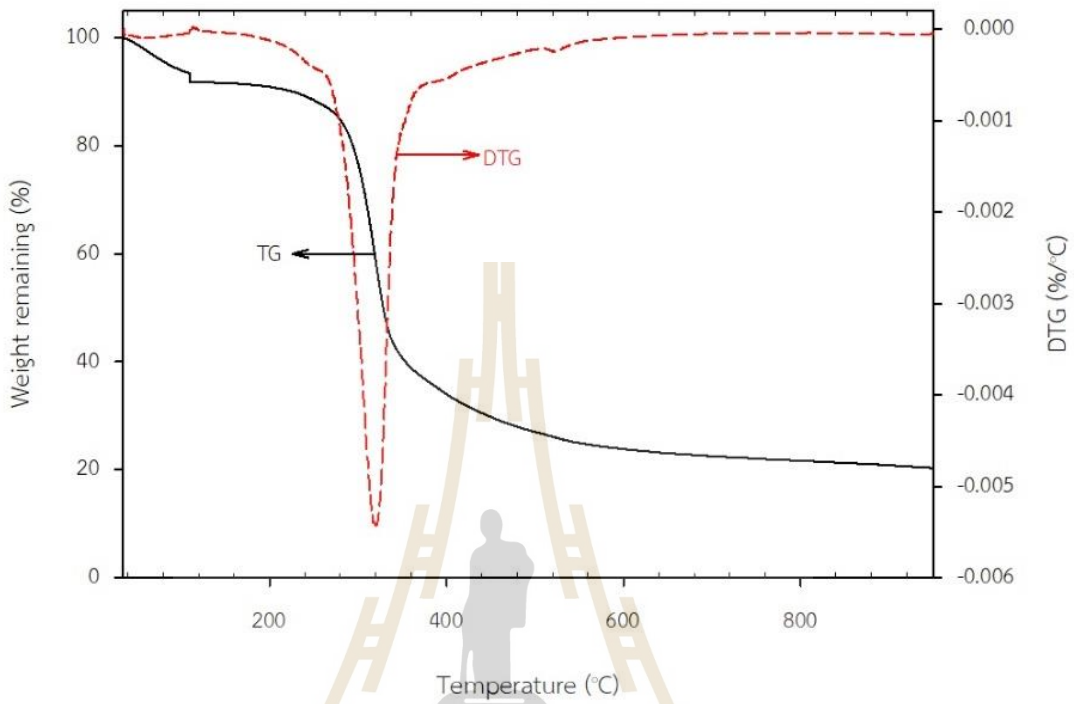

Figure 2.2 TG and DTG curves of longan seed used as the raw material in this work.

2.5.1.2 Proximate and Ultimate Analyses of Longan Seed Precursor

The results of proximate analysis of longan seed precursor used in this study are shown in Table 2.2. The fixed carbon of longan seed is 18.47 weight %, with a relatively low ash content of 0.06 weight %. The volatile matter content is quite high at 73.34 weight %, which is typical of most agricultural biomass. The % fixed carbon of longan seed precursor can be compared with other different biomasses, for example, 19.80% for oil palm shell (Guo and Lua, 2001), 19.40% for coconut shell (García et al., 2012), 16.50% for peanut shell, and 14.60% for corn cob (García et al., 2012). Results from the ultimate analysis indicate that carbon and oxygen are the major elements of the longan seed biomass which is in line with the compositions of fixed carbon and volatile matter of the proximate analysis, respectively.

Table 2.2 Proximate and ultimate analyses of longan seed precursor used in this work

Proximate Analysis	Weight %
Moisture	8.18
Volatile matter	73.34
Fixed carbon	18.47
Ash	0.06
Ultimate Analysis	**Weight %**
C	43.05
H	6.43
N	1.02
O (by difference)	44.50

2.5.2 Surface Morphology of the Prepared Activated Carbons

Figure 2.3 shows the surface images of the prepared activated carbons obtained from scanning electron microscopy (model JSM-7800F, JEOL, Tokyo, Japan). Columns a1, a2 and a3; b1, b2 and b3; c1, c2 and c3; and d1, d2 and d3 indicate the different concentrations of NaOH solution of 0, 1, and 2 weight%, respectively, while the rows from top to bottom (a to d) denote the types of activated carbon samples: AC850-2, AC900-3, AC-OTA1, and AC-OTA2, respectively. It can be observed that as the number of cycles of the OTA method increased (c1 vs d1) or more severe activation conditions in the two-step activation method were applied (a1 vs b1), an increase in the average pore size and number of pores was clearly observed. For the same activation time of one hour, the mesoporous carbon prepared by the OTA method (c1 for AC-OTA1) provided a greater pore volume than that of the microporous carbon produced by the two-step activation (a1 for AC850-2). This proves the effectiveness of the OTA method for increasing the amounts of mesopores in activated carbon. Additionally, after the impregnation process, there was visible evidence for the dispersion of NaOH particles on the surface of the activated carbon, with the number of NaOH particles appearing to increase with the increase of NaOH solution concentration from 0-2 weight%, corresponding to the loading of 0-136 mg NaOH/g

carbon. Furthermore, as the NaOH loading increased (rows a to c), the width of the pore mouth appeared to be narrower. It was expected that at a very high NaOH loading, the pore entrance would be fully covered with the deposited layer of NaOH particles. Figure 2.4 depicts the SEM images, elemental spectra, and X-ray mapping of a typical NaOH loaded carbon (AC-OTA2-1 sample). The spectra revealed a major carbon peak which resulted from the graphene structure of the activated carbon, while the peaks of sodium and oxygen atoms pertained to the sodium hydroxide molecules, thus confirming the presence of NaOH inside the pore structure of the activated carbon.

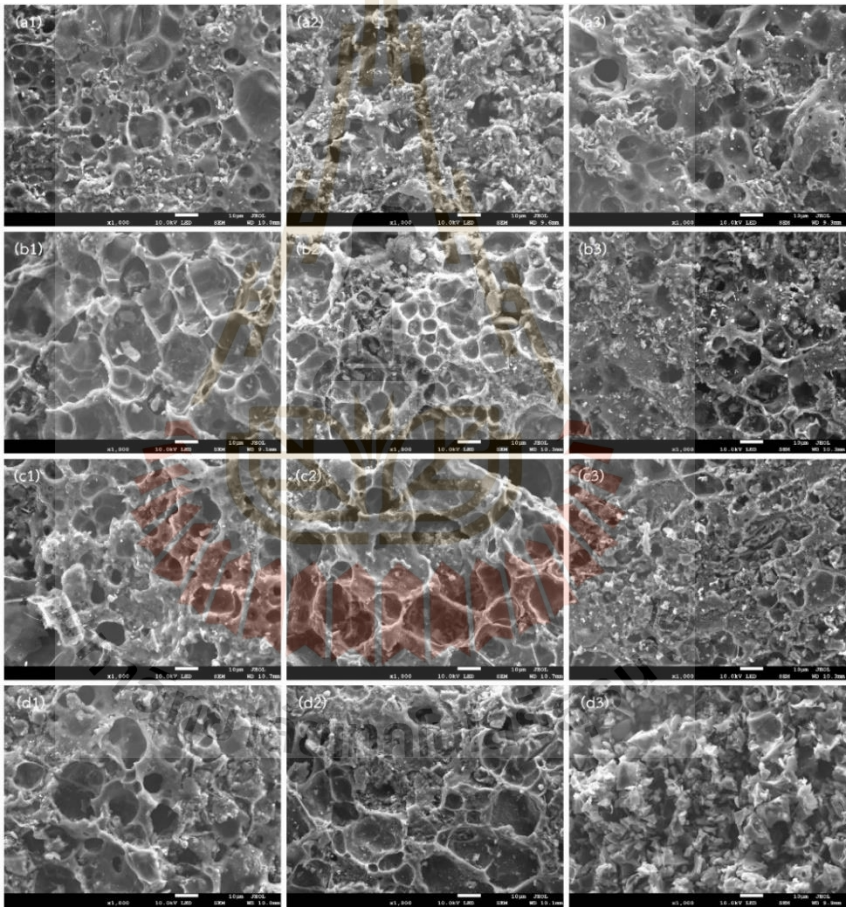

Figure 2.3 SEM micrographs of prepared activated carbons; series (a), (b), (c), and (d) stands for AC850-2, AC900-3, AC-OTA1, and AC-OTA2, respectively, with magnification of 1K. The columns a1-a3, b1-b3, c1-c3 and d1-d3 indicate the different concentrations of NaOH solution of 0, 1, and 2 weight%, respectively.

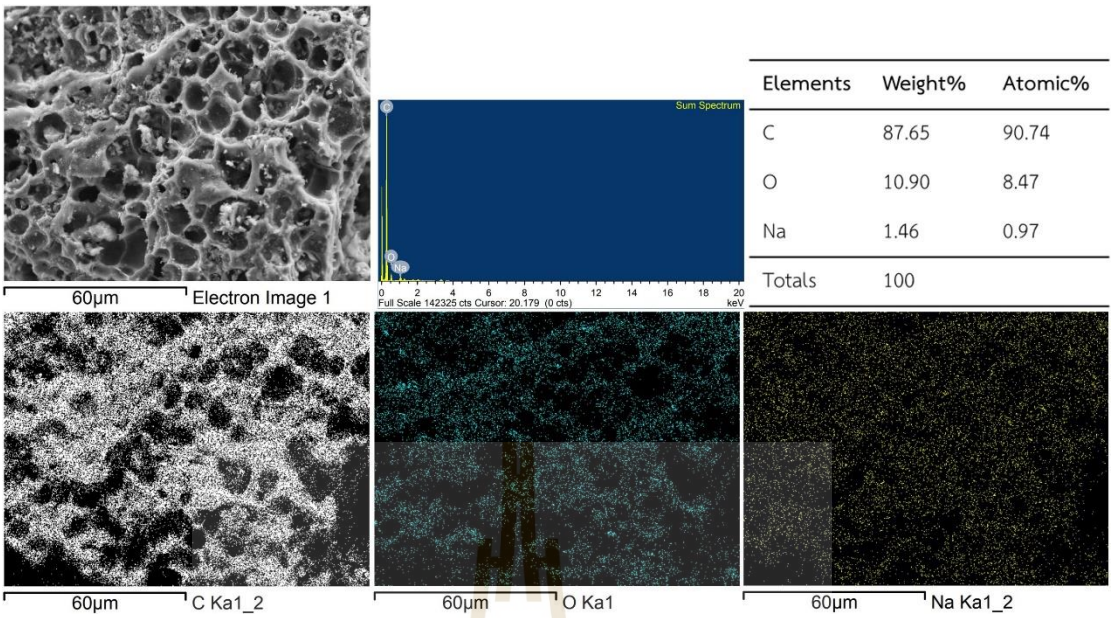

Elements	Weight%	Atomic%
C	87.65	90.74
O	10.90	8.47
Na	1.46	0.97
Totals	100	

Figure 2.4 Results of SEM-EDX analysis of sample AC-OTA2-1.

2.5.3 N_2 Adsorption/Desorption Isotherms of Prepared Activated Carbon

Figure 2.5 shows the effects of carbon type and NaOH loading on the adsorption isotherms of N_2 measured at -196°C (77K). All isotherms show a characteristic of Type I isotherm, typified by a rapid increase of the amount adsorbed for relative pressures less than about 0.1, followed by Type II isotherm with a small hysteresis loop at higher relative pressures. The initial Type I isotherm indicated that the adsorption of N_2 took place in micropores by the pore filling mechanism, while the following Type II isotherm with a hysteresis loop indicated the layering adsorption in mesopores of varying sizes, with the presence of capillary condensation occurring over the relative pressures greater than 0.40. For the microporous carbon series, N_2 isotherm of AC850-2 was lower than that of AC900-3. This was attributed to the higher amounts of porous properties (surface area and pore volume) of AC900-3, resulting from the application of a higher activation time and temperature. Similarly, the amounts of N_2 adsorbed for the mesoporous carbon produced by the two-cycle OTA method (AC-OTA-2) were about 40% greater than that of the one-cycle treated sample (AC-OTA-1). As to the effect of NaOH loading, there was a general tendency for the isotherms to decrease with increasing amounts of NaOH impregnation. This could have resulted from the presence of NaOH molecules that could block some of the small pores or occupying

the free surface area available for N_2 adsorption. The lowering of N_2 adsorption due to the increase of NaOH loading tended to become less for the mesoporous carbons, mainly because of their greater pore volume that could lower the pore blocking effect. When comparing the mesoporous carbon and microporous carbon series prepared under the same activation time and temperature (AC-OTA-1 vs AC850-2), it was observed that the mesoporous carbons prepared by the OTA method were able to adsorb larger amounts of N_2. This confirms the benefit of the OTA method over the conventional two-step activation for producing activated carbon with high porous properties.

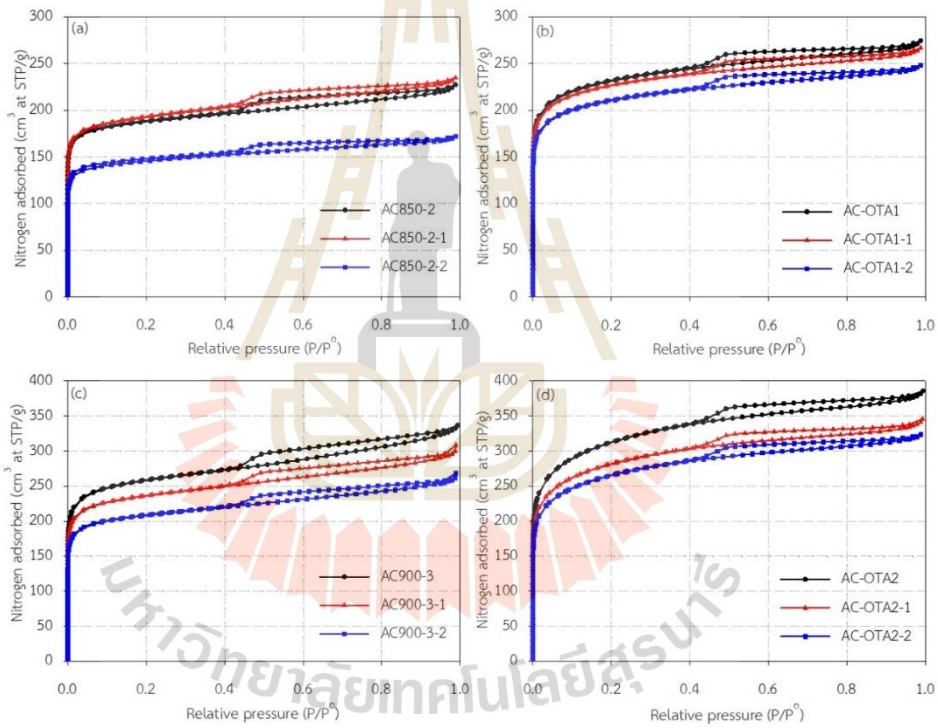

Figure 2.5 N_2 adsorption/desorption isotherms of microporous activated carbons prepared by the conventional activation method, (a) and (c), and mesoporous activated carbons prepared by the OTA method, (b) and (d).

2.5.4 Porous Properties of Prepared Activated Carbon

Table 2.3 displays porous properties of the prepared activated carbons. For the microporous carbon series, the use of higher activation time and temperature gave rise to an increase in the surface area and pore volume of the produced activated carbon, as well as the increasing percentage of mesopore volume, for example, comparing AC900-3 vs AC850-2. Similar results were obtained with the mesoporous carbons prepared by the OTA method in that the two-cycle treatment sample (AC-OTA2), having a longer activation time, had higher porous properties than those of the carbon product produced by the one-cycle OTA method (AC-OTA1). In addition, the surface area and pore volume of AC-OTA2 were about 2.5 times greater than those of the original microporous activated carbon (AC850-1). Furthermore, using the same activation time and temperature, activated carbon prepared by the OTA method had greater porous properties as compared to those of the carbon produced by the conventional two-step activation (comparing AC-OTA1 vs AC-850-2). For both the microporous and mesoporous carbon series, the increase of NaOH loading into the carbon pores by increasing the concentration of NaOH solution from 1 to 2 weight% caused a decrease in the free surface area and pore volume, as well as the average pore size, as would be expected.

The effect of adding an impregnant on porous properties of porous adsorbents prepared from various precursors is noteworthy and Table 2.4 presents the results. Similar to the results derived from the present study, the increase of concentration of an impregnant solution results in the decrease of available surface area which is clearly attributed to the occupation of the impregnant molecules on the adsorbent surfaces. The majority of these adsorbents also shows a decrease in the average pore size as the impregnant concentration is increased, due chiefly to the pore blocking effect caused by the increasing thickness of deposited layer of the impregnant molecules. The different percentage in the variation of porous properties caused by the addition of an impregnant among these adsorbents should depend primarily on the differences in their pore size distributions and pore connectivity.

Figure 2.6 shows typical plots of pore size distributions of the activated carbon products. The microporous activated carbon samples, without (AC850-2) and with NaOH impregnation (AC850-2-1 and AC850-2-2), show a distribution of pore sizes

covering the ranges from 0.50-0.65 nm, 0.65-1.0 nm and 1.0-2.0 nm. The order of decreasing in the amounts of pore volume (area under the curve) with reference to pore sizes is as follows, (0.50-0.65 nm) > (0.65-1.0 nm) > (1.0-2.0 nm). The decrease in the volume of 0.50-0.65 nm pore size as the NaOH loading increased from 0-2 weight% indicated that NaOH molecules resided mostly in this pore size range. Fig. 6(d) – 6(f) show the pore size distributions of mesoporous carbon series that cover the pore size ranges of 0.5-0.65, 0.65-1.0, 1.0-2.0 and 2.0-5.0 nm. A decrease in the volume of pore sizes in the range of 0.65-1.0 nm was notably observed. The accumulation of impregnant molecules in a larger pore size range of the mesoporous carbon, as compared with the case of microporous carbon (0.50-0.65 nm) indicates the significant role of mesopore size ranges in mitigating the early pore blocking by the impregnant molecules in narrow pores.

มหาวิทยาลัยเทคโนโลยีสุรนารี

Table 2.3 Porous properties of prepared activated carbons calculated from N_2 adsorption/desorption isotherms at -196°C

Sample	S_{BET} (m^2/g)	V_{tot} (cm^3/g)	V_{mic} (cm^3/g)	V_{mes} (cm^3/g)	V_{mic}/V_{mes}	Average pore diameter (nm)
AC850-1 (original AC)	481	0.2243	0.1967 (87.69%)	0.0277 (12.31%)	7.10	1.86
AC850-2	676	0.3402	0.2829 (83.16%)	0.0573 (16.84%)	4.94	2.01
AC850-2-1	693	0.3532	0.2883 (81.62%)	0.0649 (18.38%)	4.44	2.04
AC850-2-2	525	0.2597	0.2214 (85.25%)	0.0382 (14.75%)	5.79	1.98
AC900-3	934	0.5008	0.3803 (75.94%)	0.1206 (24.06%)	3.15	2.14
AC900-3-1	852	0.4501	0.3496 (77.67%)	0.1005 (22.33%)	3.48	2.11
AC900-3-2	751	0.3938	0.3088 (78.41%)	0.0850 (21.59%)	3.63	2.09
AC-OTA1	839	0.4132	0.3366 (81.46%)	0.0766 (18.54%)	4.39	1.97
AC-OTA1-1	820	0.4022	0.3284 (81.65%)	0.0738 (18.35%)	4.44	1.96
AC-OTA1-2	761	0.3756	0.3030 (80.67%)	0.0725 (19.33%)	4.18	1.97
AC-OTA2	1137	0.5791	0.4279 (73.89%)	0.1512 (26.11%)	2.83	2.04
AC-OTA2-1	1024	0.5162	0.3884 (75.24%)	0.1279 (24.76%)	3.04	2.01
AC-OTA2-2	964	0.4902	0.3640 (74.25%)	0.1262 (25.75%)	2.88	2.03

มหาวิทยาลัยเทคโนโลยีสุรนารี

Table 2.4 Effect of concentration of impregnant solution on porous properties of various porous adsorbents

Precursors	Impregnant	Impregnant concentration	S_{BET} (m^2/g)	Average pore diameter (nm)	References
Longan seed	- NaOH	0 1wt%	934 852	2.14 2.11	This work
Coconut shell	- NaOH	0 32%	788 378	2.89 4.12	Tan et al.
Coconut shell	- NaOH	0 3wt%	766 663	2.02 1.99	Naksusuk and Tangsathitkulchai
Activated alumina	- KOH	0 30%	- 92	- 10.31	Mohammad et al.
Coal	- NaOH	0 1M	915 614	2.3 3.4	Dehkordi et al.
Commercial AC	- Nickel oxide	0 10wt%	615 586	4.58 2.70	Bhatti et al.

มหาวิทยาลัยเทคโนโลยีสุรนารี

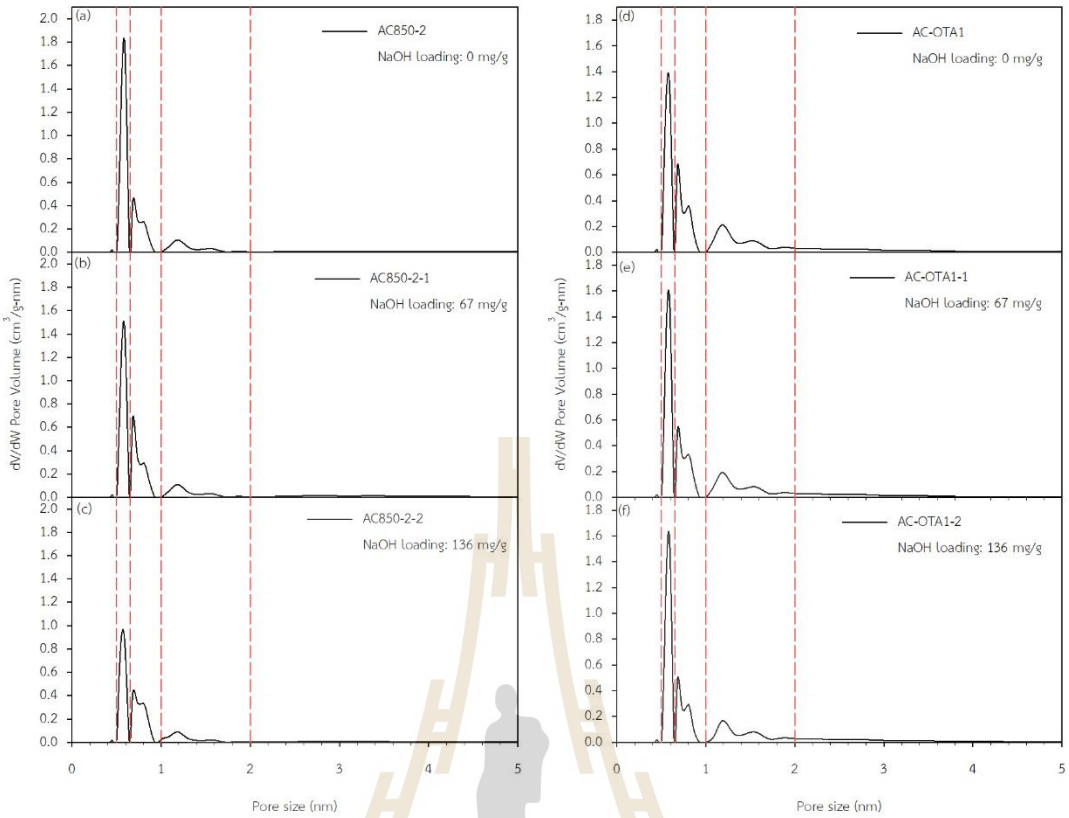

Figure 2.6 Pore size distributions of various activated carbon samples (a) – (c), the microporous carbon series and (d) – (f), the mesoporous carbon series, with varying NaOH loadings.

2.5.5 Experimental CO_2 Breakthrough Curves

Since the adsorption performance of CO_2 in a fixed bed of NaOH impregnated activated carbon depends on both the transport of CO_2 in pores and adsorption affinity of CO_2 molecules towards the carbon surfaces, we will first explore the effect of NaOH loading on the equilibrium adsorption of activated carbon without the complicating effect of mass transport through pores. Figure 2.7 shows the isotherm results for the microporous (AC850-2) and mesoporous carbon series (AC-OTA2). Sample AC850-2 which contains a larger percentage of micropores showed more or less Type I isotherm and the characteristic of Type I isotherm was more distinct with the increase of NaOH loading, due to the narrowing of pore width.

Isotherms of AC-OTA2 carbon series, with a larger average pore size, showed an initial part of the Type II isotherm, indicating that the adsorption of CO_2

occurred in both micropores and mesopores. It is interesting to observe that activated carbon samples impregnated with 1 weight % NaOH solution, which is equivalent to the NaOH loading of 67 mg NaOH/g carbon, yielded the maximum adsorbed amount of CO_2. This indicates that the presence of NaOH on the adsorbent surfaces could exert stronger NaOH-CO_2 interaction as compared to the interaction between CO_2 and carbon atoms in the graphene layers. As a result, increasing NaOH loading from 0-67 mg/g increased the number of NaOH adsorption sites, hence giving the increase in CO_2 adsorption. However, pore restriction at higher NaOH loadings will decrease the likelihood for CO_2 to arrive at the available inner adsorption sites, causing a significant drop in the isotherms. Next, we consider the CO_2 adsorption dynamic in a fixed-bed column.

Figure 2.8 shows the effects of process variables on the typical S-shaped breakthrough curves of CO_2 adsorption in a fixed-bed of the prepared activated carbons. Each variable exerted a definite effect but with different degrees on the slope and position on the time scale of the breakthrough curves. Although the effect of process variables on the slope of breakthrough curves was not clearly observed, there was a general tendency for the slope to increase for activated carbon with larger pore volume and pore size (AC900-3-1 vs AC850-2-1 and AC-OTA2-1 vs AC-OTA1-1 in Figure 2.8(a)), with increasing adsorption temperature (Figure 2.8(b)), with the decrease of NaOH loading (Figure 2.8(c)), and with the increase of gas velocity (Figure 8(d)). The increase in the slope of the breakthrough curve indicates the lowering of mass transfer resistance for the transport of adsorbate molecules from the bulk phase to the adsorption sites, hence the increase of transport flux of the adsorbate through the adsorbent pores. The effect of process variables on the time-scale position of the breakthrough curve is presented next in terms of the breakthrough time (t_B).

The effects of process variables on the various parameters of the breakthrough curve, including t_B, q_B, t_E, q_E, L_{MTZ}, and % bed saturation at t_B, are listed in Table 2.5 and presented in Figure 2.9 based on the respective conditions of the breakthrough curves shown in Figure 2.8. The values of these parameters reflect the performance of CO_2 adsorption by the carbon adsorbent in the fixed-bed adsorption unit. The effect of carbon type was expressed in terms of volume ratio of micropores and mesopores, V_{mic}/V_{mes}. As Figure 2.9(a) shows, there was a tendency for t_B and q_B to

remain relatively constant for the pore volume ratio of 2.83 to 4.40, but to decrease at higher ratios. This finding indicates that a porous carbon containing a relatively large proportion of micropores will lead to the drop in the CO_2 adsorption capacity due to the increase of pore resistance for transporting the adsorbate to the adsorption sites on the carbon surfaces. Next, increasing the adsorption temperature decreased both the values of t_B and q_B, as shown in Figure 2.9(b). This result signifies that the adsorption of CO_2 onto the NaOH impregnated carbon is considered as physical adsorption involving the intermolecular attractive forces between CO_2 and the carbon active sites. This is in agreement with the previous work reported by Tan et al. (2014) who studied the adsorption of carbon dioxide by sodium hydroxide-modified granular coconut shell activated carbon in a fixed bed over the temperatures ranging from 45-55°C.

As to the effect of NaOH loading (Figure 2.9(c)), it appeared that the loading of 67 mg NaOH/g carbon, corresponding to 1 weight% NaOH impregnant solution, provided roughly the maximum in t_B and q_B, with q_B being higher than that of the non-impregnated carbon by about 45%. This indicates that impregnating a porous carbon with an alkali agent helps increase the adsorption of an acid gas like CO_2. The higher alkali loading than the optimum value led to a drop in the adsorption capacity caused by the effect of pore restriction that slows down the diffusion rate of CO_2 molecules through pores to the adsorption sites. Similarly, a 50% increase in the adsorption capacity of CO_2 by the coconut-shell activated carbon loaded with NaOH has also been found (Naksusuk and Tangsathitkulchai, 2019). Increasing the gas feed rate, as shown in Figure 2.9(d), caused a decrease in the breakthrough time (t_B) due to the increasing velocity of the moving concentration front of the adsorbate inside the adsorbent bed. However, the adsorption capacity at t_B (q_B) was not much affected by the variation of gas flow rate, which indicates that increasing gas velocity does not exert any significant influence on the mass transfer resistance inside the carbon pores (intra-particle resistance) which in turn dictates the mass transport flux of CO_2 toward the adsorption surfaces and hence the adsorbed capacity. Figure 2.9(e) shows that increasing the amount of carbon adsorbent resulted in the increase of t_B but a decrease in the value of q_B. Larger amounts of adsorbent will allow a longer retention time for the concentration front of the adsorbate to travel inside the bed before emerging from the adsorption column, hence giving a longer breakthrough time. Definitely, the

increase in the amount of adsorbent will increase the amount of adsorbed CO_2. However, the value of q_B in the unit of mass of CO_2 adsorbed per carbon mass, for example g CO_2/g carbon, should be unchanged. It is speculated that the consistent decrease of q_B with the increase of adsorbent amount could result from the inconsistency in the packing characteristic of the particle bed such that the contact time between the gas flow in the void space and the adsorbent particles decreased with an increase in the amount of adsorbent.

It can be deduced from Table 2.5 that the effects of the five process variables, including carbon type, adsorption temperature, NaOH loading, gas feed rate and adsorbent amount, on the equilibrium time (t_E) and the adsorption capacity at the equilibrium time (q_E) followed the same trends as those observed for t_B and q_B. The percentage of bed saturation or bed utilization at the breakthrough time was not so sensitive to the variation of each process variables with the values varying in the somewhat narrow range of 86.2 to 93.9%. The width of mass transfer zone at t_B (L_{MTZ}) was obviously shorter than the bed height and its value varied with the change in the process variables in the same way as observed with the breakthrough time (t_B). The smaller value of L_{MTZ} indicates the steeper slope of the moving concentration front and hence giving better adsorption performance of the adsorbent bed.

Table 2.6 compares the adsorption capacity of CO_2 by various alkali-impregnated porous adsorbents in a fixed-bed operation. It is clear that the impregnation of an alkali agent is capable of increasing CO_2 adsorption by a relatively wide range from 23.7 to 357%, with the maximum increase being the adsorption by amine impregnated titanium oxides. It also appears that activated carbon produced from palm shell is able to adsorb CO_2 more than does the coconut-shell based activated carbon. This difference could be attributed to the differences in the pore structure and the number of adsorption sites distributing on the carbon surfaces. Definitely, many other factors such as bed porosity, particle size, CO_2 concentration, gas velocity, temperature, alkali loading, and pore size distributions can also be responsible for the efficiency of CO_2 capture in a fixed-bed of porous adsorbents.

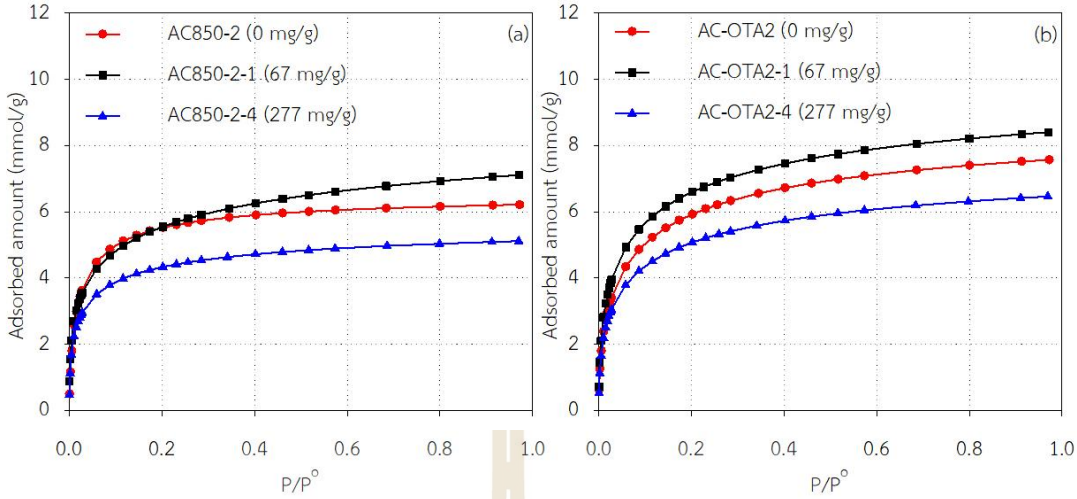

Figure 2.7 Effect of NaOH impregnation loading on CO_2 adsorption isotherms at 273 K (0°C) of longan-seed activated carbon, where P° is the saturation vapor pressure of CO_2 at 273 K (3.5 MPa), for (a) microporous carbon series and (b) mesoporous carbon series.

มหาวิทยาลัยเทคโนโลยีสุรนารี

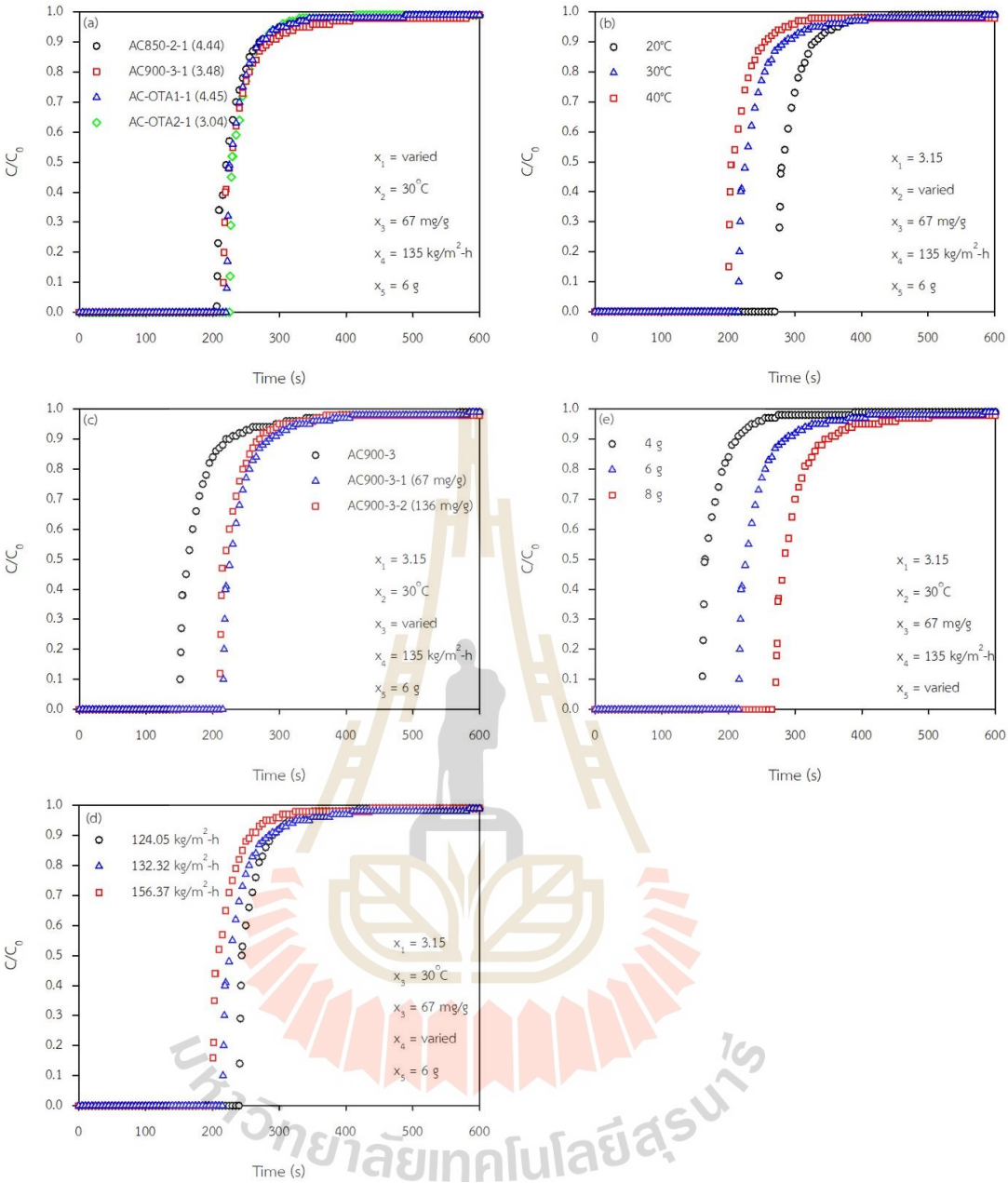

Figure 2.8 Effects of process variables on CO_2 breakthrough curves; (a) carbon type (X_1), (b) temperature (X_2), (c) NaOH loading (X_3), (d) gas feed rate (X_4), and (e) adsorbent amount (X_5).

Table 2.5 Effects of process variables on the breakthrough parameters of CO_2 adsorption in a fixed bed of longan-seed activated carbon (diameter of adsorption column = 1 cm)

Run no.	Sample	V_{mic}/V_{mes}	Adsorption temperature (°C)	NaOH concentration, wt% (mg/g)	Total gas flowrate (kg/m^2-h)	Adsorbent amount (g)	Bed height (cm)	Breakthrough time, t_B (sec)	Adsorption capacity at breakthrough time, q_B (mg/g)	Equilibrium time, t_E (sec)	Adsorption capacity at equilibrium time, q_E (mg/g)	%bed sat.at t_B	L_{MTZ} (cm)
1	AC-OTA2	2.83	20	0 (0)	124	8	45	323	26.1	398	27.2	95.9	8.66
2	AC-OTA2	2.83	20	0 (0)	156	4	22	163	33.2	243	36.8	90.2	7.76
3	AC-OTA2-2	2.83	20	2 (136)	124	4	22	173	29.0	297	32.4	89.5	8.79
4	AC-OTA2-2	2.83	20	2 (136)	156	8	45	290	29.1	378	31.1	93.4	10.15
5	AC-OTA2	2.83	40	0 (0)	124	4	22	137	21.0	207	23.1	91.0	7.94
6	AC-OTA2	2.83	40	0 (0)	156	8	45	212	20.2	278	21.5	94.1	11.52
7	AC-OTA2-2	2.83	40	2 (136)	124	8	45	250	18.9	323	19.9	94.8	9.12
8	AC-OTA2-2	2.83	40	2 (136)	156	4	22	121	23.1	193	25.9	89.0	7.67
9	AC850-2	4.94	20	0 (0)	124	4	22	185	30.1	273	33.0	91.1	5.98
10	AC850-2	4.94	20	0 (0)	156	8	45	292	30.4	447	34.0	89.6	13.80
11	AC850-2-2	4.94	20	2 (136)	124	8	45	302	24.6	488	27.4	89.7	13.51
12	AC850-2-2	4.94	20	2 (136)	156	4	22	128	26.3	248	32.6	80.8	8.88
13	AC850-2	4.94	40	0 (0)	124	8	44	277	20.9	358	22.1	94.1	9.94
14	AC850-2	4.94	40	0 (0)	156	4	22	118	23.0	197	26.3	87.6	8.83
15	AC850-2-2	4.94	40	2 (136)	124	4	22	126	19.8	216	22.8	86.7	7.32
16	AC850-2-2	4.94	40	2 (136)	156	8	45	179	17.3	307	20.3	85.3	16.48
17	AC-OTA2-1	2.83	30	1 (67)	135	6	33	226	24.5	298	26.1	93.9	8.15
18	AC850-2-1	4.94	30	1 (67)	135	6	33	208	22.9	308	25.4	90.3	8.88

Table 2.5 Effects of process variables on the breakthrough parameters of CO_2 adsorption in a fixed bed of longan-seed activated carbon (diameter of adsorption column = 1 cm) (continued)

Run no.	Sample	V_{mic}/V_{mes}	Adsorption temperature (°C)	NaOH concentration, wt% (mg/g)	Total gas flowrate (kg/m^2-h)	Adsorbent amount (g)	Bed height (cm)	Breakthrough time, t_B (sec)	Adsorption capacity at breakthrough time, q_B (mg/g)	Equilibrium time, t_E (sec)	Adsorption capacity at equilibrium time, q_E (mg/g)	%bed sat.at t_B	L_{MTZ} (cm)
19	AC900-3-1	3.15	20	1 (67)	135	6	33	275	31.6	359	33.7	93.9	7.46
20	AC900-3-1	3.15	40	1 (67)	135	6	33	203	22.4	288	24.1	92.6	9.76
21	AC900-3	3.15	30	0 (0)	135	6	33	153	17.0	294	19.7	86.2	14.74
22	AC900-3-2	3.15	30	2 (136)	135	6	33	212	24.7	307	26.8	92.0	9.66
23	AC900-3-1	3.15	30	1 (67)	124	6	33	240	25.2	318	26.8	93.9	8.26
24	AC900-3-1	3.15	30	1 (67)	156	6	33	202	26.7	283	29.1	91.9	9.53
25	AC900-3-1	3.15	30	1 (67)	135	4	22	163	28.0	238	30.6	91.6	6.75
26	AC900-3-1	3.15	30	1 (67)	135	8	45	271	23.3	403	25.6	91.2	13.14
27	AC-OTA1-1	4.40	20	1 (67)	135	6	33	264	31.3	542	35.3	88.8	16.94
28	AC-OTA1-1	4.40	40	1 (67)	135	6	33	203	22.5	293	24.3	92.7	10.17
29	AC-OTA1	4.40	30	0 (0)	135	6	33	210	24.1	288	25.9	93.0	9.15
30	AC-OTA1-2	4.40	30	2 (136)	135	6	33	208	23.9	298	25.9	92.1	9.03
31	AC-OTA1-1	4.40	30	1 (67)	124	6	33	238	24.8	313	26.4	93.8	7.87
32	AC-OTA1-1	4.40	30	1 (67)	156	6	33	196	25.9	278	28.1	92.1	9.41
33	AC-OTA1-1	4.40	30	1 (67)	135	4	22	161	27.7	243	30.5	90.9	6.93
34	AC-OTA1-1	4.40	30	1 (67)	135	8	45	289	24.7	378	26.1	94.4	10.58
35	AC900-3-1	3.15	30	1 (67)	135	6	33	215	24.5	333	27.2	90.1	11.22
36	AC-OTA1-1	4.40	30	1 (67)	135	6	33	221	25.2	303	27.0	93.1	9.00

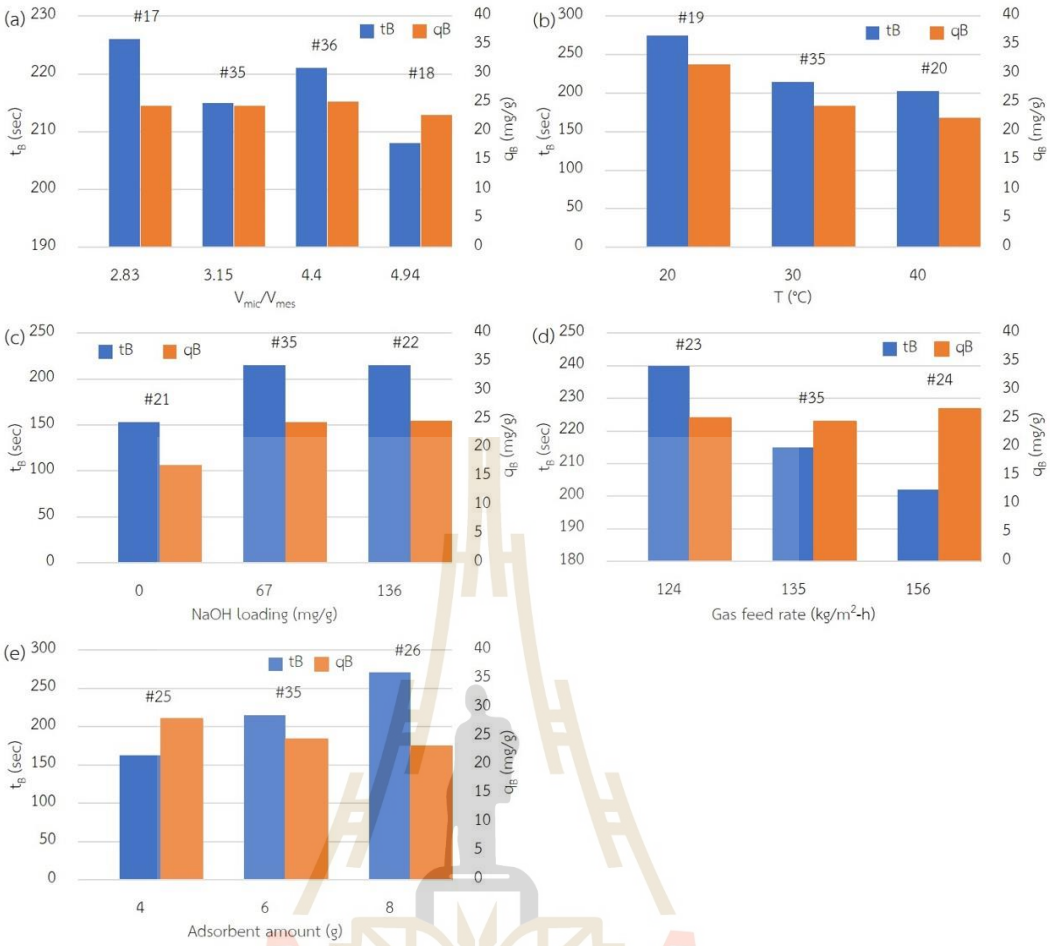

Figure 2.9 Effects of process variables on t_B and q_B for the adsorption of CO_2 in a fixed-bed of activated carbon; (a) X_2 = 30°C, X_3 = 67 mg/g, X_4 = 135 kg/m^2-h, X_5 = 76 kg/m^2 (6g), (b) X_1 = 3.15 kg/m^2-h, X_3 = 67 mg/g, X_4 = 135 kg/m^2-h, X_5 = 76 kg/m^2 (6g), (c) X_1 = 3.15, X_2 = 30°C, X_4 = 135 kg/m^2-h, X_5 = 76 kg/m^2-h (6g), (d) X_1 = 3.15, X_2 = 30°C, X_3 = 67 mg/g, X_5 = 76 kg/m^2 (6g) , (e) X_1 = 3.15, X_2 = 30°C, X_3 = 67 mg/g, X_4 = 135 kg/m^2-h.

Note: The symbol # represents Run no. in Table 2.5

Table 2.6 CO_2 adsorption capacity in a fixed bed of alkali-impregnated porous adsorbents

Type of adsorbent	Specific surface area (m^2/g)	CO_2 conc. in feed (vol%)	Adsorption temperature (°C)	Adsorption capacity (mg/g)			References
				Non-impregnated	Impregnated	% increase	
1.NaOH impregnated coconut shell AC	1052	13	35	22.8	32.1	40.8	Naksusuk & Tangsathitkulchai
2. Diethanol amine impregnated palm shell AC	800	40	40	75.0	92.8	23.7	Kongnoo et al.
3.NaOH impregnated coconut shell AC	787	20	35	17.5	27.3	56.0	Tan et al.
4.Palm shell AC impregnated with sterically hindered amine	822	30	40	37.1	64.0	72.5	Lee et al.
5.Amine impregnated titanium oxide	930	10	75	20.0	91.5	357	Ma et al.
6.NaOH modified activated alumina	207	15	35	19.6	51.9	165	Auta et al.

2.5.6 Development of Correlations for q_B and t_B by the RSM

The adsorption capacity at the breakthrough time (q_B) is an important breakthrough parameter for deciding the efficiency of CO_2 adsorption in a fixed bed of a porous adsorbent. In this work, the response surface methodology (RSM) was

employed to correlate q_B with the five process variables, leading to the determination of optimal conditions which provided the maximum adsorption capacity of CO_2. In applying the RSM, the central composite design (CCD) was used as a sampling technique for experimental design. Normally, the number of sample points of CCD consists of full factorial design point with an additional design of axial and center points. Generally, the full factorial design was mostly used as an experimental design for the first-order model regression. To reduce the time and cost for preparing the tested adsorbent, the section of the first-order regression was compiled with the second-order regression. Therefore, we decided to construct a test matrix with CCD. The objective function of this work is a second-order model that represents the relationship between process variables (X_i) and the breakthrough parameters (y). The second-order model equation is in the form of a polynomial type, as follows.

$$y = \beta_0 + \sum_{i=1}^{k} \beta_i X_i + \sum_{i=1}^{k} \beta_{ii} X_i^2 + \sum\sum_{i<j} \beta_{ij} X_i X_j \quad \text{when } k = 5 \qquad (2.8)$$

The adsorption experiments were carried out under the process conditions (X_i) generated by CCD. The following are the five X_i parameters: volume ratio between the activated carbon's micropores and mesopores (X_1), adsorption temperature (X_2), NaOH loading (X_3), gas supply flow rate (X_4), and the amount of adsorbent (X_5). Then, the values of the corresponding breakthrough time (q_B) and process conditions (X_i) were collected through the experiments. Regression analysis was then carried out using Design Expert 12 to fit the data to the second-order model. The second-order model was reduced to include only significant terms by considering only the terms with *p*-value less than 0.05 (where the level of significant (α) at 0.05 was considered). The final empirical equation for q_B is shown in
Equation (2.9),

$$q_B = 45.8727+0.9405X_1-1.5261X_2+0.1391X_3+0.0474X_4-0.0507X_5-0.0174X_1X_3+ 0.0185X_2^2-0.0006X_3^2 \qquad (2.9)$$

where $X_1=V_{mic}/V_{mes}$ (2.83-4.94), X_2=adsorption temperature (20-40°C), X_3=NaOH loading (0-136mg/g), X_4= gas flow rate (124-156 kg/m^2-h), X_5=amount of adsorbent (51-102 kg/m^2 of column cross-section area). The adjusted R^2 of this proposed equation is 0.828.

Next, Equation (2.9) was used as the objective function in the optimization problem and the Design Expert 12 was also employed to determine the maximum q_B. The optimization formulation is as follows.

Decision variables: X_i: i = 1, 2, 3, . . ., 5

MAX:

$$q_B = 45.8727+0.9405X_1-1.5261X_2+0.1391X_3+0.0474X_4-0.0507X_5-0.0174X_1X_3+0.0185X_2^2-0.0006X_3^2$$

Subject to:

$$2.83 \leq X_1 \leq 4.94$$

$$20 \leq X_2 \leq 40 \quad (°C)$$

$$0 \leq X_3 \leq 136 \quad (mg/g)$$

$$124 \leq X_4 \leq 156 \quad (kg/m^2\text{-}h)$$

$$51 \leq X_5 \leq 102 \quad (kg/m^2)$$

The adjusted R^2 of the equation of the derived q_B (max) is 0.8617.

Similarly, the RSM was applied to develop the empirical equation for the breakthrough time (t_B) and the final derived equation is shown in the following equation, with the adjusted R^2 of 0.944.

$$t_B = 271.8539+7.8644X_1-9.1064X_2+1.2478X_3-1.0712X_4+3.4163X_5-0.1436X_1X_3-0.0348X_2X_5+0.1487X_2^2-0.0055X_3^2 \quad (2.10)$$

Table 2.7 shows the optimal adsorption conditions for achieving the maximum CO_2 adsorption at breakthrough time ($q_{B,max}$). The results indicate that the maximum adsorption of 33.58 mg/g was achieved under the adsorption conditions of 20°C, NaOH loading of 76.5 mg/g (corresponding to 1.14 weight% of NaOH impregnant solution), gas flow rate of 156 kg/m^2-h, adsorbent amount of 51kg/m^2, and V_{mic}/V_{mes} of 2.83. The adsorption experiment was then performed under these optimal conditions and the amount of CO_2 adsorbed was found to be 36.59 mg/g, thus giving a prediction error of about 8.23%. The predicted q_B for the non-impregnated carbon under the

optimal conditions was found to be 30.22 mg/g which was about 10% lower than the maximum estimated q_B of 33.58 mg/g.

The surface plots of q_B and t_B constructed from Equation (2.9) and Equation (2.10) are typically shown in Figure 2.10 and Figure 2.11, respectively. As Figure 2.10(a) shows, the maximum q_B of 33.58 mg/g was clearly observed at the optimal NaOH loading of 76.5 mg NaOH/g carbon. Figure 2.10(b) shows that the increase of adsorption temperature lowered the amount of CO_2 adsorbed, while q_B increased slightly with the increase of gas flow rate at a constant adsorption temperature. Figure 2.11(a) shows that the maximum of breakthrough time (t_B) also occurred at the same optimal NaOH loading of 76.5 mg/g as in the case of q_B. Furthermore, increasing the adsorption temperature decreased the breakthrough time (t_B), while t_B tended to continuously increase with the increase of the adsorbent amount because of the longer gas-adsorbent contact time, as shown in Figure 2.11(b).

Table 2.7 The optimal adsorption conditions that provide the maximum adsorption capacity of CO_2 at breakthrough time

Decision variables	Range	Optimal conditions	q_B (mg/g)	
			Experimental value	Predicted value
V_{mic}/V_{meso} (-)	2.83-4.94	2.83	36.59	33.58
Adsorption Temperature (°C)	20-40	20		
NaOH loading (mg/g)	0-136	76.5		
Total gas flow rate (kg/m^2-h)	124-156	156		
Adsorbent amount (kg/m^2)	51-102	51		
			8.23 % Error	

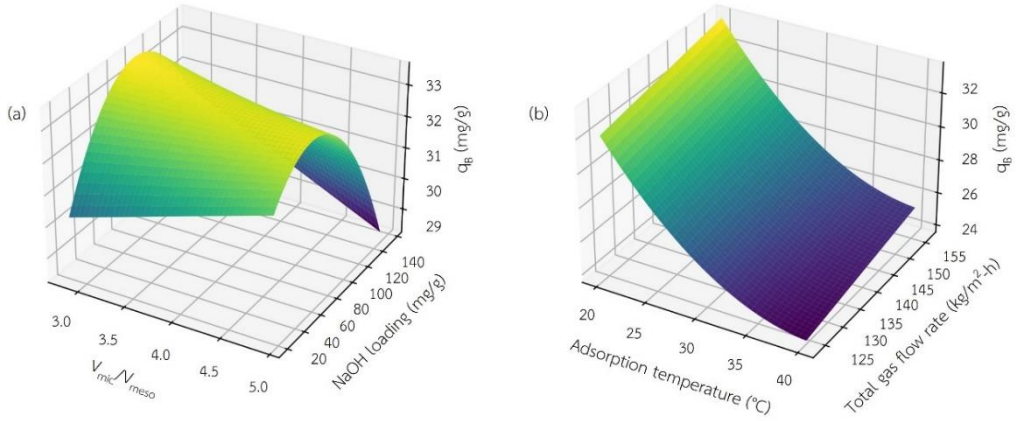

Figure 2.10 Typical response surface plots showing (a) the effect of NaOH loading and V_{mic}/V_{mes} on q_B for adsorption temperature of 20°C, total gas flow rate of 156 kg/m^2-h, and adsorbent amount of 51 kg/m^2, and (b) the effect of total gas flow rate and adsorption temperature on q_B for V_{mic}/V_{mes} of 2.83, NaOH loading of 76.5 mg/g, and adsorbent amount of 51 kg/m^2.

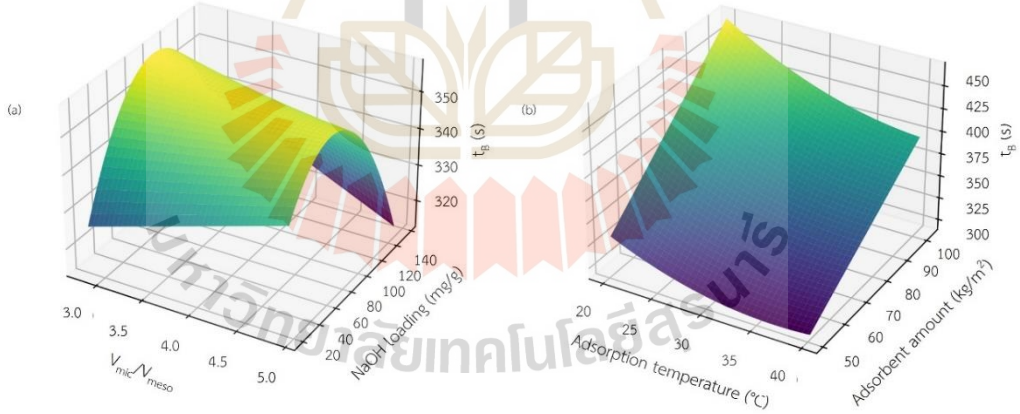

Figure 2.11 Typical response surface plots showing (a) the effect of NaOH loading and V_{mic}/V_{mes} on t_B for adsorption temperature of 30°C, total gas flow rate of 135 kg/m^2-h, and adsorbent amount of 76 kg/m^2, and (b) the effect of adsorbent amount and adsorption temperature on t_B for V_{mic}/V_{mes} of 2.83, NaOH loading of 76.5 mg/g, and total gas flow rate of 135 kg/m^2.

2.5.7 The Breakthrough Model

Figure 2.12 shows the comparison between the breakthrough curves derived from experiments and those from the model prediction. It is noted that the Klinkenberg's equation was able to predict the experimental breakthrough data for CO_2 adsorption accurately up to the exit concentration ratio (C/C_0) of around 0.80. However, the tested model overpredicted the experimental results at higher C/C_0 values. At this stage, there is no sound explanation for the overprediction of the breakthrough model at C/C_0 larger than 0.8, but it could result from the basic assumption of neglecting the axial-dispersion effect of the Klinkenberg's model. This hypothesis could be proved by trying a more sophisticated breakthrough model, but it would be rather tedious and time-consuming since a numerical solution is required. However, with a good match in the range of C/C_0 = 0-0.80 provided by the simple breakthrough model of Klinkenberg, the application of this model for the conceptual design of a fixed-bed adsorption unit should pose no difficulty, since the prediction of the breakthrough time, where the fixed bed operation needs to be stopped and the adsorbent regeneration is required, can be accurately achieved using breakthrough data over a much lower value of C/C_0 less than 0.05.

Figure 2.13 shows the effects of process variables on the model parameters, including k_p, K and D_e. It should be noted that both the particle-mass transfer coefficient (k_p) and the effective pore diffusivity (D_e) are the transport properties that measure the resistance for the diffusion of an adsorbate through carbon pores, whereas the Henry's constant of the linear isotherm (K) indicates the adsorbent-adsorbate affinity which is indicative of the adsorption capacity. It should be noted also that the adsorption capacity of a fixed-bed system will depend on how fast an adsorbate is transported to the adsorption sites, which depends primarily on the porous structure of an adsorbent, since the fixed-bed column operates in a dynamic or transient mode.

It is not surprising that the effect of the five process variables on the value of the Henry's constant (K) (Figure 2.13) followed the same trend as that observed for the adsorption capacity at breakthrough time (q_B), as previously discussed. This is because the adsorbent-adsorbate affinity is a direct indication of the adsorbed amount of an adsorbate. As shown in Figure 2.13(a), the increase in V_{mic}/V_{mes} gave rise

to the decrease in both k_p and D_e which is clearly the result of an increase in the mass-transport resistance in the pore space due to the increasing degree of pore restriction caused by the increasing amount of micropores. Increasing the adsorption temperature decreased both the values of k_p and D_e, as shown in Figure 2.13(b). This can be explained by the fact that the increase in temperature lowers the amount being adsorbed, thus limiting the transport flux of the adsorbate (CO_2) to the adsorption sites. Similar reasoning can be applied to explain the increase of k_p and D_e with the increase of NaOH loading from 0 to 67 mg/g which is due chiefly to the consequent increase in the number of active adsorption sites, as displayed in Figure 2.13 (c). The slight drop in the values of k_p and D_e with the increase of the gas feed rate, as shown in Figure 2.13 (d), was not expected since only the external film resistance around the adsorbent particles should be affected by the gas flow rate but not the internal mass transfer resistance of the porous material. The decrease of K by about 18% for the increasing amount of adsorbent from 4 to 8 grams, as shown in Figure 2.13(e), is hypothesized to result from the possible decrease of bed porosity that provides less contact time between the adsorbent and adsorbate and hence results in a decrease in the amount adsorbed. Again, this effect will then lower the transport rate of the adsorbate to the adsorption sites, thus causing a decrease in the values of k_p and D_e. The correlations between the breakthrough model's parameters (k_p and K) and the process variables were also developed, as shown in Equations.(11) and (12), respectively.

$$k_p = 3.7260-0.2290X_1+0.0104X_2-0.0022X_3-0.0179X_4+0.0096X_5 \qquad (2.11)$$

with the adjusted R^2 = 0.411

$$K = 81.3858+23.93499X_1-1.9592X_2+1.0710X_3+0.4059X_4-0.3413X_5-0.0024X_3^2-0.2341X_1X_3 \qquad (2.12)$$

with the adjusted R^2 = 0.788

It is interesting to explore further the role of the proportion of micropore volume with respect to mesopore volume on the kinetic and equilibrium of CO_2 adsorption in a fixed bed of a carbon adsorbent. Figure 2.14 shows the relationship

between K and D_e for all adsorption conditions which can be approximately fitted by the solid line of the following empirical equation, $K = 129.44+1.39\times10^{6}D_e - 1.83\times10^{10}D_e^{2}$ (where D_e is in the unit of m^2/s) from which the maximum K of 156 occurred at the effective pore diffusivity (D_e) of 3.8×10^{-5} m^2/s. It may be argued that the scattering of the data points is relatively large. However, the trend of the data as shown by the plotted curve can be explained by the following reasoning. To The optimal value of V_{mic}/V_{mes} of the carbon adsorbent corresponding to the D_e value of 3.8×10^{-5} m^2/s was read out from the plot of D_e vs V_{mic}/V_{mes}, as presented in Figure 2.15, and was found to be around 2.90. This value is close to the optimal value of 2.83 as predicted by the RSM analysis (Table 2.7). Therefore, a suitable activated carbon used for CO_2 capture in a fixed-bed mode should possess primarily the porous properties of about 74% micropore volume and the rest of 26% mesopore volume. This proportional pore volume will ensure a balance between a fast adsorption kinetic due to a reasonable amount of mesopores and a reasonably high adsorption capacity due to a sufficiently large surface area of micropores. Table 2.3 indicates that the optimal pore volume ratio (V_{mic}/V_{mes}) of 2.90 can be achieved with activated carbons prepared by the OTA method. Apart from having the proper volume ratio of micropores and mesopores, it is necessary to impregnate the carbon adsorbent with an appropriate amount of an alkali agent to maximize the capture of CO_2 by the adsorption process. Therefore, it can be inferred that the alkali impregnation and the proportional amounts of micropores and mesopores of activated carbon are the key parameters capable of controlling the adsorption efficiency of CO_2 in a fixed-bed adsorption system.

It should be noted that the expressions developed for t_B (Equation (2.10)), k_p (Equation (2.11)) and K (Equation (2.12)) combined with the breakthrough equation (Equation (2.5)) can be used for the conceptual design of a fixed-bed adsorption unit, that is, the computation of an adsorption column diameter (D_c), adsorbent bed height (L_B), and adsorbent weight (W). The calculation procedure is briefly illustrated as follows. The following data are generally provided for the adsorption unit design: volume flow rate of a treated gas mixture (Q), activated carbon with known porous properties ($X_1=V_{mic}/V_{mes}$), adsorption temperature (X_2), a selected NaOH loading (X_3), gas mass velocity (X_4), where $X_4 = Q\rho/A_c$, ρ =gas density, A_c= column cross-section area = $\pi D_c^2/4$, and D_c= column diameter. The known

parameters (X_1-X_4) along with the unknown amount of adsorbent in terms of X_5, where $X_5 = W/A_c = W/(\pi D_c^2/4)$, with $W = (\pi D_c^2/4)(L_B)(1-\varepsilon_b)\rho_s$, L_B=bed height, ε_b=bed porosity and ρ_s = density of adsorbent particles, are substituted into the equation of breakthrough time (Equation (2.10)). Next, substituting the various parameters in the breakthrough equation (Equation (2.5)), starting with k_p and K from Equations (2.11) and (2.12), respectively, the interstitial gas velocity (u) = $Q/A_c\varepsilon_b$, $C/C_0 = 0.05$, and $t = t_B$. We can then simultaneously solve the t_B equation (Equation (2.10)) and the breakthrough equation (Equation (2.5)) to obtain the column diameter (D_c) and the adsorbent bed height (L_B), from which the amount of the adsorbent required (W) can be finally derived.

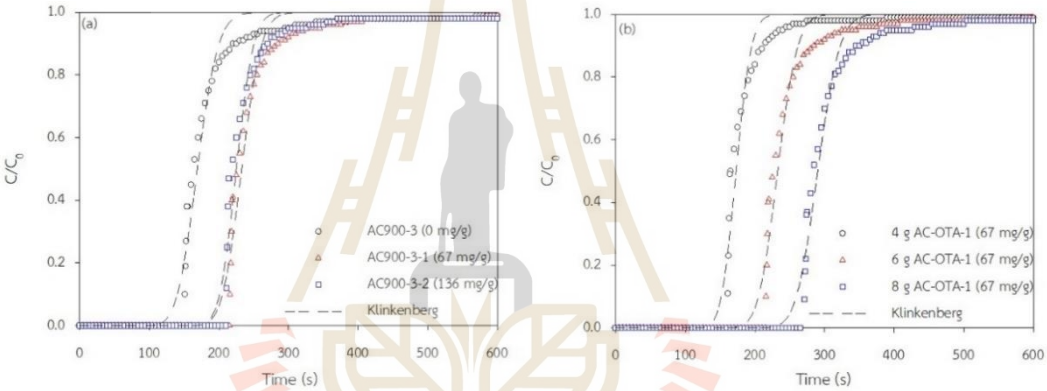

Figure 2.12 The fitting of the Klinkenberg's breakthrough equation to the experimental breakthrough data for, (a) Effect of NaOH loading (X_3) for X_1 = 3.15, X_2 = 30°C, X_4 = 135 kg/m^2-h, X_5 = 76(6) kg/m^2(g), and (b) Effect of adsorbent amount (X_5) for X_1 = 4.39, X_2 = 30°C, X_3 = 67 mg/g, X_4 = 135 kg/m^2-h.

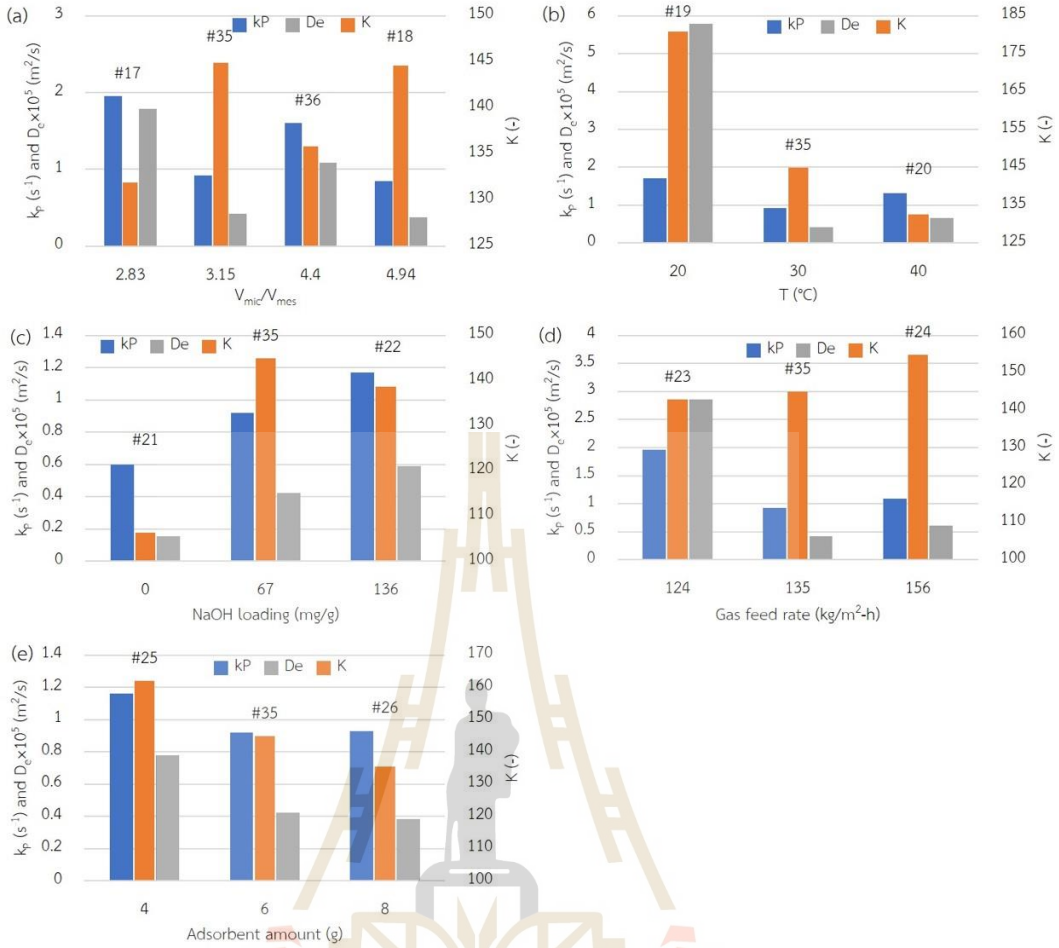

Figure 2.13 Effect of process variables on the breakthrough model parameters; (a) X_2 = 30°C, X_3 = 67 mg/g, X_4 = 135 kg/m^2-h, X_5 = 76 kg/m^2 (6g), (b) X_1 = 3.15, X_3 = 67 mg/g, X_4 = 135 kg/m^2h, X_5 = 76 kg/m^2 (6g), (c) X_1 = 3.15, X_2 = 30°C, X_4 =135 kg/m^2h, X_5 = 76 kg/m^2 (6g), (d) X_1 = 3.15, X_2 = 30°C, X_3 = 67 mg/g, X_5 = 76 kg/m^2 (6g), (e) X_1 = 3.15, X_2 = 30°C, X_3 = 67 mg/g, X_4 = 135 kg/m^2-h.

Note: The symbol # represents Run no. in Table 2.5

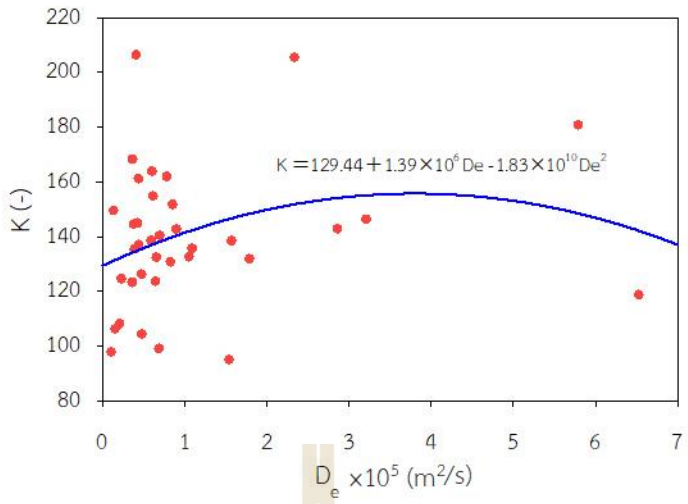

Figure 2.14 Relationship between Henry's constant of the linear isotherm (K) and pore diffusivity (D_e).

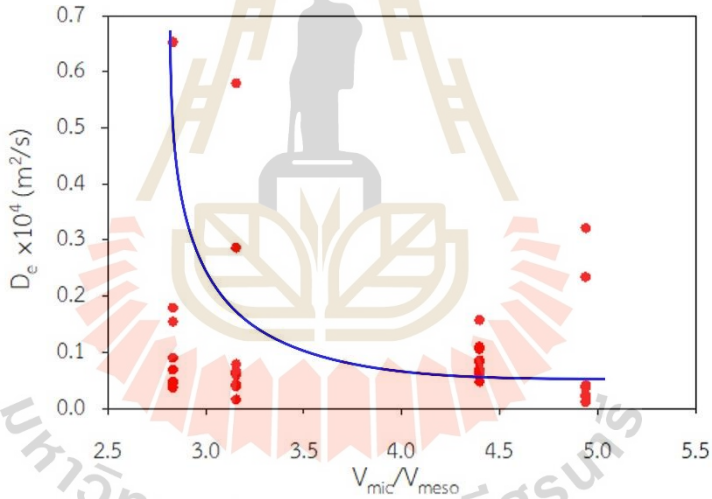

Figure 2.15 Effect of V_{mic}/V_{mes} on the effective pore diffusivity (D_e).

2.6 Conclusions

Carbon dioxide adsorption dynamic was investigated in a fixed bed of longan-seed based microporous and mesoporous activated carbons impregnated with sodium hydroxide. The variables affecting the breakthrough parameters were studied, including the carbon type as indexed by the volume ratio of micropores and mesopores (V_{mic}/V_{mes}), adsorption temperature, NaOH loading, gas feed rate and the amount of

adsorbent. The addition of NaOH into the prepared activated carbon increased the adsorption capacity of CO_2 up to about 45% in comparison with that of the non-impregnated carbon. Empirical correlations were developed for the two important breakthrough parameters, namely the breakthrough time and CO_2 adsorption capacity at the breakthrough time, based on the response surface methodology. It was found from the correlation that the maximum amount of CO_2 adsorption of 33.58 mg/g occurred at the NaOH loading of 76.5 mg/g carbon (equivalent to 1.14 g of NaOH per 100 g of NaOH solution), adsorption temperature of 20°C, V_{mic}/V_{mes} of 2.83, gas feed rate of 156 kg/m^2-h, and the adsorbent amount of 51 kg/m^2 of column cross-section area. The Klinkenberg's equation was capable of describing the experimental breakthrough curves reasonably well up to a CO_2 concentration ratio (C/C_0) of around 0.80. The relationship between the pore volume ratio (V_{mic}/V_{mes}) and the derived model parameters, the Henry's constant of the linear isotherm (K) for adsorbent-adsorbate affinity and the effective pore diffusivity (D_e) for mass-transport characterization, indicated that the optimal pore volume ratio for providing the maximum of K value was about 2.90 which corresponds to 74% of micropore volume and 26% of mesopore volume. The activated carbon that possesses this optimum pore volume ratio can be readily produced by the OTA method as proposed recently for the synthesis of a large-surface area mesoporous carbon adsorbent. It can be concluded that the most suitable activated carbon to be used for the maximum CO_2 adsorption in a fixed-bed column should contain the proper amounts of micropores and mesopores, coupled with the impregnation of activated carbon with an appropriate amount of an alkali agent.

2.7 References

Adeyemi, I, M R M Abu-Zahra and I Alnashef (2017) Novel green solvents for CO_2 capture. Energy Procedia 114: 2552-2560

Aghel, B, S Janati, S Wongwises and M S Shadloo (2022) Review on CO_2 capture by blended amine solutions. International Journal of Greenhouse Gas Control 119: 103715

Auta, M., N. D. Amat Darbis, A. T. Mohd Din and B. H. Hameed (2013). Fixed-bed column adsorption of carbon dioxide by sodium hydroxide modified activated alumina. Chemical Engineering Journal 233: 80-87.

Bezerra, M A, R E Santelli, E P Oliveira, L S Villar and L A Escaleira (2008) Response surface methodology (RSM) as a tool for optimization in analytical chemistry. Talanta 76(5): 965-977

Bhatti, A H, M Waris, W W Kazmi, U H Bhatti, G H Min, B C Park, S Kweon, I H Baek and S C Nam (2023) Metal impregnated activated carbon as cost-effective and scalable catalysts for amine-based CO_2 capture. Journal of Environmental Chemical Engineering 11(1): 109231

Chen, J, J Yang, G Hu, X Hu, Z Li, S Shen, M Radosz and M Fan (2016) Enhanced CO_2 capture capacity of nitrogen-doped biomass-derived porous carbons. ACS Sustainable Chemistry & Engineering 4(3): 1439-1445

Dehkordi, S S R, Q Delavar, H A Ebrahim and S S Partash (2022) CO_2 adsorption by coal-based activated carbon modified with sodium hydroxide. Materials Today Communications 33: 104776

García, R, C Pizarro, A G Lavín and J L Bueno (2012) Characterization of Spanish biomass wastes for energy use. Bioresource Technology 103(1): 249-258

Gregg, S J, K S W Sing and H Salzberg (1967) Adsorption surface area and porosity. Journal of The electrochemical society 114(11): 279Ca

Guo, J and A C Lua (2001) Kinetic study on pyrolytic process of oil-palm solid waste using two-step consecutive reaction model. Biomass and Bioenergy 20(3): 223-233

Hanum, F, O Bani and L I Wirani (2017) Characterization of activated carbon from rice husk by HCl activation and its application for lead (Pb) removal in car battery wastewater. IOP Conference Series: Materials Science and Engineering

Huang, P-H, H-H Cheng and S-H Lin (2015) Adsorption of carbon dioxide onto activated carbon prepared from coconut shells. Journal of Chemistry 2015: 106590

Jaber, L, I Ihsanullah, I W Almanassra, S N Backer, A Abushawish, A K A Khalil, H Alawadhi, A Shanableh and M A Atieh (2022) Adsorptive removal of lead and chromate ions from water by using iron-doped granular activated carbon

obtained from coconut shells. Sustainability 14 DOI: 10.3390/su141710877

Kongnoo, A., P. Intharapat, P. Worathanakul and C. Phalakornkule (2016). Diethanolamine impregnated palm shell activated carbon for CO_2 adsorption at elevated temperatures. Journal of Environmental Chemical Engineering 4(1): 73-81.

Kikkawa, S, K Amamoto, Y Fujiki, J Hirayama, G Kato, H Miura, T Shishido and S Yamazoe (2022) Direct air capture of CO_2 using a liquid amine–solid carbamic acid phase-separation system using diamines bearing an aminocyclohexyl group. ACS Environmental Au 2(4): 354-362.

Lawtae, P and C Tangsathitkulchai (2021) A new approach for controlling mesoporosity in activated carbon by the consecutive process of air oxidation, thermal destruction of surface functional groups, and carbon activation (the OTA Method). Molecules 26(9)

Lee, C. S., Y. L. Ong, M. K. Aroua and W. M. A. W. Daud (2013). Impregnation of palm shell-based activated carbon with sterically hindered amines for CO_2 adsorption. Chemical Engineering Journal 219: 558-564.

Li, B, Y Duan, D Luebke and B Morreale (2013) Advances in CO_2 capture technology: A patent review. Applied Energy 102: 1439-1447

Ma'mum, S, H F Svendsen, K A Hoff and O Juliussen (2005) Selection of new absorbents for carbon dioxide capture. Greenhouse Gas Control Technologies 7. E S Rubin, D W Keith, C F Gilboy et al. Oxford, Elsevier Science Ltd: 45-53

Ma, L., R. Bai, G. Hu, R. Chen, X. Hu, W. Dai, H. F. M. Dacosta and M. Fan (2013). Capturing CO_2 with Amine-Impregnated Titanium Oxides. Energy & Fuels 27(9): 5433-5439.

Masinga, T, M Moyo and V E Pakade (2022) Removal of hexavalent chromium by polyethyleneimine impregnated activated carbon: intra-particle diffusion, kinetics and isotherms. Journal of Materials Research and Technology 18: 1333- 1344

Metz, B, O R Davidson, H d Coninck, M Loos, L Meyer and I. P. o. C. C. R. S. W. Group (2005) Carbon dioxide capture and storage. Intergovernmental Panel on Climate Change (IPCC) Special Report. Cambridge University Press

Misra, D N (1969) Adsorption on heterogeneous surfaces: A dubinin-radushkevich equation. Surface Science 18(2): 367-372

Mohammad, N K, A Ghaemi and K Tahvildari (2019) Hydroxide modified activated alumina as an adsorbent for CO_2 adsorption: Experimental and modeling. International Journal of Greenhouse Gas Control 88: 24-37

Mohd Azmi, N Z, A Buthiyappan, A A Abdul Raman, M F Abdul Patah and S Sufian (2022) Recent advances in biomass based activated carbon for carbon dioxide capture – A review. Journal of Industrial and Engineering Chemistry 116: 1-20

Mukherjee, A, J A Okolie, A Abdelrasoul, C Niu and A K Dalai (2019) Review of post-combustion carbon dioxide capture technologies using activated carbon. Journal of Environmental Sciences 83: 46-63

Naksusuk, S and C Tangsathitkulchai (2019) Carbon dioxide capture in a fixed bed ofcoconut shell activated carbon impregnated with sodium hydroxide: Effects of carbon pore texture and alkali loading. Engineering Journal 23(4): 29-48

Nanda, S, A K Dalai, F Berruti and J A Kozinski (2016) Biochar as an exceptional bioresource for energy, agronomy, carbon sequestration, Activated Carbon and Specialty Materials. Waste and Biomass Valorization 7: 201-235

Oladimeji, T E, B O Odunoye, F B Elehinafe, O R Obanla and O A Odunlami (2021) Production of activated carbon from sawdust and its efficiency in the treatment of sewage water. Heliyon 7(1): e05960

Ooi, Z L, P Y Tan, L S Tan and S P Yeap (2020) Amine-based solvent for CO_2 absorption and its impact on carbon steel corrosion: A perspective review. Chinese Journal of Chemical Engineering 28(5): 1357-1367

Pagani, M, M Huber and B Sageman (2014) 6.13 - Greenhouse climates. Treatise on Geochemistry (Second Edition). H. D. Holland and K. K. Turekian. Oxford, Elsevier: 281-304

Rahman, N U, W Bahadar, S Alam, M Zahoor, I Zekker, F A Khan, R Ullah, E A Ali and H C A Murthy (2022) Activated sawdust-based adsorbent for the removal of basic blue 3 and methylene green from aqueous media. Adsorption Science & Technology 2022: 4551212

Rosado, H R a M R a P (2020) CO_2 and greenhouse gas emissions. Published online at OurWorldInData.org

Russell, L M (2014) 5.11 - Carbonaceous particles: Source-based characterization of their formation, composition, and structures. Treatise on Geochemistry (Second Edition). H D Holland and K K Turekian. Oxford, Elsevier: 291-316

Ruthven, D M (1984) Principles of adsorption and adsorption processes, John Wiley & Sons.

Song, C, W Pan, S T Srimat, J Zheng, Y Li, Y-H Wang, B-Q Xu and Q-M Zhu (2004) Tri-reforming of methane over Ni catalysts for CO_2 conversion to syngas with desired H_2/CO ratios using flue gas of power plants without CO_2 separation. Studies in Surface Science and Catalysis. S-E Park, J-S Chang and K.-W Lee, Elsevier. 153: 315-322

Sun, S, H Sun, P T Williams and C Wu (2021) Recent advances in integrated CO_2 capture and utilization: a review. Sustainable Energy & Fuels 5(18): 4546-4559

Tan, Y L, M A Islam, M Asif and B H Hameed (2014) Adsorption of carbon dioxide by sodium hydroxide-modified granular coconut shell activated carbon in a fixed bed. Energy 77: 926-931

Tu, B, R Wen, K Wang, Y Cheng, Y Deng, W Cao, K Zhang and H Tao (2020) Efficient removal of aqueous hexavalent chromium by activated carbon derived from Bermuda grass. Journal of Colloid and Interface Science 560: 649-658

Wakao, N and T Funazkri (1978) Effect of fluid dispersion coefficients on particle-to-fluid mass transfer coefficients in packed beds: Correlation of Sherwood numbers. Chemical Engineering Science 33(10): 1375-1384

Xu, H, B Gao, H Cao, X Chen, L Yu, K Wu, L Sun, X Peng and J Fu (2014) Nanoporous activated carbon derived from rice husk for high performance supercapacitor. Journal of Nanomaterials 2014: 714010

CHAPTER III

INVESTIGATION THE BEHAVIOR OF CARBON DIOXIDE ADSORPTION BY NaOH IMPREGNATED LONGAN SEED ACTIVATED CARBON USING GCMC

3.1 Abstract

Four types of activated carbon, containing two microporous activated carbon from two-step activation method and two mesoporous activated carbon from activation combined with oxidation method, were prepared for investigating the behavior of CO_2 adsorption under high pressure system. These activated carbons were impregnated with NaOH solution and then were used for carbon dioxide adsorption up to saturation pressure at 0°C. The NaOH solution was varied from 1 to 10 weight% with total impregnation method. The porous properties and adsorption analysis of activated carbons were characterized using BET and HPVAII. BET surface area of activated carbons decreased with an increase in NaOH loading. It seemed that impregnation with appropriate NaOH loading could develop some micropores of activated carbon. However, the excess of impregnant molecules may cause pore blockage leading to a decrease in total pore volume. The highest microporous volume was found after impregnating activated carbon with 1 weight% NaOH solution. The results of CO_2 adsorption at 0°C under atmospheric pressure up to saturated pressure revealed the maximum adsorption capacity, which used activated carbon was prepared by activation combined with oxidation method with 180 min of total activation time, two cycles for oxidation with 720 min and 1 weight% NaOH loading. The Grand Canonical Monte Carlo (GCMC) simulation was performed to determine pore size distribution of each prepared activated carbon. The results show that the micropore volume of microporous activated carbon dramatically decreased with an increase in NaOH loading while the micropore volume of mesoporous decreased slightly. The mesopore volume occurred when impregnated with 1 to 4 weight% NaOH loading.

3.2 Introduction

CO_2 is one of greenhouse gases mostly released from fossil-fuel power plants burning coal, natural gas, and heavy oil. The report of annual CO_2 emission has shown that the burning of fossil fuels for energy and cement production are responsible for a rapid increase of CO_2 level in the atmosphere since 1950 (Roser, 2020). The adverse effect of CO_2 accumulation on global warming has prompted the scientists and engineers to find various effective techniques for CO_2 capture and utilization. Currently, there are four technologies for the post-combustion capture of CO_2, including absorption, adsorption, cryogenic, and membrane separations. Among these processes, the adsorption process is an attractive technology because it possesses many favorable features as compared to other different capture methods, including process simplicity, low preparation cost of adsorbents, low energy consumption, and extremely high efficiency (Samanta et al., 2012).

Activated carbon is the most widely used adsorbent due to its high internal surface area with high degree of porosity, and microporous structure leading to high adsorption capacity. Typically, activated carbon can be prepared by the two-step physical or chemical activations with activating agents. Many biomaterials were employed as precusors for activated carbon preparation such as coconut shell (Chen et al., 2016; Tan et al., 2014), walnut shell (Rouzitalab et al., 2018), eucalyptus (Tangsathitkulchai, Ngernyen, & Tangsathitkulchai, 2009), argan fruit shell (Boujibar et al., 2018), corn stack (Song et al., 2015), longan fruit seed (Junpirom et al., 2005), etc. For the gas adsorption including CO_2 capture, the-adsorption capacity depends strongly on the microporous properties of activated carbons. To increase the CO_2 adsorption capacity, many researchers have investigated the preparation of activated carbon with high capture efficiency. Due to the acid gas characteristic of CO_2, the presence of more active basic sites on activated carbon should improve the adsorption efficiency in terms of both capacity and selectivity. The simple and direct technique to introduce more basic sites onto the adsorbent surfaces is by impregnating an adsorbent with basic or alkali solutions such as sodium hydroxide (Tan et al., 2014; Khalil et al., 2012; Naksusuk & Tangsathitkulchai, 2019), potassium hydroxide, metal oxide, amine solutions

(Gholidoust et al., 2017; Hidayu & Muda, 2016; Kongnoo et al., 2016; Mohammad et al., 2019).

Therefore, the main purpose of the present study was to improve the efficiency of prepared activated carbon for CO_2 capture. However, the proportion of various pore sizes of activated carbon is also a deciding factor for accommodating the amount of alkali impregnant to prevent the early blockage of internal pores. Therefore, this work also investigated the impact of proportional amounts of micropores and mesopores in activated carbon on their adsorption performance. Moreover, this study proposed a model of finite-length slit pores, which incorporates the molecules of sodium hydroxide with different loadings to investigate the mechanism of CO_2 and N_2 adsorption in different pore widths. The measurement of CO_2 and N_2 adsorption isotherms of prepared activated carbon were performed at 0°C and -196.15°C, respectively, and were used to compute the pore size distribution (PSD) using the Grand Canonical Monte Carlo (GCMC) simulation method. The effects of PSD and alkali loading of the slit pore model on the adsorption behavior of CO_2 and N_2 were also studied.

Sections 3.2 and 3.3 discuss the experimental and simulation results, respectively and both of the results were compared in this section. Section 3.4 gives the methodology for optimizing the experimental and the kernels of GCMC simulated equilibrium isotherms for both CO_2 and N_2, leading to the determination of pore size distributions. Finally, Section 3.5 provides the conclusions. The outcome of this investigation will offer an alternative method for improving the CO_2 capture efficiency in activated carbon, as well as the underlying adsorption mechanisms involved.

3.3 Methods

3.3.1 Experimental Isotherms

3.3.1.1. Material Preparation and Adsorption Isotherm Measurements

Longan fruit seed was used as precursor for preparation of activated carbon. Microporous activated carbons were prepared by the two-step activation method using CO_2 as an activating agent. Microporous activated carbons were activated at 850°C for 120 and 180 min and the derived activated carbons were denoted

as A850-120-X A850-180-X, respectively, where A represents microporous carbon and X is NaOH loading in percent by weight of the impregnant solution. Mesoporous activated carbons were prepared by oxidation combined with activation method, called OTA method (Lawtae & Tangsathitkulchai, 2021) The mesoporous activated carbons were prepared by oxidizing the initial microporous activated carbon under air flow at 230°C for 720 min, followed by a high temperature heating in N_2 and re-activating at 850°C for another 60 min , and this first-cycle product was denoted as O230-120-X, and for the two-cycle oxidation the carbon sample was denoted as O200-180-X. The steps of preparation of activated carbon products are schematically shown in Figure 3.1. The NaOH impregnated activated carbon used in this study was prepared by soaking the carbon in a NaOH solution of the desired concentration (in weight% NaOH) for 120 min and dried in an electric oven at 110°C for 24 hours. The concentration of NaOH solution was varied in the range from 0-13 weight%, corresponding to the NaOH loading of 0-872 mg NaOH/g carbon.

For the isotherm measurement, the prepared activated carbons were first degassed at 300°C for 720 min. The micromeritics high-pressure volumetric analyzer (HPVAII, Micromeritics, Norcross, GA, USA) was used to perform CO_2 adsorption at 0°C over a pressure range up to the saturation pressure and their porous properties were analyzed by measuring N_2 adsorption/desorption at -196.15°C, using the Micromeritics 3-Flex Surface Characterization Analyzer (Micromeritics, Norcross, GA, USA). Surface morphology of the prepared activated carbons was ascertained by a scanning electron microscope (JEOL-SEM, model JSM-7800F)

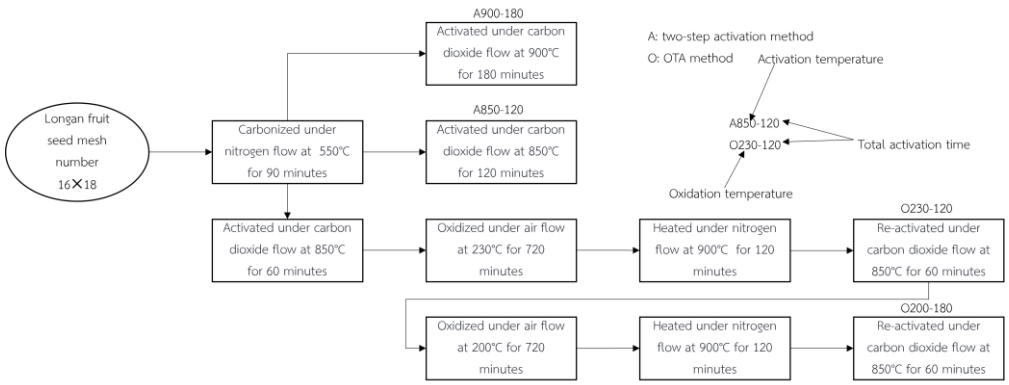

Figure 3.1 Steps of activated carbon preparation.

Four types of activated carbon were used in this work contain two microporous activated carbons which were prepared by two-step activation and two mesoporous activated carbons which were prepared by oxidation combined with activation method. The microporous activated carbons were denoted as A850-120-X and A850-180-X. The mesoporous activated carbons were denoted as O200-120-X and O200-180-X, X is percent NaOH by weight. The prepared activated carbons were analyzed to obtain CO_2 isotherms at pressure up to saturated pressure at 0°C using the high-pressure volumetric analyzer (HPVAII). Their porous properties such a BET surface area and pore volume were analyzed by using N_2 adsorption/desorption at -196.15°C, which performed on micromeritic 3-flex surface characteristic analyzer. Surface morphology of prepared activated carbons were obtained from the scanning electron microscope (JEOL-SEM model JSM-7800F).

3.3.2 The Kernel of Equilibrium Adsorption Isotherms

The GCMC simulation was used to compute the pore size distributions of prepared activated carbon and to investigate the effect of NaOH loading on adsorption performance. The model of carbon pore was given as a slit-shaped with finite length of 6 nm on both dimensions of X and Y with collision diameter (σ_{s-s}) of 0.34 nm and reduced well depth (ε_{s-s}/k_B) of 28.0 K. The micro-mesoporous adsorption behaviors were modeled with N_2 adsorption in pore size range of 0.5-5 nm (54 pore sizes) and CO_2 adsorption in pore size range of 0.4-4 nm (53 pore sizes). The N_2 molecules was modeled as a simple spherical molecule with a single Lennard-Jones (LJ) center. The Lennard-Jones parameters of N_2 follows collision diameter of 0.3615 nm and reduce well depth of 101.5 K. The molecular shape of carbon dioxide was employed as linear structure with 3-LJ centers (Harris & Yung, 1995). Its parameters employed in simulation follows: σ_{c-c}= 0.2757 nm, ε_{c-c}/k_B= 28.129 K, σ_{o-o} = 0.3033 nm, ε_{o-o}/k_B = 80.507 K, q^C=0.6512e and q^O = -0.3256e. Moreover, the molecules of NaOH were added on the surface of slit pore with five different loadings, its molecular parameters follow: σ_{o-o} = 0.3804 nm, ε_{o-o}/k_B = 1962 K, q^{Na} = 0.758e,q^O = -1.056e, and q^H = 0.298e (Santoro et al., 1984). The absence and presence of NaOH molecules on the solid model are shown in Figure 3.2 (a)-(b). The interaction energy between different fluid particles or between solid and fluid particles was calculated by the 12-6 LJ

potential model, with $\varepsilon_{s\text{-}f}$ and $\sigma_{s\text{-}f}$. These molecular parameters were calculated from the Lorentz-Berthlot rule shown in Equations (3.1) - (3.2). These simulations were performed in Microsoft visual studio 2010 software. The simulation box was specified by volume, chemical potential, and temperature to get the adsorption equilibrium information.

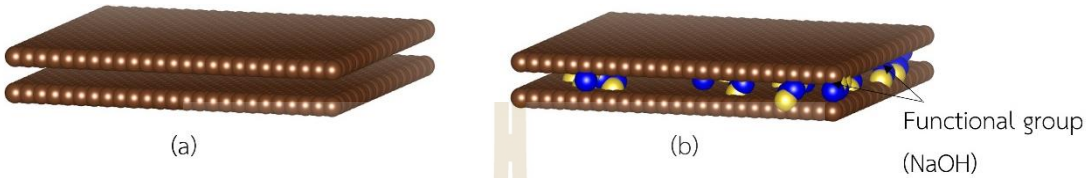

Figure 3.2 The slit pore model: (a) absence of NaOH molecules and (b) presence of NaOH molecules.

$$\varepsilon_{s-f} = \sqrt{\varepsilon_{s-s}\varepsilon_{f-f}} \tag{3.1}$$

$$\sigma_{s-f} = \frac{\sigma_{s-s} + \sigma_{f-f}}{2} \tag{3.2}$$

The model of carbons were given as a slit-shaped with the finite length of 6 nm on both dimensions. The kernel isotherms were performed by adsorption of CO_2 and N_2 at 0°C and -196.15°C of a slit pore carbon on the GCMC simulation. The slit pores were varied from 0.5 to 5 nm (54 pore sizes) for CO_2 adsorption and 0.4 to 4 nm (53 pore sizes) for N_2 adsorption. The collision diameter of carbon ($\sigma_{s\text{-}s}$) of 0.34 nm and the reduced well depth ($\varepsilon_{s\text{-}s}/k_B$) of 28.0 K.

3.3.3 Determining Pore Size Distribution

The sets of adsorption isotherms of N_2 and CO_2 were computed using the GCMC simulation and then applied to determine pore size distribution for different NaOH loadings in activated carbons. Adsorption isotherm of N_2 in slit pore was studied from pore width of 0.4-4 nm, while that of CO_2 was studied from pore width of 0.5-5 nm that cover the range of of micro-mesopores. The pore size distribution was calculated by comparing experimental isotherms and simulation results as the following Equation.

$$q^{exp}(P) = \int_{w^{min}}^{w^{max}} v(w)q^{sim}(w,P)dw \tag{3.3}$$

Where $q^{exp}(P)$ is experimental adsorbed amount at corresponding pressure, $q^{sim}(w,P)$ is simulation isotherm at corresponding pressure and pore width, v(w) is volume fraction of each pore width and w is pore width. To obtain a solution of PSD, Equation (3.3) was solved using a non-linear least square method by minimizing sum of squared error.

3.3.4 Calculation of CO_2 Absolute Isotherms

The amounts of CO_2 adsorbed in carbon obtained from HPVAII were calculated as an excess amount and plot as excess isotherms. The excess amount was calculated from the different volume of adsorbate dosed to the sample and total volume of adsorbate after dosing. The relation between the excess adsorption and the absolute absorption (Zhou & Zhou, 2001) follows Equation (3.4)

$$q' = q + v_a \rho_g \tag{3.4}$$

where q' is the absolute absorption that describes the number of adsorbed molecules in adsorbed phase, mol/g; q is the excess adsorption, mol/g; v_a is the volume of adsorbate in adsorbed phase. m^3/g; and ρ_g is the bulk gas density at T and P, mol/m^3.

The original isotherms were derived for absolute adsorption, which can be applied for excess adsorption as well, but they cannot represent the amount of excess isotherm if the amount adsorbed is high. The derived equation that is useful to represent the adsorption of ideal monocomponent adsorptive on a heterogeneous surface by applying Langmuir-Freundlich equation, is shown as Equation (3.5).

$$q = \left(\frac{bf^n}{1+b^n}\right)\left(q'_m - \frac{A^{3/2}}{(q'_m A_v)^{1/2}}\rho_g\right) \tag{3.5}$$

where f is fugacity which is transformed from pressure P and can be determined by an equation of state. b and n are parameters of the Langmuir-Freundlich equation. q'_m is a parameter of solid coverage surface. A_v is the Avogadro number. A is the specific surface area that corresponds to the energy well depth of adsorbent and adsorbate and surface coverage. The fugacity of CO_2 can be computed using the following equations;

$$\ln\frac{f}{P} = z - 4 - \ln\left(z - B^*\right) - \frac{A^*}{B^*}\ln\left(1 - \frac{B^*}{z}\right) \tag{3.6}$$

Where $$A^* = 0.4728\frac{\left(P/P_c\right)}{\left(T/T_c\right)^2} \tag{3.6.1}$$

$$B^* = 0.0867\frac{P/P_c}{T/T_c} \tag{3.6.2}$$

$$\alpha = (1 + m(1 - T_r^{0.5}))^2 \tag{3.6.3}$$

$$m = 0.480 + 1.574\omega - 0.176\omega^2 \tag{3.6.4}$$

$$z^3 - z^2 + z(A^* - B^* - B^{*2}) - A^*B^* = 0 \tag{3.6.5}$$

The parameters of CO_2 follow T_C = 304.2778 K; P_C=7.39807 MPa; ω= 0.225

3.4 Results and Discussion

3.4.1 Experimental Adsorption Results

3.4.1.1 N_2 adsorption/desorption isotherms at -196.15°C

The N_2 adsorption/ desorption isotherms of original activated carbon are shown in Figure 3.3. The adsorption isotherm of type I as classified by IUPAC classification can be used to describe the isotherm behavior of N_2 for samples A850-

120, A850-180 and O230-120, as typified by a sharp increase in nitrogen adsorption at low pressures and followed by plateau region at higher pressures. The type I isotherm mostly indicates the adsorption behavior of a microporous material with monolayer adsorption. The adsorption behavior changed from type I to type II when activated carbon was prepared with the OTA method as seen in Figure 3.3 for the O200-180 sample, and the isotherm exhibited a larger hysteresis loop corresponding to the characteristic of mesopores with the distribution of pore sizes. This tends to indicate that the OTA method was able to increase the amounts of mesopores. In the case of two step activation method, the isotherm for activation time of 120 min was greater than that of 180 min. It may be possible that some small pores of activated carbon may have been destroyed and coalesced into larger pores at longer activation time, thus leading to a decrease in surface area and total pore volume. It is further noted that increasing the number of oxidation cycle of the OTA preparation method can enhance substantially the adsorption capacity of nitrogen, as one can see that the isotherm of O200-180 > O230-120 > A850-120. This may indicate that the mesopores was possibly developed by micropore widening. Therefore, an increase of oxidation cycles and total activation time can effectively increase the adsorption capacity of N_2.

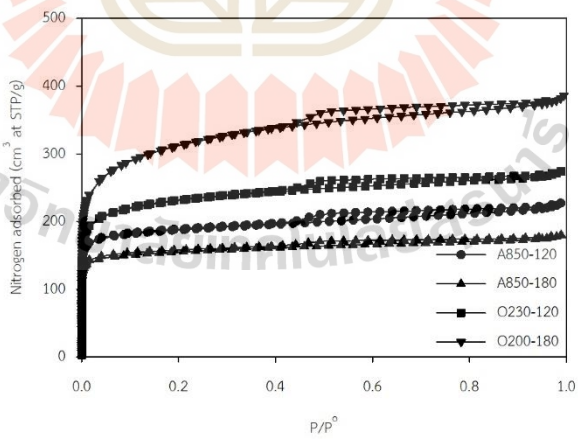

Figure 3.3 Nitrogen adsorption/desorption isotherms of original activated carbon.

Next, Figure 3.4 shows the N_2 isotherms of activated carbons impregnated with NaOH of concentrations varying from 1-13 weight%. In general, most adsorption isotherms exhibited Type I isotherm, while the isotherms of mesoporous

carbons showed the characteristic of TypeI at low pressures followed by Type II at higher pressures. There was a general tendency for the isotherm to show more characteristic of Type I isotherm as the NaOH loading increased, due principally to the increase in the number of micropores due to pore restriction effect. It is observed that the adsorption isotherm of 1% NaOH on activated carbon is much greater than that of the original activated carbon prepared by the two-step activation. This may be due to the stronger interaction between N_2 and NaOH and the interaction between the fluid and carbon surface, from which the NaOH effect shows a significant influence for smaller pores as one can see in the case of A850-180-1. However, the opposite behavior can be observed in the case of larger pores as indicated by the isotherms of O200-180 series. Therefore, the pore size of activated carbon is more important than the effect of functional groups for the mesopores. When the NaOH concentration is greater than 1 weight%, the adsorption isotherms decreased drastically with the increase of NaOH concentration greater than about 4% for the microporous carbons and greater than 7% for the mesoporous carbons. This could result from the blocking of NaOH molecules at the pore mouth, the effect of which is investigated in Section 3.3. This finding clearly indicates the capability of mesopores in accommodating more alkali molecules before the pore blocking comes into effect.

มหาวิทยาลัยเทคโนโลยีสุรนารี

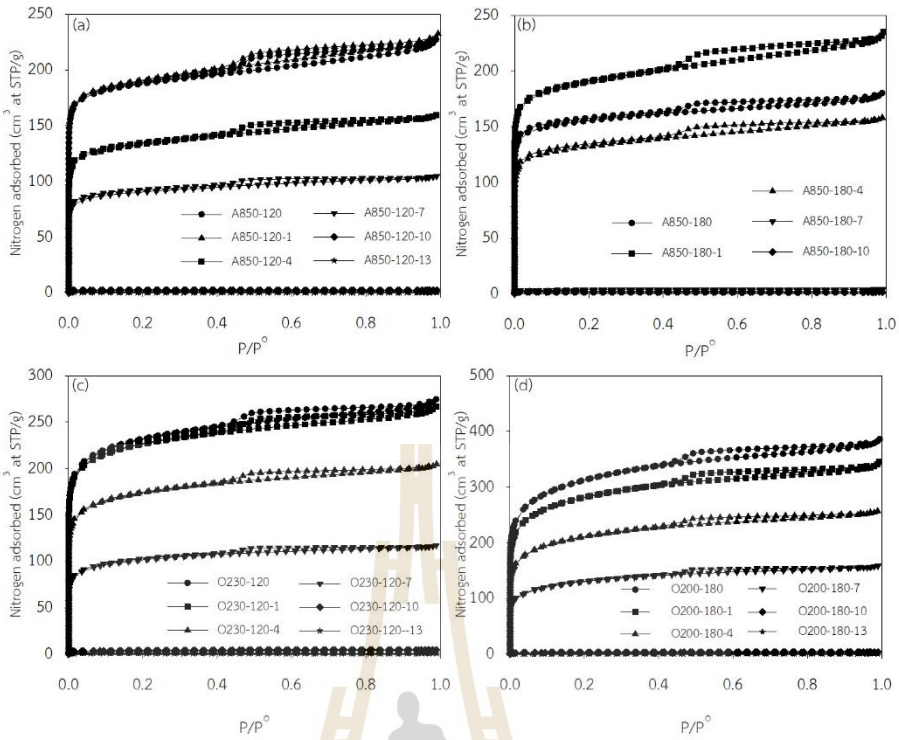

Figure 3.4 N_2 adsorption/desorption isotherms at -196.15°C of original and impregnated activated carbon prepared by total impregnation method of four different types of activated carbon consisting of (a) A850-120, (b) A850-180, (c) O230-120 and (d) O200-180.

3.4.1.2 CO_2 Adsorption at High Pressure

The adsorption of CO_2 at 0°C for activated carbon series (with and without NaOH impregnation) derived from the two-step activation and the OTA method, including samples A850-120, A850-180, O230-120 and O200-180 are shown in Figure 3.5 (a) to (d), respectively. The adsorption isotherms for the original carbon, 1% NaOH and 4% NaOH impregnated carbons are presented in circle, square and triangle symbols, respectively, in the same figure. The solid line represents the absolute adsorption while the dash line is the excess adsorptions isotherms, the absolute adsorption isotherm is always greater than that of the excess adsorption. The absolute adsorption isotherms increased with increasing pressures, by showing a dramatic increase at low relative pressures and then gradually increased at relative pressures greater than 0.2, while the excess isotherms exhibited the maximum adsorption and

then the isotherms fell continuously due to the increasing amount of adsorbate in the bulk phase Next, discussion on CO_2 adsorption performance of the prepared activated carbons will be based on the results of absolute adsorption isotherms.

Similar results can be observed for the adsorption isotherms of A850-120, O30-120 and O200-180 series in that the adsorption isotherms for carbons impregnated with 1% NaOH were greater than those of the original carbons. This is due to the stronger interaction between NaOH and CO_2 and the increasing of BET area as discussed in the case of N_2 adsorption. When the NaOH concentration increased to 4%, the isotherms were less than the isotherms obtained for carbons without NaOH. Again, it may be due to the difficulty of CO_2 molecules to diffuse through the pore mouth. However, in the case of A850-180 series, an increase of NaOH impregnation to 1 weight% cannot improve the adsorption amount of CO_2 in activated carbon. This may be attributed to the lower BET area and micropore volume as compared to those of the other carbons, thus rendering an early blocking of the pore mouth that retards the diffusion of CO_2. It is further noted that the activated carbons prepared by the OTA method showed the greater adsorption amounts than the activated carbons prepared by the two-step activation, simply because of their higher surface area and micropore volume.

It is found that the NaOH loading on activated carbon can increase the amount of CO_2 adsorbed, however, the optimum NaOH concentration must be properly selected. The sample O200-180-1 shows the greatest CO_2 absorption because this sample has the largest surface area, total pore volume, and micropore volume. As a result, the micropore volume plays a significant role in CO_2 adsorption in activated carbon. Moreover, the activated carbons prepared by the OTA method can increase larger pore widths, thus increase the diffusion rate of CO_2 into the inner pores to interact with the active sites of impregnated NaOH.

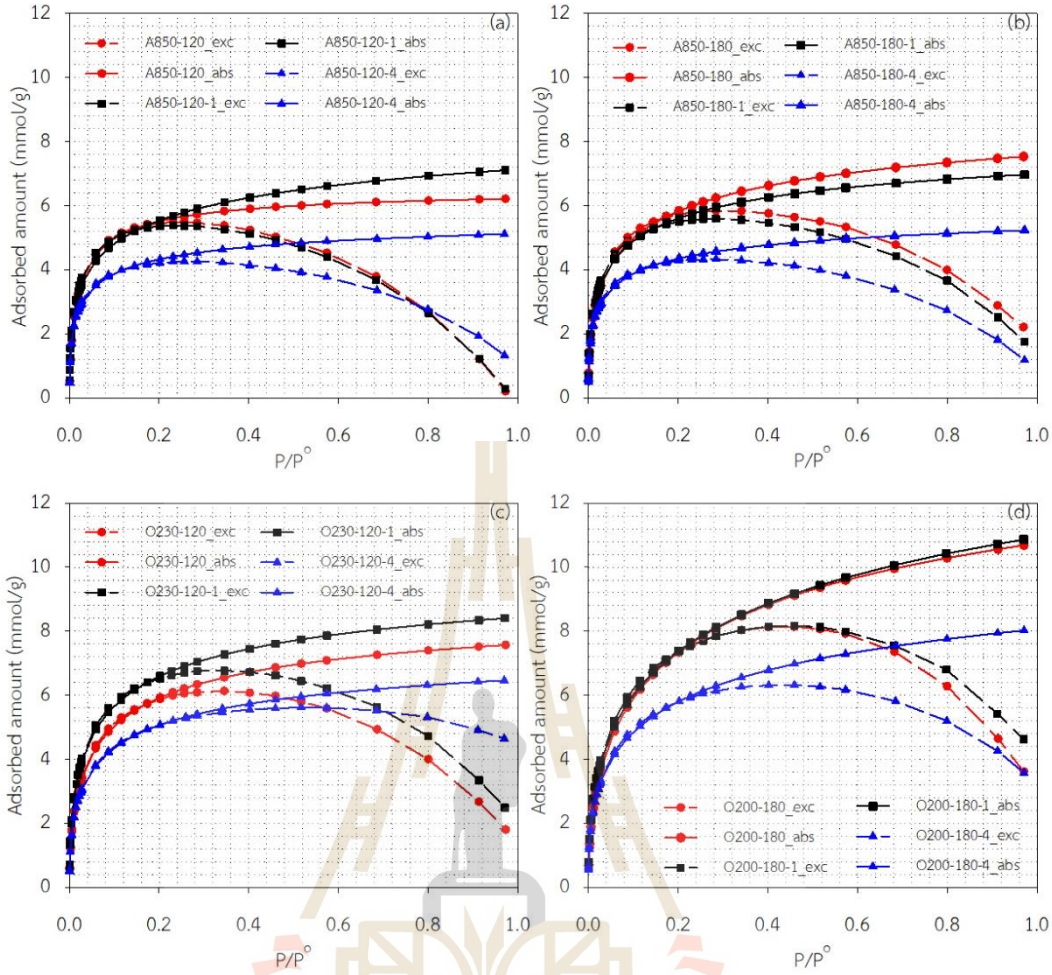

Figure 3.5 CO_2 adsorption isotherms at 0°C of original and impregnated activated carbon prepared by total impregnation method of four different types of activated carbon, including (a) A850-120, (b) A850-180, (c) O230-120 and (d) O200-180.

3.4.1.3 Porous Properties of Prepared Activated Carbons

Table 3.1 shows the porous properties of prepared activated carbons derived from nitrogen adsorption isotherms previously presented in Section 3.1. The porous properties such as BET surface area and total pore volume of the activated carbon prepared by the OTA method were greater than those of the activated carbon prepared by two-step activation method under the same activation conditions (samples O230-120 vs A850-120 and O200-180 vs A850-180). The sample of A850-180,

even being activated with longer activation time as compard with A850-120, had less surface area and micropore pore volume but greater mesopore volume than those of the A850-120 carbons. This could result from the merging of adjacent micropores into larger mesopores because of the high temperature and long activation conditions, thus leading to a decrease in the porous properties of A850-180 sample. It is interesting to note that when the original microporous carbon samples (A850-120 and A850-180) were impregnated with 1 weight% NaOH solution (equivalent to the NaOH loading of 67.1 mgNaOH/g carbon) the porous properties of A850-120-1 and A850-180-1 increased. One plausible reasoning might be that the presence of large NaOH molecules on the carbon surface increases the surface area for N_2 adsorption as compared to the area of the flat graphene sheet. However, the opposite results were observed with the case of mesoporous carbons except for the micropore volume that tended to increase, comparing samples O230-120 vs O230-120-1 and O200-180 vs O200-180-1. It is hypothesized that the pore mouth of some mesopores may be blocked by NaOH molecules so that the diffusion of N_2 molecules to the adsorption sites is reduced rendering the decrease of N_2 adsorption and the amount of micropores would increase also by the reduction of mesopore size by the pore-mouth blocking. At NaOH concentrations greater than 1 weight% NaOH, all porous properties for both the microporous and mesoporous carbons decreased continuously, obviously by the pore blocking effect at the pore mouth and the inner pores, and at 13 weight% NaOH almost all pores are completely blocked. As to the average pore size, it was found that the average pore size of microporous carbons appeared to decrease with the increase of NaOH impregnation but the average pore size of mesoporous carbon was not so sensitive to the change in the amount of NaOH impregnation. For all activated carbon samples, the average pore size varied in a narrow ramge of 1.7-2.3 nm, depending on the type of activated carbon, activation conditions and NaOH loading.

Table 3.1 Porous properties of prepared activated carbons using nitrogen adsorption/desorption at -196.15°C

Sample	S_{BET} (m^2/g)	V_{total} (cm^3/g)	V_{micro} (cm^3/g)	$V_{meso + macro}$ (cm^3/g)	$V_{meso + macro}/V_{total}$	Average pore diameter (nm)
A850-120	676	0.340	0.283	0.057	0.168	2.01
A850-120-1	684	0.347	0.285	0.062	0.178	2.03
A850-120-4	480	0.242	0.199	0.043	0.177	2.02
A850-120-7	330	0.159	0.137	0.022	0.138	1.93
A850-120-10	200	0.087	0.085	0.002	0.023	1.71
A850-120-13	23	0.011	0.010	0.001	0.091	1.96
A850-180	560	0.271	0.199	0.072	0.266	1.93
A850-180-1	686	0.350	0.284	0.066	0.188	2.04
A850-180-4	476	0.240	0.198	0.042	0.175	2.01
A850-180-7	295	0.144	0.122	0.022	0.153	1.95
A850-180-10	165	0.069	0.069	0.000	0.000	1.68
O230-120	839	0.413	0.256	0.077	0.186	1.97
O230-120-1	820	0.402	0.328	0.074	0.184	1.96
O230-120-4	629	0.310	0.250	0.060	0.194	1.97
O230-120-7	368	0.179	0.146	0.033	0.184	1.94
O230-120-10	283	0.161	0.123	0.038	0.236	2.27
O230-120-13	62	0.031	0.031	0.000	0.000	1.98
O200-180	1137	0.579	0.278	0.151	0.261	2.04
O200-180-1	1024	0.516	0.388	0.128	0.248	2.01
O200-180-4	766	0.389	0.288	0.101	0.259	2.03
O200-180-7	474	0.241	0.177	0.064	0.265	2.03
O200-180-10	245	0.140	0.102	0.038	0.271	2.29
O200-180-13	67	0.038	0.029	0.009	0.237	2.29

3.4.1.4 Surface Morphology of Prepared Activated Carbon

The surface morphology of activated carbons prepared by the two-step activation and the OTA method is shown in Figure 3.6 for conditions of without and with NaOH impregnation. Figure 3.6 (a)-(c) shows the conditions of 0, 1, and 4 % NaOH impregnation for the microporous carbons, while those of mesoporous carbons

prepared by the OTA method are presented in Figure 3.6 (d)-(f). As one can see from Figure 3.6 (a) and (d) for the original activated carbons, it was observed that pore size of activated carbon prepared by the OTA method had larger pore size than that prepared by the two-step activation. This indicates that the growth of mesopores is developed by micropores widening during the activation process (Lawtae et al., 2021). The surface morphology of activated carbons revealed a significant change in the case of NaOH impregnation, the pore size become smaller with the increase of NaOH concentration. Then the micropore volume increased as presented in Table 3.1, however when the NaOH loading exceeded 4 weight%, the micropore volume decreased. Figure 3.6 (b) and (e) show the particles of NaOH on the carbon surface and some allocated at the pore mounts, this leads to the increasing amounts of micropores and decreasing of mesopores. Most micropores can be observed for impregnation with 4% NaOH, as shown in the SEM images of Figure 3.6 (c) and (f) for A850-180-4 and O200-180-4, respectively. In Figure 3.6(b) for A850-180-1 carbon, not only the number of micropore increased but the mesopore number also appeared to increase, suggest that the deposit of NaOH particles on the carbon surfaces formed a biger pore. The SEM images shown in Figure 3.6 also support the porous properties presented in Table 3.1 in that the pore volume decreased with an increase of NaOH concentration since NaOH particles resided on the carbon surface and allocated at the pore mounts. From the porous properties together with the morphology study, we will use the activated carbons with 1 and 4% of NaOH impregnation to investigate CO_2 capture by simulation to investigate whether NaOH addition can enhance the adsorption capacity of CO_2 in activated carbon.

มหาวิทยาลัยเทคโนโลยีสุรนารี

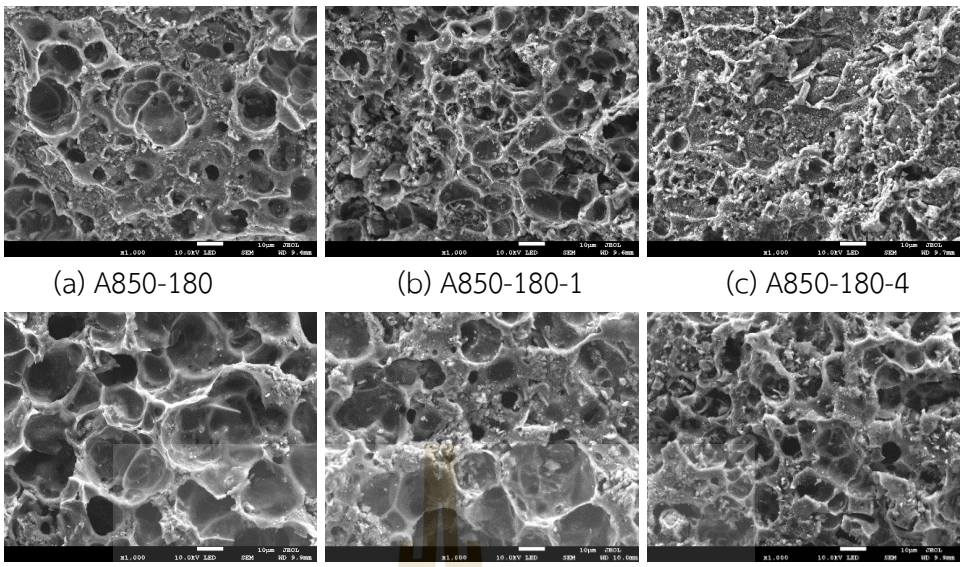

(a) A850-180 (b) A850-180-1 (c) A850-180-4

(d) O200-180 (e) O200-180-1 (f) O200-180-4

Figure 3.6 SEM images of original activated carbon and impregnated activated carbon with NaOH solutions.

3.4.2 Simulation Results

We start the discussion of Grand Canonical Monte Carlo (GCMC) simulation results by presenting the adsorption of N_2 at -196.15°C and CO_2 at 0°C with different pore widths in the presence and absence of NaOH as the kernel of isotherms for the calculation of pore size distribution (PSD). Then, the adsorption behavior of N_2 and CO_2 in different pore widths with NaOH loading are presented to show the effects of pore size and NaOH loading on adsorption isotherms. The location of NaOH on carbon surfaces is also investigated to see how the functional groups can affect the adsorption mechanism. Finally, the pore size distribution obtained from N_2 and CO_2 adsorption isotherms are then determined by the application of the GCMC simulation and experimental results.

3.4.2.1 The Kernel of Adsorption Isotherms of N_2

The adsorption isotherms of N_2 in finite-length carbon slit pore model with and without NaOH loading at 196.15°C for various pore widths are shown in Figure 3.7. This set of isotherms for different pore widths is known as kernel and used for determine the PSD. This kernel composes of 54 isotherms obtained for pore sizes ranging from 0.6 to 5 nm, which approximates the representation for mesopores with

diameter of 2.1 to 5 nm and micropores with diameter of 0.6 - 2 nm Each isotherm contains 47 adsorption points at pressures ranging from 1 Pa to the saturated pressure (relative pressure of 1.0). The adsorption of N_2 can be observed in pores having width of 0.65 nm for the slit pore model without and with NaOH concentration of less than 4%. For pore size of 0.6 nm, very small adsorbed amount occurs in the pore because the pore is too small for N_2 to penetrate to the inner pore. The maximum adsorption capacity is observed for pore having width of 0.65 nm in the absence of NaOH, this is due to the packing effect where the pore size is suitable for a single layer of particle to form. When pore width increases the adsorption capacity at saturated pressure decreases, because the distance between particle and slit walls is greater and this leads to the less interaction between fluid and solid. The adsorption behavior of N_2 in pore width less than 1.4 nm show the gradual increase in isotherm as the monolayer formation. When pore size is larger than 1.4 nm, the capillary condensation after the layering can be observed as the sudden jump of the isotherm. The capillary condensation pressure become greater when the pore width is larger.

In the case of pore containing NaOH, an early onset in adsorption isotherm can be observed, this is due to the greater interaction between fluid and functional group of NaOH. The capillary condensation pressures are shifted to lower pressures compared with those without functional group. However, the adsorption capacity at saturated pressure is less than that in the absence of NaOH because the pore volume of heterogeneous pore is decreased with the additional of NaOH particles. Therefore, the number of N_2 particles inside the pore then decrease. The maximum adsorption capacity for pore having NaOH is observed in the mesopores, as one can see that the maximum capacity of pore with 1, 4 and 7% NaOH are pore size of 3.4, 5.0 and 5.0 nm, respectively. Therefore, the NaOH amount and the pore width are possible key factors to enhance the adsorption of fluid in activated carbon.

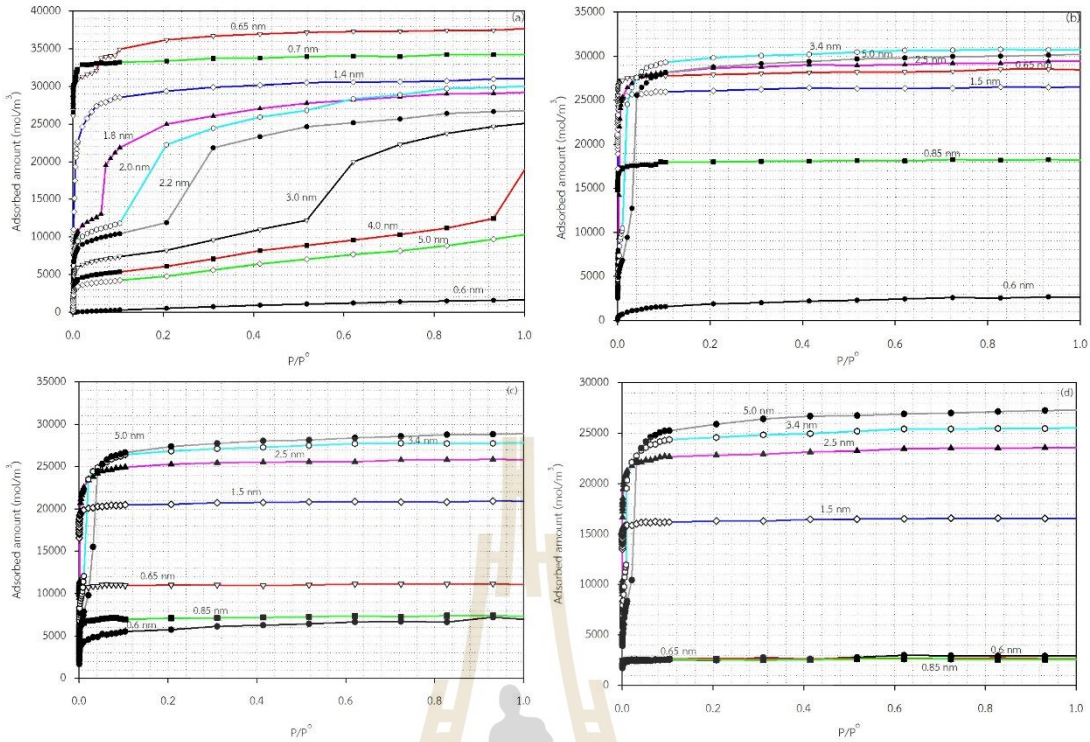

Figure 3.7 The kernels of GCMC simulated equilibrium adsorption isotherms of N_2 at -196.15°C in the model of carbon slit pores of 54 pore sizes; (a) original carbon slit pores and (b) carbon slit pores with 1% NaOH, (c) carbon slit pores with 4 weight% NaOH solution and (d) carbon slit pores with 7 weight% NaOH solution.

3.4.2.2 The Kernel of Adsorption Isotherms of CO_2

The kernels of CO_2 adsorption isotherms at 0°C are shown in Figures 3.8 (a)–(d). Each kernel is composed of 53 isotherms with pore widths ranging from 0.4 to 4 nm, which represent micropores and mesopores size range. Each isotherm is computed at a pressure of 10 Pa up to saturated pressure (relative pressure of 1.0). For carbon slit pores without NaOH or the original carbon presented in Figure 3.8 (a), the gradual increase of isotherm can be observed in the pore width of 0.6 to 1.2 nm, and when pores are larger than 1.2 nm, the pore filling can be seen. However, the sharp change in adsorption isotherm of CO_2 does not occur, as shown in the adsorption isotherm of N_2 in the previous section. This may be due to the higher adsorption temperature in the case of carbon dioxide. The pore size increases then the adsorbed

amount of CO_2 considerably decreases because the stronger fluid-solid interaction potential occurs in the smaller pore. The adsorbed amount increases significantly at low pressures, as indicated by the isotherm at 0.65 and 0.7 nm pore widths. The isotherms obtained for pore having NaOH loading of 1% NaOH as shown in Figure 3.8 (b) exhibit an early onset in the adsorption isotherm akin to that observed in the adsorption of N_2. Again, this is due to the stronger interaction between the functional group (NaOH) and the fluid particle which can enhance the initial adsorption at the functional group and then the adsorption of fluid particle and inner pore is occured. The adsorption capacity for pore sizes of 0.65 and 0.7 nm which can form only as a single layer are less than that for the original pore because the pore volume decreases. In the larger pore, the adsorption capacity is greater than that of the pore surfaces without NaOH due to an enhancement effect of NaOH.

When the NaOH loading increases, the initial adsorption at NaOH at low relative pressures also increases but the maximum adsorption capacity for the micropores decreases as can be observed in Figures 3.8 (c) and (d) for NaOH concentration of 4 and 7%, respectively. This is due to that NaOH are deposited at the pore mouth and may obstruct the diffusion of CO_2 to the inner pores. However, the opposite is true in the case of pores having width larger than 1.2 nm, but the adsorbed amounts decreased at all pore sizes. NaOH molecules in pores with a size of less than 0.7 nm may not be able to aid in the adsorption of CO_2. Small pore sizes may make it harder to disperse an adsorbate molecule or cause NaOH molecules to fill the pore to its maximum capacity. The results in the bigger pore size allows for a greater number of NaOH molecules to adsorb the CO_2 molecules, as seen in Figure 3.8 (c)-(d).

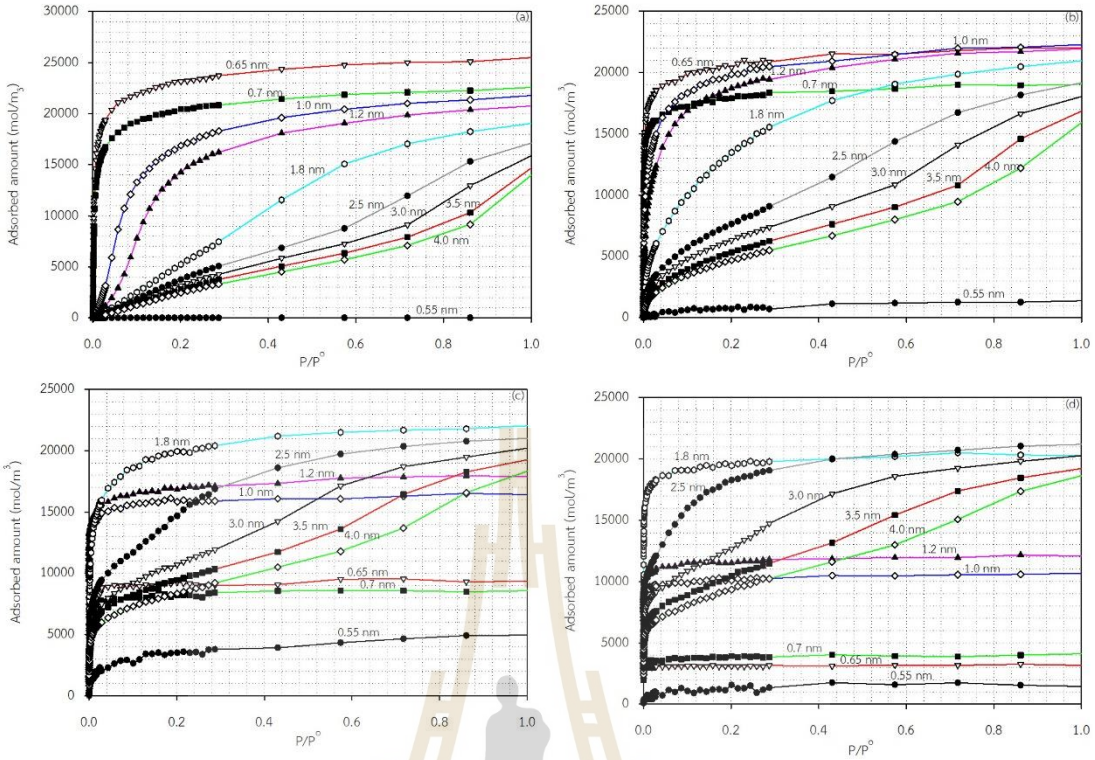

Figure 3.8 The kernels of GCMC simulated equilibrium adsorption isotherms of CO_2 at 0°C in model carbon slit pores of 53 pore sizes; (a) original carbon slit pores, (b) carbon slit pores with 1% NaOH, (c) carbon slit pores with 4% NaOH and (d) carbon slit pores with 7% NaOH.

3.4.3 Effects of Pore Width on CO_2 Adsorption

The effect of the pore width and various NaOH concentrations on the amount of CO_2 adsorption is shown in Figure 3.8 (a) to (d) at four different pressures: 0.1 kPa, 10 kPa, 100 kPa, and 3500 kPa. Figure 3.8(a) shows the results of CO_2 adsorption at 0.1 kPa (low pressure). The carbon slit pore with the presence of NaOH molecules provides a higher adsorption amount than the carbon slit pore without NaOH molecules. With an increase in NaOH concentration, a suitable pore width that gives the greatest CO_2 adsorption amount increases. At pressures of 0.1 kPa, 10 kPa, and 100 kPa, carbon slit pores without NaOH molecules show a lower adsorption amount than carbon slit pores with NaOH molecules. The strong interactions between carbon and CO_2 occur at a high pressure (3500 kPa). At 3500 kPa, the results show the maximum CO_2 adsorption of carbon slit pore without NaOH molecules, 1% NaOH, 4 %NaOH and

7% NaOH occuringr at pore widths of 0.65, 0.65, 1.75, and 2.4 nm, respectively. This indicates that a larger pore width can accommodate the molecule of NaOH better than the smaller pore width. If the percentage of NaOH is increased, the pore width of the carbon slit pore should accordingly increase to achieve higher adsorption.

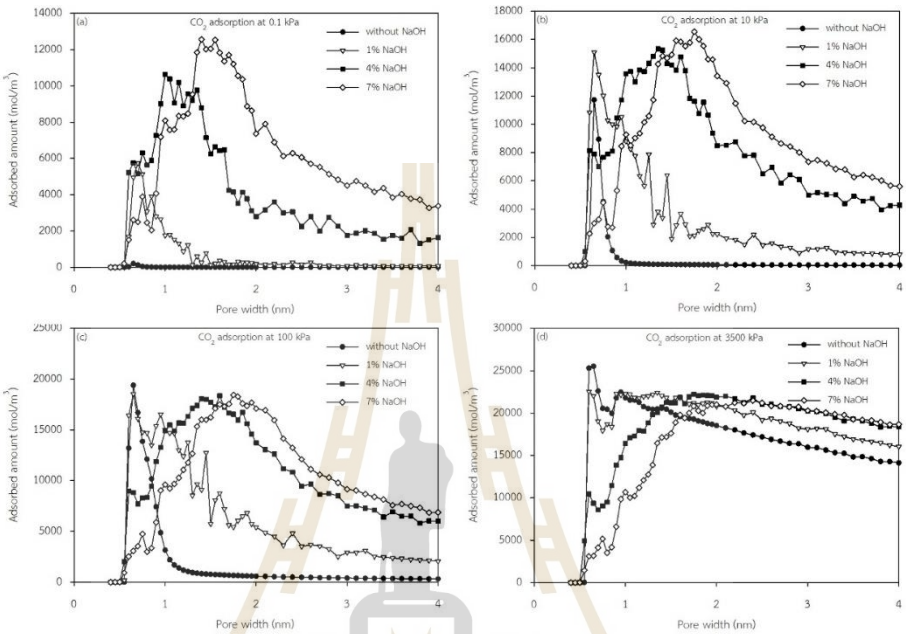

Figure 3.9 Effect of pore with on CO_2 adsorption amount with various %NaOH at pressure (a) 0.1 kPa, (b) 10 kPa, (c) 100 kPa and (d) 3500 kPa.

3.4.4 Effect of %NaOH on CO_2 Adsorption

Figure 3.10 (a) to (d) illustrates the effect of weight % NaOH solution and pore widths on the amount of CO_2 adsorbed at 0.1 kPa, 10 kPa, 100 kPa, and 3500 kPa, respectively. For pore widths of 1.7–2 nm and low pressure (0.1 kPa), % NaOH affects CO_2 adsorption. An increase in % NaOH causes an increase in the adsorbed amount for pore widths of 0.6, 0.65, and 1 nm, but when 7% NaOH is added to slit pores of 0.6 and 0.65 nm, the adsorption amount decreases, indicating an excess of NaOH loading into the slit pore. At the pressure of 10 kPa, the results tend to be the same as CO_2 adsorption at 0.1 kPa, but the adsorption amount increases with an increase in pressure. The CO_2 adsorption results at 100 kPa (Figure 3.10 (c)) show that the adsorption amount of 0.6-0.65 nm decreases with increasing NaOH. The adsorption

amount in the pore widths of 1.75-2 nm increases with the increase of % NaOH. While a slit pore with a pore width of 1 nm may accommodate the molecule of NaOH at 1% NaOH, one with a pore width of 1.75-2 nm can accommodate the molecule of NaOH up to 4% NaOH at a high pressure of 3,500 kPa. The results show that the amount of adsorption reduces with increasing NaOH concentration and pore width of 0.6-0.65 nm. The maximum adsorption of slit pores with 1% NaOH occurs when 1 nm of slit pores are utilized, suggesting that the activated carbon's pore size for the experiment on CO_2 adsorption is in the 1 nm range.

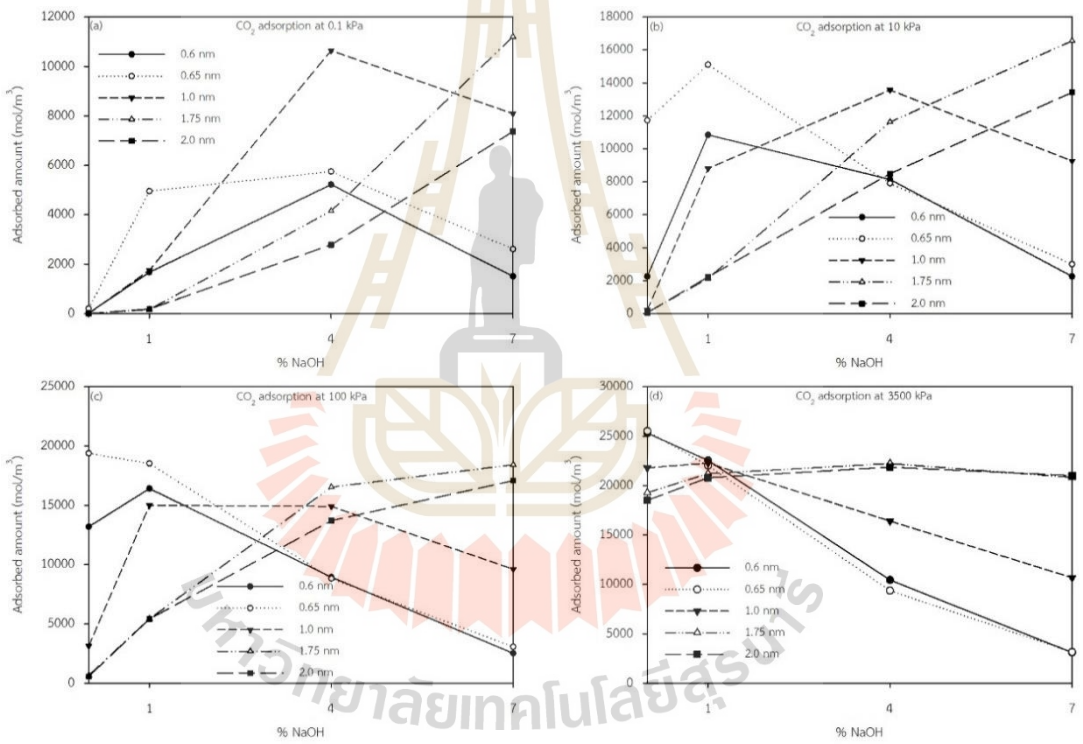

Figure 3.10 Effect of %NaOH on CO_2 adsorption amount with various pore width at pressure (a) 0.1 kPa, (b) 10 kPa, (c) 100 kPa and (d) 3500 kPa.

3.4.5 Effects of Functional Group Allocation on CO_2 Adsorption

Figures 3.11 and 3.12 show the effect of functional group allocation on CO_2 adsorption isotherms for the carbon slit pore model of 0.65 and 1.5 nm, respectively. The 1% NaOH with random topology adsorbed amount is the largest at

pressures less than 50 kPa, followed by the 1% NaOH fixed topology and without NaOH, according to the results of a pore width of 0.65 nm. The results indicate that the CO_2 molecules initially adsorbed on NaOH molecules which leads to a decrease in pore width, and subsequently the CO_2 molecules interacted with the carbon slit pores to fill them. At pressures greater than 100 kPa, the results of adsorption with 1% NaOH in random topology show the lowest adsorbed amount due to the difficulty of CO_2 to get access into the pore by diffusion, which results in pore blockage with NaOH. The highest adsorbed amount is derived with a slit pore without NaOH.

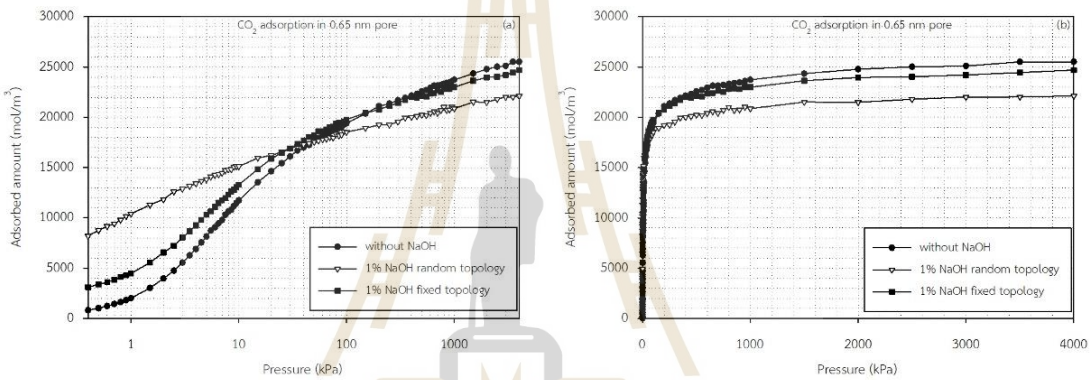

Figure 3.11 Effects of functional group allocation on CO_2 adsorption isotherms at 0°C for the carbon slit pore model of 0.65 nm width at (a) plotted in semi-log scale and (b) plotted in linear scale.

The results of Figure 3.12 can be described as follows: the highest adsorption of a pore size of 1.5 nm at low pressure occurs in a slit pore with a fixed topology of 1% NaOH because the molecules of CO_2 can interact rapidly with the molecules of NaOH. When the pressure was greater than 50 kPa, the 1% NaOH structure provides the maximum amount of adsorption, while a slit pore without a NaOH molecule yields the lowest amount of adsorption. The results demonstrate that in the larger pore size the NaOH molecules could exert a stronger CO_2 adsorption than the interaction between carbon and CO_2 molecules.

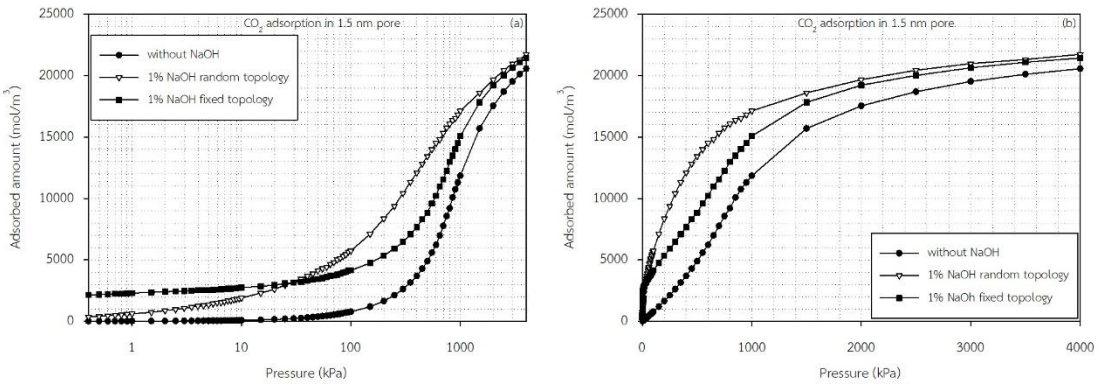

Figure 3.12 Effects of functional group allocation on CO_2 adsorption isotherms at 0°C for the carbon slit pore model of 1.5 nm width at (a) plotted in semi-log scale and (b) plotted in linear scale.

Figure 3.13 Snapshots of CO_2 molecules in carbon slit pore model of 0.65 nm. CO_2 adsorption at 0°C and 1% of NaOH functional groups with random topology. In these figures, the large brown spheres represent the solid model of carbon, yellow and blue spheres represent the functional group, and black and red spheres represent atoms of C and O of CO_2 molecule, respectively.

Figure 3.14 Snapshots of CO_2 molecules in carbon slit pore model of 0.65 nm. CO_2 adsorption at 0°C and 1% of NaOH functional groups with fixed topology. In these figures, the large brown spheres represent the solid model of carbon, yellow and blue spheres represent the functional group, and black and red spheres represent atoms of C and O of CO_2 molecule, respectively.

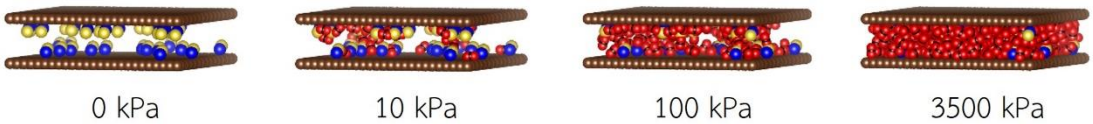

Figure 3.15 Snapshots of CO_2 molecules in carbon slit pore model of 1.5 nm. CO_2 adsorption at 0°C and 1% of NaOH functional groups with random topology. In these figures, the large brown spheres represent the solid model of carbon, yellow and blue spheres represent the functional group, and black and red spheres represent atoms of C and O of CO_2 molecule, respectively.

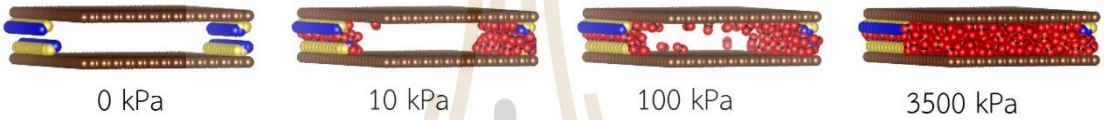

Figure 3.16 Snapshots of CO_2 molecules in carbon slit pore model of 1.5 nm. CO_2 adsorption at 0°C and 1% of NaOH functional groups with fixed topology. In these figures, the large brown spheres represent the solid model of carbon, yellow and blue spheres represent the functional group, and black and red spheres represent atoms of C and O of CO_2 molecule, respectively.

3.4.6 Pore Size Distributions

3.4.6.1 Pore Size Distribution Using N_2 Adsorption at -196.15°C

The density functional theory (DFT) was used to determine the pore size distribution of activated carbons, as shown in Figure 3.17 (a)-(d). The number of micropores of pore sizes less than 1.5 nm decreased with increasing NaOH loading after being impregnated. The results of samples A850-120 and A850-180 show a dramatically decreased in micropore volume at pore widths less than 1.0 nm. The micropore volume around 0.5 nm of A850-120-7 decreased by up to 30 percent from A850-120. For mesoporous activated carbon, O230–120 and O200–180, the micropore volume slightly decreases with the increase of NaOH loading. The mesopore volume of sample O200-180 is greater than that of samples A850-120, A850-180, and O230-

120. An increase in NaOH loading does not significantly decrease the mesopore volume (pore width greater than 2 nm). As a result of the strong interaction between carbon and N_2 molecules, the majority of the adsorption occurs in the micropore volume at a pore size of 0.55-0.65 nm.

มหาวิทยาลัยเทคโนโลยีสุรนารี

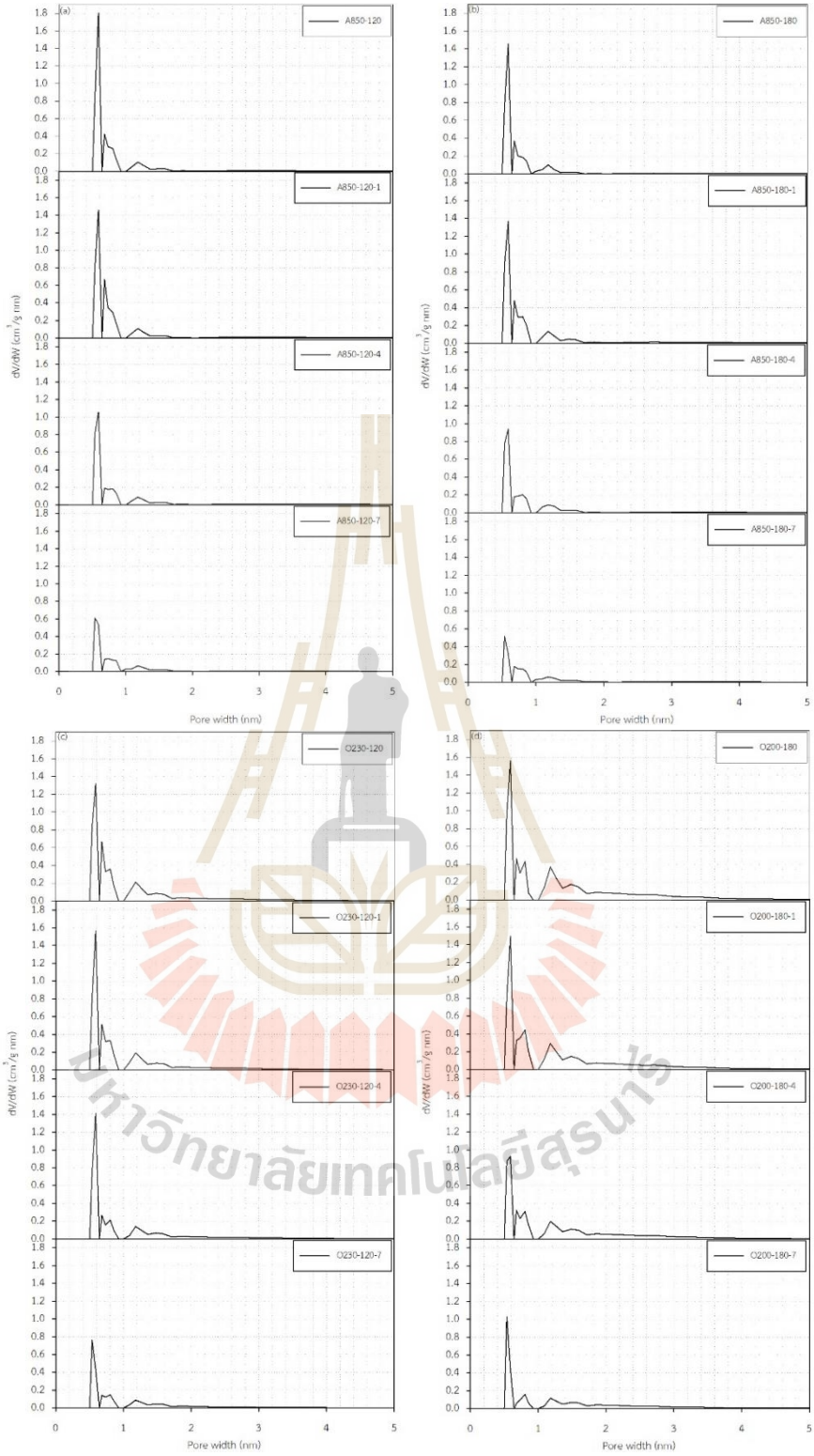

Figure 3.17 Effect of NaOH loading on pore size distribution computed by DFT using adsorption of N_2 at -196.15°C of four type activated carbons: (a) A850-120, (b) A850-180, (c) O230-120 and (d) O200-180.

3.4.6.2 Pore Size Distribution Using CO_2 Adsorption at -196.15°C

Figures 3.18 (a)-(d) show the pore size distribution of activated carbon using CO_2 adsorption at 0°C. The results show that most micropores are in the range of less than 1.5 nm for original or non-impregnated activated carbon. After being impregnated with 1% NaOH, the micropore volume of all types of activated carbon dramatically decreased. Both the A850-120 and A850-180 sample series exhibit the same pattern. A850-120 and A850-180 are adsorbed at pore diameters smaller than 1 nm. This illustrates the impact of the interaction between adsorbate molecules and narrow pores. After impregnating with 1% NaOH, the highest amount of CO_2 adsorption takes place in 1.4 nm pores, followed by mesopores. After impregnating with 4 and 7 % NaOH, the results of samples O230-120 and O200-180, and original activated carbon can be adsorbed at pore diameters less than 2 nm. Most adsorption takes place in pores smaller than 1 nm due to the strong interaction in the small pores. After being impregnated with NaOH, the micropores between 0.5 and 1 nm in size are not detected. Furthermore, after being impregnated with 4 and 7% NaOH, respectively, samples O230-120 and O200-180 develop mesopores in the range of 2-3 nm. After being impregnated with 4% NaOH, samples O230-120 and O200-180 possess mesopore volume in the range of 2-2.6 nm. Total pore volume and pore size distribution diminish substantially when the carbons are impregnated with 7% NaOH.

The micropore volume of activated carbon appears to have a significant role in CO_2 adsorption, according to the results of CO_2 adsorption in section 2.1.4 and the results of calculating pore size distribution. The maximum CO_2 adsorption capacity occurs in activated carbon that is impregnated with 1% NaOH solution. Additionally, the results indicate that activated carbon with a 4% NaOH impregnation has a greater mesopore volume with a more uniform distribution of mesopores, suggesting that some NaOH molecules may the larger pore. The micropore volume of activated carbon decreases as the number of NaOH molecules increases, and CO_2 is adsorbed in the larger pore size as a result of the interaction between NaOH and CO_2 molecules.

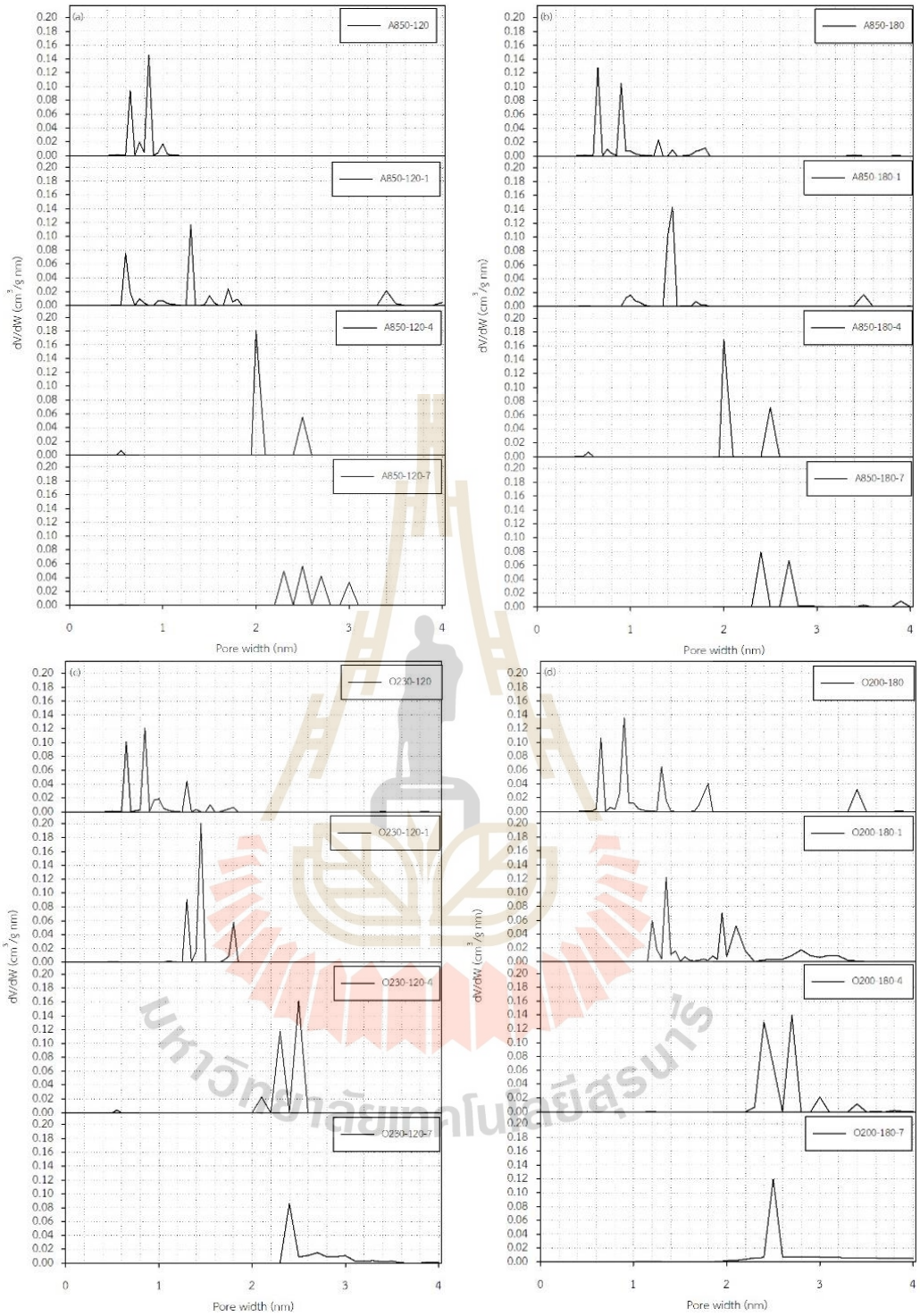

Figure 3.18 Effect of NaOH loading on pore size distribution computed by GCMC simulation using adsorption isotherms of CO_2 at 0°C for four type activated carbons: (a) A850-120, (b) A850-180, (c) O230-120 and (d) O200-180.

3.5 Conclusions

Four types of activated carbons were prepared in this work: A850-120, A850-180, O230-120, and O200-180. The results of the porosity of the prepared activated carbon after being impregnated with 0–7% NaOH illustrated a decrease in surface area and micropore volume. A decrease in the porous properties of impregnated activated carbon due to an increase in NaOH molecules, which entered into pores, and some molecules may have blocked a small pore mount of an activated carbon. The SEM results and average pore diameter showed that the activated carbon impregnated with 1% NaOH had larger pores than the original activated carbon. The highest CO_2 adsorption up to a saturated pressure at 0°C was found for the sample impregnated with 1% NaOH. The maximum adsorption capacity occurred with appropriate pore distribution and NaOH loading. Pore size distribution determined using the GCMC for four types of activated carbon were studied over the range of 0.6-4 nm pore widths. The results of impregnating samples O230-120 and O200-180 with 1 and 4% NaOH showed an increase in mesopores and a decrease in micropores. However, after being impregnated with 1% NaOH, the micropore of the microporous activated carbon A850-120 and A50-180 rapidly decreased. All of the results indicate that micropores play a significant role in the CO_2 adsorption, and mesopores may influence the diffusion of adsorbed molecules into pores. Future research may concentrate on the impact of pore size distribution in porous materials with an emphasis on the role of mesopores in accommodating alkali impregnants in activated carbon.

มหาวิทยาลัยเทคโนโลยีสุรนารี

3.6 References

Boujibar, O., Souikny, A., Ghamouss, F., Achak, O., Dahbi, M., & Chafik,. (2018). CO_2 capture using N-containing nanoporous activated carbon obtained from argan fruit shells. Journal of Environmental Chemical Engineering, 6(2), 1995-2002. doi:https://doi.org/10.1016/j.jece.2018.03.005

Chen, J., Yang, J., Hu, G., Hu, X., Li, Z., Shen, S., Fan, M. (2016). Enhanced CO_2 Capture Capacity of Nitrogen-Doped Biomass-Derived Porous Carbons. ACS Sustainable Chemistry & Engineering, 4(3), 1439-1445. doi:10.1021/acssuschemeng.5b01425

Gilbert J. Santoro (1984). Experimental and theoretical deposition rates from salt-seeded combustion gases of a Mach 0.3 burner rig [microform]

Gholidoust, A., Atkinson, J. D., & Hashisho, Z. (2017). Enhancing CO_2 Adsorption via Amine-Impregnated Activated Carbon from Oil Sands Coke. Energy & Fuels, 31(2), 1756-1763. doi:10.1021/acs.energyfuels.6b02800

Harris, J. G., & Yung, K. H. (1995). Carbon Dioxide's Liquid-Vapor Coexistence Curve And Critical Properties as Predicted by a Simple Molecular Model. The Journal of Physical Chemistry, 99(31), 12021-12024. doi:10.1021/j100031a034

Hidayu, A. R., & Muda, N. (2016). Preparation and Characterization of Impregnated Activated Carbon from Palm Kernel Shell and Coconut Shell for CO_2 Capture. Procedia Engineering, 148, 106-113. doi:https://doi.org/10.1016 /j.proeng.2016. 06.463

Junpirom, S., Do, D. D., Tangsathitkulchai, C., & Tangsathitkulchai, M. (2005). A carbon activation model with application to longan seed char gasification. Carbon, 43, 1936-1943.

Khalil, S. H., Aroua, M. K., & Daud, W. M. A. W. (2012). Study on the improvement of the capacity of amine-impregnated commercial activated carbon beds for CO_2 adsorbing. Chemical Engineering Journal, 183, 15-20. doi:https://doi.org/10. 1016/j.cej.2011.12.011

Kongnoo, A., Intharapat, P., Worathanakul, P., & Phalakornkule, C. (2016). Diethanolamine impregnated palm shell activated carbon for CO_2 adsorption at elevated temperatures. Journal of Environmental Chemical Engineering, 4(1), 73-81. doi:https://doi.org/10.1016/j.jece.2015.11.015

Lawtae, P and C. Tangsathitkulchai (2021). A new approach for controlling mesoporosity in activated carbon by consecutive process of air oxidation, therma destruction of surface functional groups, and carbon activation (the OTA method). Molecules, 26(9)

Lawtae, P. Phothong K. Wongkoblap, A. and Tangsathitkulchai, C. (2021). Pore sixe distribution of micro-mesoporous activated carbons determined from isotherms of gas adsorption on homogenious surfaces: experiment and computer simulations. Molecules, 26

Mohammad, N. K., Ghaemi, A., & Tahvildari, K. (2019). Hydroxide modified activated alumina as an adsorbent for CO_2 adsorption: Experimental and modeling. International Journal of Greenhouse Gas Control, 88, 24-37. doi:https://doi.org/10.1016/j.ijggc.2019.05.029

Naksusuk, S., & Tangsathitkulchai, C. (2019). Carbon Dioxide Capture in a Fixed Bed of Coconut wShell Activated Carbon Impregnated With Sodium Hydroxide: Effects of Carbon Pore Texture and Alkali Loading. Engineering Journal, 23(4), 29-48. doi:10.4186/ej.2019.23.4.29

Roser, H. R. a. M. (2020). CO_2 and Greenhouse Gas Emissions. Our World in Data. Retrieved from https://ourworldindata.org/co2-and-other-greenhouse-gas-emissions

Rouzitalab, Z., Mohammady Maklavany, D., Rashidi, A., & Jafarinejad, S. (2018). Synthesis of N-doped nanoporous carbon from walnut shell for enhancing CO_2 adsorption capacity and separation. Journal of Environmental Chemical Engineering, 6(5), 6653-6663. doi:https://doi.org/10.1016/j.jece.2018.10.035

Samanta, A., Zhao, A., Shimizu, G. K. H., Sarkar, P., & Gupta, R. (2012). Post-Combustion CO_2 Capture Using Solid Sorbents: A Review. Industrial & Engineering Chemistry Research, 51(4), 1438-1463. doi:10.1021/ie200686q

Song, T., Liao, J.-m., Xiao, J., & Shen, L.-h. (2015). Effect of micropore and mesopore structure on CO_2 adsorption by activated carbons from biomass. New Carbon Materials, 30(2), 156-166. doi:https://doi.org/10.1016/S1872-5805(15)60181-0

Tan, Y. L., Islam, M. A., Asif, M., & Hameed, B. H. (2014). Adsorption of carbon dioxide by sodium hydroxide-modified granular coconut shell activated carbon in a fixed bed. Energy, 77, 926-931. doi:https://doi.org/10.1016/j.energy.2014.09.079

Tangsathitkulchai, C., Ngernyen, Y., & Tangsathitkulchai, M. (2009). Surface modification and adsorption of eucalyptus wood-based activated carbons: Effects of oxidation treatment, carbon porous structure and activation method. Korean J. Chem. Eng., 26(5), 1341-1352. doi:https://doi.org/10.1007/s11814-009-0197-4

Zhou, L., & Zhou, Y. P. (2001). A mathematical method for determination of absolute adsorption from experimental isotherms of supercritical gases. Chinese Journal of Chemical Engineering, 9(1), 110-115. Retrieved from https://www. cheric.org /research/tech/periodicals/view.php?seq=282275

CHAPTER IV

PROCESS CONFIGURATION STUDIES OF METHANOL PRODUCTION VIA CARBON DIOXIDE HYDROGENATION: PROCESS SIMULATION-BASED OPTIMIZATION USING ARTIFICIAL NEURAL NETWORKS

4.1 Abstract

Carbon dioxide (CO_2) emission is the main cause of global warming. Carbon dioxide utilization is an interesting process to reduce the quantity of CO_2 in the atmosphere. Methanol production is a chemical that can be produced from CO_2 through carbon dioxide hydrogenation, which is considered a green chemical process. Recently, the configuration and operating condition of this process have been studied to obtain the minimum methanol production cost. This chapter presents a study of the process configuration of methanol production via carbon dioxide hydrogenation. The minimum methanol production cost of three configurations was optimized. Price sensitivity was studied as well to describe the impacts of raw materials on methanol production cost. The result shows hydrogen price has a large impact on methanol production cost. In the optimization model, four different numbers of nodes in a hidden layer of artificial neural networks were studied. Subsequently, the configuration of the artificial neural network that yielded the minimum error between actual and predicted methanol production costs was selected as the most suitable configuration. Eight nodes with feed-forward neural networks were selected to use for training the data. The optimization results of three different configurations of methanol production process show the lowest methanol production cost was obtained by operating with two reactors in series, which cost $885.85 per ton of methanol.

4.2 Introduction

Many greenhouse gases (GHGs) are naturally present in the atmosphere, carbon dioxide is one of the most emission by anthropogenic, which causes global warming. Nowadays, carbon dioxide present 76% of the total sources of greenhouse gas (Mukherjee, Okolie et al., 2019). An increase in the amount of carbon dioxide in the air leads to the challenge of carbon dioxide capture and utilization. Carbon dioxide could be used as a reactant to produce sustainable energy, like methanol and dimethyl ether (Arena, Mezzatesta et al., 2014). The methanol synthesis is considered as the second largest production from carbon dioxide conversion, after the urea production(Naims, 2016). Methanol is a very valuable chemical, giving products such as dimethyl ether, methyl tertiary-butyl ether, formaldehyde, acetic acid, and its direct use as fuel (Bowker, 2019).

Methanol or methyl alcohol is an environmentally friendly fuel due to its combustion does not produce toxic byproducts like SO_x or NO_x (Zander, Kunkes et al., 2013). The advantages of using methanol as a fuel are it has lower risks, lower emissions, and higher performance than gasoline (Bill, 1998). The methanol production scale was reported in market analytics: methanol and derivatives-2018 (Nexant, 2018) that the world scale has been constantly increasing. From all of methanol demands 28% of the demand is used in the methanol to olefin (MTO) industry and 23% of the demand is used in the formaldehyde production process.

Conventionally, methanol was produced by syngas. The first commercial methanol synthesis plant was established in 1923 by BASF with operating conditions of 300 bar and temperature above 300°C. Due to the high pressure and temperature of methanol synthesis, a copper-based catalyst was introduced to reduce that limitation. The Cu-ZnO/Al_2O_3 catalyst was performed in the reaction of methanol synthesis with operating conditions of 50-100 bar and 200-300°C. The improvement of catalysts to higher performances and methanol yield were studied (Liang, Dong et al. 2009; Liu, Guo et al. 2016; Jadhav, Vaidya et al., 2014). For example, an increase in methanol production rate by doping Mn to Cu/ZnZr catalyst or coding Pd/ZnO over multi-walled carbon nanotubes (Liang, Dong et al., 2009). Furthermore, methanol could be

manufactured using carbon dioxide and hydrogen, called carbon dioxide hydrogenation.

In the recent decade, the methanol production from pure carbon dioxide and hydrogen (carbon dioxide hydrogenation) feeds were proposed as a green chemical process that support the carbon dioxide mitigation. However, this process requires higher cost and energy consumption than methanol production from syngas. Bowker, M. (B.Vaferi, M.Bahmani et al., 2014) suggested that sustainable methanol synthesis should be produced not only from green source of carbon but also hydrogen must not be derived from fossil fuels. Tidona, B., et al. (Tidona, Koppold et al., 2013) reported that energy consumption of the conversion of carbon dioxide and hydrogen is 26% higher than syngas-to-methanol production. Other researches also reported that the carbon dioxide hydrogenation required 2 to 2.5 times higher cost than conventional process and consumed more utilities (F.R.Machado, Medeiros et al. 2014; Atsonios, Panopoulos et al., 2016).

Several process modification and optimization were studied to reduce cost and energy consumption of carbon dioxide hydrogenation process, and to achieve mitigation of carbon dioxide emission to the atmosphere (F.R.Machado, Medeiros et al., 2014; Pellegrini, Soave et al., 2011; Roh, Nguyen et al., 2015; Leonzio, 2017; Matr, 2018). Pellegrini et al., (Pellegrini, Soave et al., 2011 modified the methanol production plant configuration, the gases recycled was used to feed a combined-cycle energy plant. The two stages reforming and carbon dioxide hydrogenation for the sustainable carbon dioxide conversion process were compared to conventional methanol production plant. The development of these process could reduce the net carbon dioxide emission especially in the case of carbon dioxide hydrogenation. The cost of direct conversion via carbon dioxide hydrogenation is considered high due to large amount of hydrogen consumption and high hydrogen price (Roh, Nguyen et al. 2015).

For studied of operating conditions of the reactor for methanol production via carbon dioxide hydrogenation, the temperature range of 200-500°C (Ullmann, 2003; Leonzio, Zondervan et al., 2019) and the pressure range of 15-55 bar were studied (Leonzio, Zondervan et al., 2019). Leonzio et al. reported that high operating pressure and low operating temperature can increase carbon dioxide conversion (Leonzio,

Zondervan et al., 2019). The operating conditions of reactor 210°C and 78 bar resulted in 94% carbon dioxide conversion (Pérez-Fortes, Schöneberger et al. 2016).

Many researches on process modeling and optimization of methanol production via CO_2 hydrogenation were studied to increase methanol production capacity. Leonzio, G. (Leonzio, 2017) used the ANOVA to perform the methanol reactor model using central composite design to investigate a significant of each parameter on the reactor performance. If a temperature is increased, carbon dioxide/hydrogen feed ratio is decreased and recycle ratio is increased could be obtained the higher methanol productivity. After that, the methanol production was studied with different three novel reactor configurations, once-through reactor, equilibrium reactor with recycle, and membrane reactor with separator, using Aspen Plus. For the reactor with recycle showed the higher methanol product occurs when increased of the recycle ratio and ensures higher efficiency when compared with other reactor schemes (Leonzio, Zondervan et al., 2019). The study of process modeling and simulation of (Matr, 2018) was performed with different model configurations. The results indicated that methanol production with two reactors in series have an advantage of low production cost at the maximum capacity. The optimization of temperature before entering the first reactor of 160°C with the recycle ratio of 1.197 could help in minimization of heat integration and production cost. Borisut, P. and A. Nuchitprasittichai (Borisut and Nuchitprasittichai, 2019) performed simulation – based optimization to minimize the cost of methanol production via CO_2 hydrogenation. The response surface methodology (RSM) was used to represent methanol production and optimized the methanol production cost.

For simulation-based optimization, an optimization algorithm uses mathematical functions as the objective functions, and solve the problems via minimization or maximization of a function. The mathematical functions can be nonlinear regression models, or metamodels such as Artificial Neural Networks (ANNs). An artificial neural network is one of surrogate modeling, which powerful tool for many applications and can fit complex nonlinear functions (Jin, Li et al. 2016). Artificial neural network is widely used in many processes in the chemical engineering field to model functions i.e. carbon dioxide absorption, and ethylene cracking furnaces (Jin, Li et al., 2016; Eason and Cremaschi, 2014; Sudakov, Koroteev et al., 2019; Ye, 2019). In the case of methanol production, artificial neural network was used to model and optimize the

process. The modification and optimization of carbon dioxide hydrogenation unit to maximize the amount of produced methanol was investigated using artificial neural network and verified with industrial plant data (B.Vaferi, M.Bahmani et al., 2014). The inputs of the model are the inlet pressure and inlet temperature of the reactor. The multilayer perceptron (MLP) network is determined to select the number of nodes by trial and error. The results indicated that higher methanol production was produced with an increase in the reactor inlet pressure and decreasing in reactor inlet temperature. Ye, J. (Ye, 2019) used artificial neural network with three layers to investigate the influences of decision parameters on methanol concentration and carbon monoxide conversion. The results showed that a simple artificial neural network is fairly consistence with experimental results and the data of an outputs indicated that methanol concentration and carbon monoxide conversion were increased with an increase in pressure from 10 to 30 bar.

However, modeling and optimization of the methanol production process via carbon dioxide hydrogenation, which compares process configurations and optimizes process parameters for the minimum production cost has not been studied. This work studied methanol production process with three different configurations and applied artificial neural network as an objective function in the optimization problem. For artificial neural network training, the difference in the number of nodes was considered. The model representation with artificial neural network was solved to obtain the minimum methanol production cost in a unit per ton of produced methanol and optimal operating conditions. The optimization problem was solved using an optim optimizer.

Section 4.2 gives details of process configuration and economic evaluation. Section 4.3 cover sampling techniques, artificial neural network, and optimization formulation. Section 4.4 discusses the suitable configuration and presents results of optimization. Section 4.5 gives the conclusion.

4.3 Process Simulation and Economic Evaluation

In this section, three different configurations of methanol production process, which are configuration I: once-through reactor methanol production, configuration II:

methanol production with a recycle, and configuration III: two reactors in series, were compared in term of their methanol production costs.

4.3.1 Process Simulation

Methanol Production via carbon dioxide hydrogenation process was simulated using ASPEN HYSYS V10.1 process simulator with Peng-Robinson fluid package. Feeds of 1,000 kmoles per hour of carbon dioxide at 40°C, and 3,000 kmoles per hour of hydrogen at 25°C were mixed at a pressure of 20 bar. After that, the feed stream was compressed to a design reaction pressure and heated to the design reaction temperature. The methanol production process comprised two sections. The first section involves methanol production where methanol was produced from reactants in an equilibrium reactor. The second section involves methanol purification. In the methanol purification process, liquid methanol product was sent to the first distillation column to separate light components (carbon dioxide, carbon monoxide, and hydrogen) from a mixture of methanol and water. The bottom stream of the first distillation, which contains only methanol and water, was then sent to the second distillation column to separate water from the methanol product. The purity of the methanol product is 99.5% by mole.

For the study of three different process configurations, the compositions, conditions, and flow rate of hydrogen and carbon dioxide feeds were the same for all configurations. The following sections describe the details of each process configuration.

4.3.1.1 Configuration I: Once-Through Reactor Methanol Production

The reactants (hydrogen and carbon dioxide) were fed into an equilibrium reactor at design conditions to produce methanol with reactions as shown in Equations (4.1) to (4.3) (Tidona, Koppold et al., 2013). After product stream left an equilibrium reactor, the steam temperature was decreased. The product stream was sent to the purification process. The process simulation of this configuration was shown in Figure 4.1(a).

$$CO_2 + H_2 \leftrightarrow CO + H_2O \qquad \Delta H300K = 41.2 \text{ kJ per mole } CO_2 \qquad (4.1)$$

$$CO + 2H_2 \leftrightarrow CH_3OH \qquad \Delta H300K = -90.4 \text{ kJ per mole } CO_2 \qquad (4.2)$$

$$CO_2 + 3H_2 \leftrightarrow CH_3OH + H_2O \qquad \Delta H300K = -49.2 \text{ kJ per mole } CO_2 \qquad (4.3)$$

4.3.1.2 Configuration II: Methanol Production with a Recycle

In this configuration, after product stream left an equilibrium reactor, the methanol product was separated as liquid by decreasing a temperature. The vapor phase of a separator was fed back (recycle) to a mixer to combine with feed stream of reactants. The recycle ratio was adjusted to separate vapor phase of product into two streams (recycle and vapor product stream, which combined with liquid product stream). After that, product streams were combined and sent to a purification process. The process simulation of this case was shown in Figure 4.1(b).

4.3.1.3 Configuration III: Methanol Production with Two Reactors in Series

In this configuration, in the first equilibrium reactor, reactants were partially converted to methanol product. Temperature of product stream was then decreased to separate the methanol product as a liquid. The remaining reactants (in vapor phase) were fed to the second equilibrium reactor by increasing in a pressure. The second equilibrium reactor was used to produce addition methanol product. All of liquid methanol products were then combined and sent to purification process. The process simulation of this case was shown in Figure 4.1(c).

มหาวิทยาลัยเทคโนโลยีสุรนารี

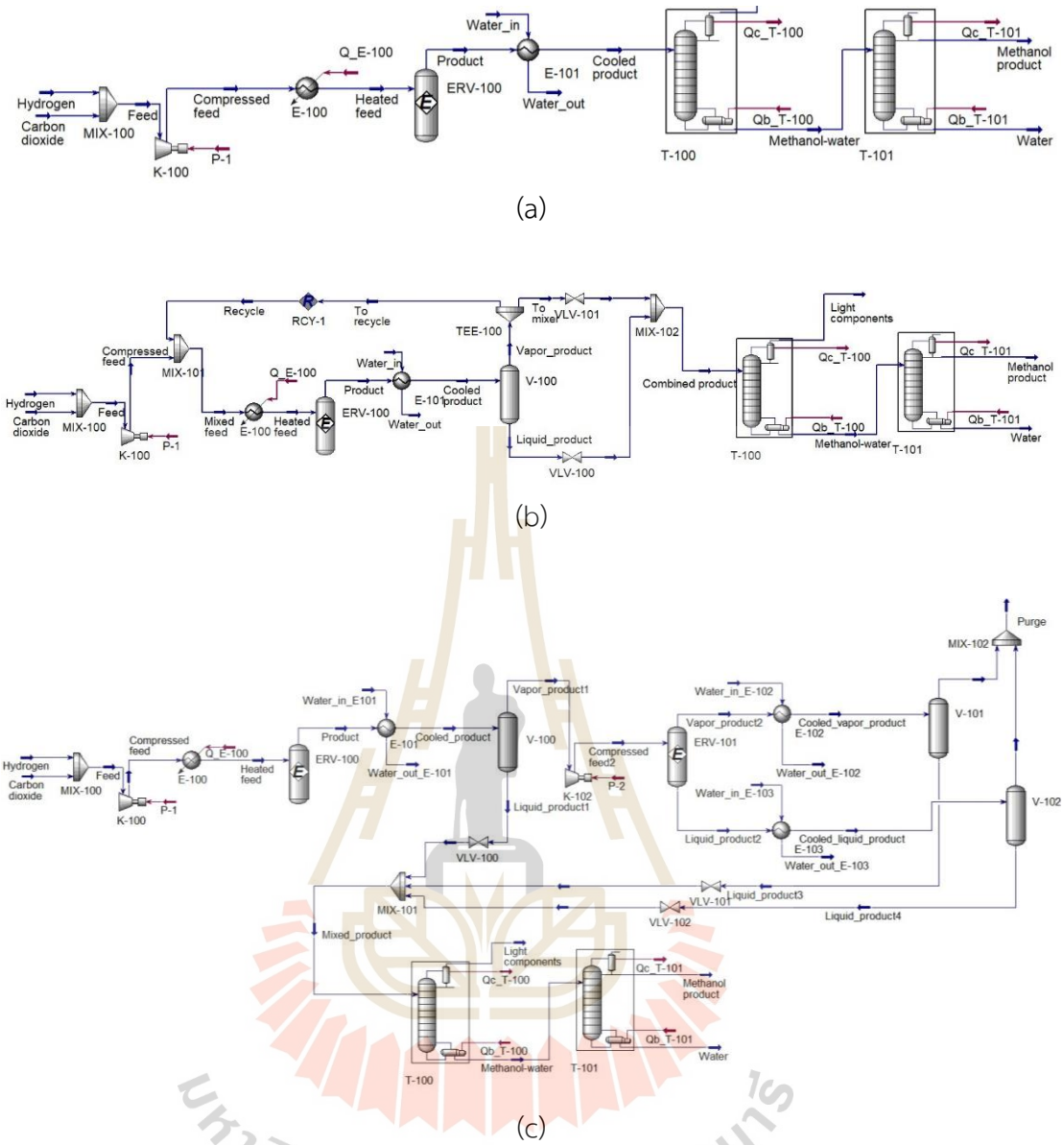

Figure 4.1 Process simulation of the methanol production via carbon dioxide hydrogenation: (a) configuration I; (b) configuration II; and (c) configuration III.

In the simulation, reactors with equilibrium model used reaction sets follow Equations (4.1) to (4.3). Compressors efficiencies were assumed adiabatic at 75%. Reflux ratio of column T-100 was specified at 0.6, and condenser temperature was specified at 25°C. For specifications of column T-10, the reflux ratio was specified at 30,

and methanol purity was specified at 99.5% by mole. Details on parameters of process simulation for each process configuration can be found in Appendix A.1 to A.3.

4.3.2 Economic Evaluation

The analysis of economic for methanol production cost includes capital and operating costs. The capital cost was estimated by using data from the capital equipment-costing program (Turton, Bailie et al., 2003). Cost of piping was not included in the analysis of economic. The value of Chemical Engineering Plant Cost Index, CEPCI in 2017 was used to adjust for inflation from 2001 to 2017. The CEPCI value in 2017 is 541.7 (Jenkins, 2018). Assumptions used in the economic analysis were followed (Borisut and Nuchitprasittichai, 2019). Price of pure carbon dioxide feed was $30 per ton and, price of hydrogen from electrolysis was $3,230 per ton which were obtained from CarbonBrief (Timperley, 2019).

4.3.2.1 Price Sensitivity

The methanol production cost not only depends on its operating conditions but also on prices of raw materials. Therefore, this section studied the impacts of raw material prices on methanol production cost. The configuration III: methanol production with two reactors in series was used as a case study in this study. This is due to this configuration required the lowest methanol production cost than other cases. Sensitivity analysis of prices of carbon dioxide and hydrogen were studied by varying price of each one of reactants within the range of ±25 and ±50 percent from its base price and fixed another price parameter at its base value. In this study, the base price of carbon dioxide was $30 per ton, and the base price of hydrogen was $3230 per ton.

4.4 Simulation-Optimization Methodology

The simulation-optimization methodology of this work was shown in Figure 4.2. There are three decision variables for configuration I: once-through reactor methanol production. Four decision variables for configuration II: methanol production with a recycle, and five decision variables for configuration III: the methanol production with two reactors in series. The list of decision variables and the range of each variable for each process configuration were shown in Table 4.1(a), (b), and (c).

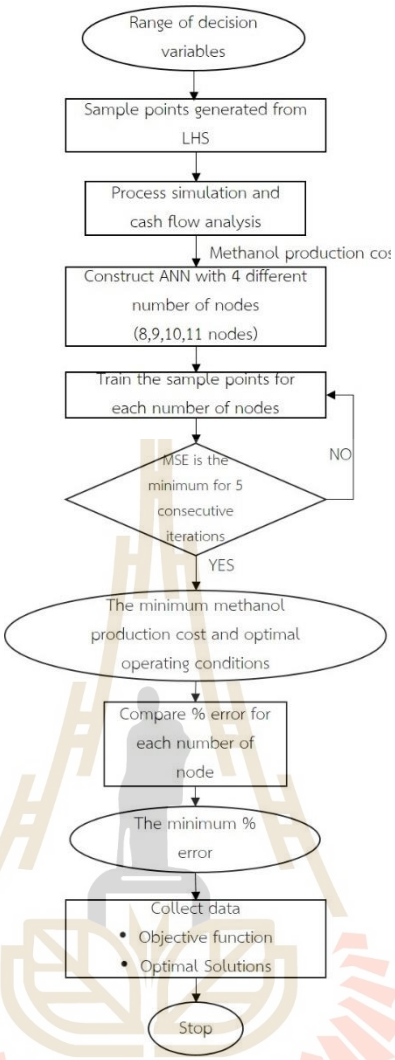

Figure 4.2 Algorithm for Latin hypercube design for Artificial neural network training.

มหาวิทยาลัยเทคโนโลยีสุรนารี

Figure 4.2 shows the optimization algorithm which uses ANN as the objective function. In the algorithm, the suitable ANN configuration was first determined, and then the function was optimized. The algorithm started with the range of each decision variable. Based on previous researchers (Ullmann, 2003; Leonzio, Zondervan et al., 2019; Pérez-Fortes, Schöneberger et al., 2016; Borisut and Nuchitprasittichai, 2019), the range of each decision variable was selected as shown in Table 4.1. Then a data set of decision variables was selected using Latin hypercube sampling (Section 4.1) with amount of ten times *n* sample points, where *n* is number of decision variables. The

corresponding methanol production costs were obtained using process simulation and cash flow analysis.

Artificial neural networks (Section 4.2) with four different nodes (8, 9, 10 and 11 nodes) were constructed. For each number of nodes, the sample points were trained. The mean square error (MSE) of a test set was used as a criterion to determine the suitable ANN configuration (number of nodes). The ANN network was trained until MSE values keep decreasing for five consecutive iterations. Then, ANN parameters (weight and bias) were collected, and used as an objective function in optimization problem. The objective of optimization problem was to minimize the methanol production cost (Section 4.3).

Table 4.1(a) Range of the decision variables of configuration I

Decision variables	Range	
	Lower	Upper
Pressure of the equilibrium reactor (bar)	69	73
Temperature of the equilibrium reactor (°C)	189	193
Temperature of the stream entering a separator (°C)	65	75

Table 4.1(b) Range of the decision variables of configuration II

Decision variables	Range	
	Lower	Upper
Pressure of the equilibrium reactor (bar)	50	70
Temperature of the equilibrium reactor (°C)	190	210
Temperature of the stream entering a separator (°C)	60	80
Recycle ratio	0	1

มหาวิทยาลัยเทคโนโลยีสุรนารี

Table 4.1(c) Range of the decision variables of configuration III

Decision variables	Range	
	Lower	Upper
Pressure of the first equilibrium reactor (bar)	50	70
Temperature of the first equilibrium reactor (°C)	190	210
Temperature of the stream entering a separator (°C)	60	80
Pressure of the second equilibrium reactor (bar)	100	140
Outlet temperature of the liquid stream cooler after the second equilibrium reactor (°C)	60	80

4.4.1 Latin Hypercube Sampling

Latin hypercube sampling was used in this work for data collection to build the ANNs.The number of data points (*N*) of this sampling technique is arbitrary. A data set was generated by equally dividing the range of 0 to 1 into *N* ranges. Then, sample points were randomly picked from each range of each variable. After that, sample points of each independent variable were randomly matched to the ones of other variables. Figure 4.3 represents coded level of data set obtained from LHS with two decision variables and five sample points.

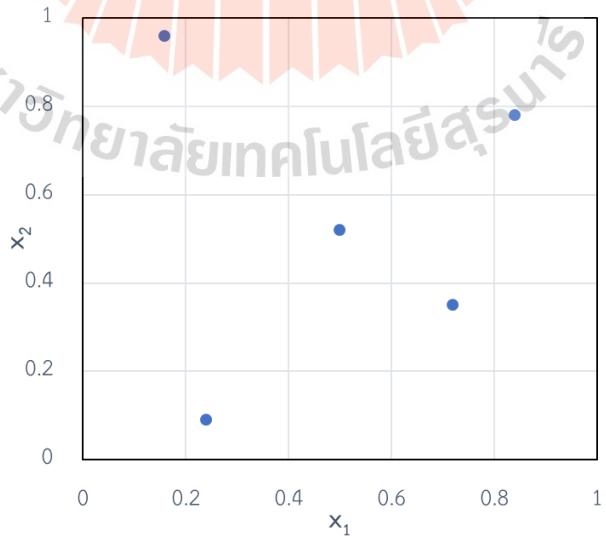

Figure 4.3 Experimental design: Latin hypercube sampling.

4.4.2 Artificial Neural Networks

Artificial neural network (ANN) is mathematical expression consists of interconnected processing unit known as neurons (Basheer and Hajmeer, 2000). The parameters of network contain weight and bias and at each neuron operated using transfer function. In this work, the feed-forward neural network with three-layer (input layer, one hidden layer and output layer) is used to train the data sets. Figure 4.4 represents the schematic of the feed-forward neural network with a single hidden layer. Training algorithm is Levenberg-Marquardt, which automatically stops when generalization stops improving. The data was separated for 70% of training set, 15% of validation set and 15% of testing set.

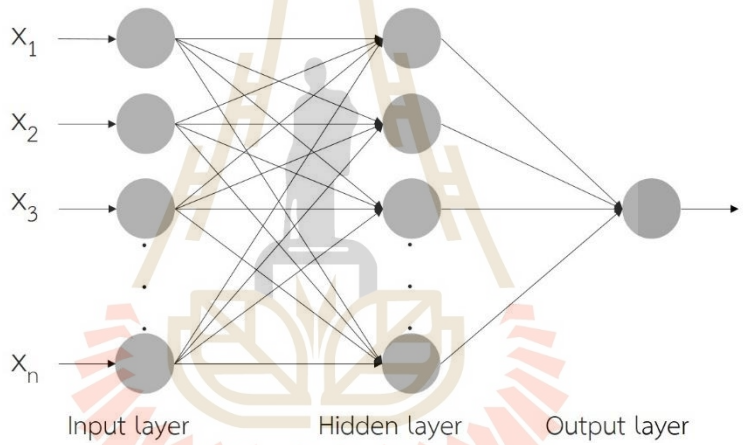

Figure 4.4 The schematic of the feed-forward neural network with a single hidden layer.

4.4.3 Optimization Formulation

The objective functions in this work were obtained by training the data set with artificial neural network. The objective function represents the methanol production costs. In this work, artificial neural network was used an objective function as shown in Equations 4.4 and 4.5. This ANNs three layers design, which consists of input, hidden and output layers, were trained using function *nnstart* in MATLAB. The sigmoid function and linear function were used to represent the data in hidden layer and output layer, respectively with Levenberg-Marquardt algorithm.

For optimization formation of an artificial neural network follows

$$\text{MIN: } y = \left(\sum_r W2_r \times L1_r\right) + B2 \tag{4.4}$$

$$\text{Subject to: } L1_r = \frac{2}{1 + e - 2\left(\sum_r \left(W1_{rn} \times x_r\right) + B1_r\right)} - 1 \tag{4.5}$$

$x_r \in [-1,1]$; decision variables corresponding to each configuration

Where *n* is number of decision variables, *r* is the number of neurons in hidden layer, W1 and W2 are input weights of hidden layer and output layer, respectively. B1 and B2 are biases of input and output layer, respectively.

4.5 Results and Discussion

4.5.1 Price Sensitivity

Figure 4.5 shows the impacts of hydrogen and carbon dioxide prices on methanol production cost. Each methanol production cost shown in Figure 4.6 represents the minimum cost obtained from process optimization. Regarding the impact of hydrogen price, the results showed that hydrogen price has a significant impact on methanol production cost. An increase in hydrogen price from its base value by 50 percent raises the minimum methanol production cost by 38 percent. Conversely, if the hydrogen price decreases by 50 percent from its base price, the minimum methanol production cost (per ton produced methanol) can be reduced from $890.75 to $585.58.

In case of an impact of carbon dioxide price, the minimum methanol production cost slightly increases as the price increases. Hence, the carbon dioxide price has a slight impact on the minimum methanol production cost. This is because the amount of hydrogen feed was consumed three times higher than carbon dioxide feed. The optimization of operating conditions can offset an increase in carbon dioxide price, but the optimization problem cannot offset the increase in hydrogen price. To make methanol production via carbon dioxide hydrogenation a sustainable process, the price of hydrogen has to be considered.

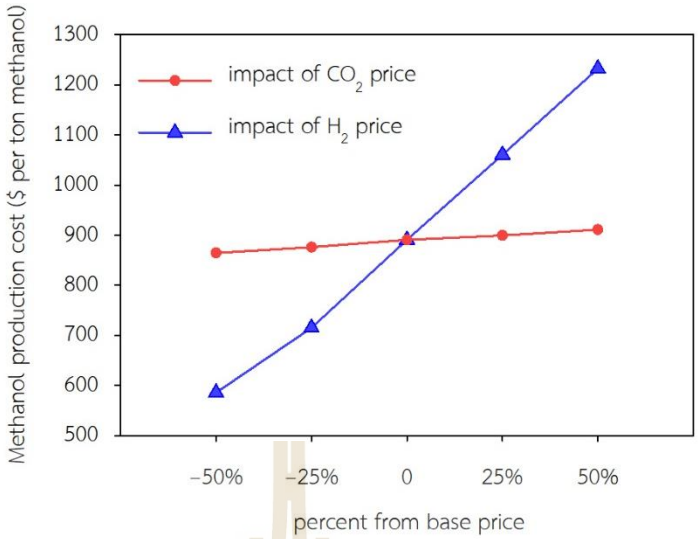

Figure 4.5 The impact of carbon dioxide and hydrogen price on methanol production cost.

4.5.2 Comparison of Different Process Configurations

Table 4.2 shows the optimization results for each number of nodes of each process configuration. The ANNs were trained with four different number of nodes (8, 9, 10, and 11). From Table 4.2(a): configuration I: once – through reactor methanol production, the obtained minimum methanol production cost was $2,353.56 per ton produced methanol. The ANN structure with eight nodes yielded the lowest percent error, which are 0.563. From Table 4.2(b): configuration II: methanol production with a recycle, the obtained minimum methanol production cost was $928.04 per ton produced methanol. This lowest cost and percent error were obtained from the model of ANN structure with eight nodes (percent error of 0.077). From Table 4.2(c): configuration III: methanol production with two reactors in series, the obtained minimum methanol production cost was $888.85 per ton produced methanol. The ANN structure was the same as two other process configurations, which is the structure with eight nodes (percent error of 0.104). When comparing among these three configurations, the results showed that configuration III: methanol production with two reactors in series process required the lowest methanol production cost. The ANN with eight nodes was the most suitable configuration to represent the relation between operating

conditions and methanol production cost for this case study (with all percent errors less than one). The ANN parameters (weight and bias) of each process configuration are included in Supplementary Information S.4-S.6.

Table 4.2(a) Results of fitting data with artificial neural networks for configuration I: once-through reactor methanol production

Number of nodes (N)	8	9	10	11
R-squared	0.9987	0.9891	0.9717	0.9925
MSE	1.01×10^{-3}	3.63×10^{-3}	5.46×10^{-3}	5.74×10^{-3}
Predicted cost ($/ton)	2,340.31	2,284.50	2,291.88	2,280.82
Actual cost ($/ton)	2,353.56	2,330.03	2,334.02	2,337.94
Error (%)	0.563	1.954	1.805	2.443

Table 4.2(b) Results of fitting data with artificial neural networks for configuration II: methanol production with a recycle

Number of nodes (N)	8	9	10	11
R-squared	0.9981	0.9972	0.9966	0.9983
MSE	1.42E-03	3.02E-04	1.38E-03	1.15E-03
Predicted cost ($/ton)	928.76	973.41	770.24	724.95
Actual cost ($/ton)	928.04	964.83	949.68	942.38
Error (%)	0.077	0.889	18.895	23.072

มหาวิทยาลัยเทคโนโลยีสุรนารี

Table 4.2(c) Results of fitting data with artificial neural networks for configuration III: methanol production with two reactors in series

Number of nodes (N)	8	9	10	11
R-squared	0.9669	0.9910	0.9922	0.9884
MSE	7.21E-03	3.02E-03	2.01E-03	2.91E-03
Predicted cost ($/ton)	887.93	886.95	889.81	889.14
Actual cost ($/ton)	888.85	888.70	968.31	968.31
Error (%)	0.104	0.197	8.106	8.177

4.5.3 The Optimal Solutions

Table 4.3 shows the optimal operating conditions and the minimum methanol production cost of each process configuration. Table 4.4 shows energy consumption and energy cost for each equipment for the three process configurations. For configuration I: once-through reactor methanol production, the minimum methanol production cost was $2,353.56 per ton produced methanol. The corresponding optimal operating conditions were as follows: the pressure at the equilibrium reactor of 71.95 bar, the temperature at the equilibrium reactor of 192°C, and the temperature of a cooler of 71.14°C. The minimum methanol production cost of this configuration was considered high because there was only one reactor, and carbon dioxide conversion was around 50 percent. Therefore, the methanol production cost per ton was high due to the low amount of methanol product (12,358 kg/hr).

Table 4.3 Optimal operating conditions and minimum methanol production cost of three configurations

Decision variables	Optimal conditions		
	Configuration I	Configuration II	Configuration III
Pressure of the first equilibrium reactor (bar)	71.95	70	70
Temperature of the first equilibrium reactor (°C)	191.99	192.10	199.04
Temperature of the stream entering a separator (°C)	-	61.24	80
Temperature of cooler (°C)	71.14	-	-
Recycle ratio	-	1	-
Pressure of the second equilibrium reactor (bar)	-	-	100
Outlet temperature of the liquid stream cooler after the second equilibrium reactor (°C)	-	-	80
Predicted cost ($/ton)	2,340.31	928.76	887.93
Actual cost ($/ton)	2,353.56	928.04	888.85
Error (%)	0.563	0.077	0.104

For configuration I (once-through reactor methanol production), the minimum methanol production cost was $2,353.56 per ton produced methanol. The corresponding optimal operating conditions were as follows: pressure at the equilibrium reactor of 71.95 bar, temperature at the equilibrium reactor of 192 °C, and the

temperature of the cooler of 71.14 °C. The minimum methanol production cost of this configuration was considered high because there was only one reactor, and carbon dioxide conversion was around 50 percent. The total energy consumption of this configuration was 5847.6 kW. However, the methanol production cost per ton was high due to a low amount of methanol product (12,358 kg/h).

Table 4.4 Energy consumption and energy cost for equipment for three configurations

Configuration	Energy Consumption/Energy cost		
	Equipment	Energy (kW)	Cost ($/year)
I	K-100	5645.8	6,022,855.6
	E-100	201.8	215,234,6
II	K-100	5502.0	5,869,491.4
	E-100	6739.8	7,189,968.1
III	K-100	5502.0	5,869,491.4
	E-100	607.6	648,201.5
	K-102	926.6	988,473.4

For process configuration II (methanol production cost with a recycle), the minimum methanol production cost was $928.04 per ton produced methanol. The optimal operating conditions were as follows: pressure of an equilibrium reactor of 70 bar, temperature of an equilibrium reactor of 192.10 °C, temperature of the stream entering a separator of 61.24 °C, and recycle ratio of one (full recycle). The results of this process configuration agreed with the work of Leonzio et al. (Leonzio, Zondervan et al. 2019) that a higher recycle ratio resulted in higher methanol yield. However, the power consumption of a heater was increased with an increase in the recycle ratio, which results in high methanol production cost for this process configuration. The power consumption of the heater in this process configuration was ten times higher than the process configuration without recycle. The total energy consumption of this configuration was 12,241.8 kW.

For process configuration III: methanol production with two reactors in series, the minimum methanol production cost per ton produced methanol was $888.85, which is the lowest cost among the three configurations. The optimal operating conditions were as follows: pressure of the first equilibrium reactor of 70 bar, temperature of the first equilibrium reactor of 199.04 °C, temperature of the stream entering a separator of 80 °C, pressure of the second equilibrium reactor of 100 bar, and outlet temperature of the liquid stream cooler after the second equilibrium reactor of 80 °C. This configuration resulted in the lowest methanol production cost due to a higher methanol yield than the other two configurations. The amount of methanol product in the process configuration was 31,036 kg/h. Moreover, the total energy consumption of this configuration was comparable to configuration I, being 7036.2 kW.

4.6 Conclusions

This chapter compared three different process configurations of methanol production via carbon dioxide hydrogenation. Latin hypercube sampling was employed as sampling technique to generate a data set of studied parameters. An artificial neural network with four different number of nodes were constructed to represent the relationship between operating conditions and methanol production cost. Three configurations include once-through reactor methanol production, methanol production with a recycle, and methanol production with two reactors in series. Each process configuration was optimized for the minimum methanol production cost. The minimum methanol production costs were compared among these process configurations. The results showed that the methanol production with two reactors in series required the lowest methanol production cost. The optimal operating conditions were as follows: the pressure of the first equilibrium reactor of 70 bar, the temperature of the first equilibrium reactor of 199.04°C, the temperature of the stream entering a separator of 80°C, the pressure of the second equilibrium reactor of 100 bar, the outlet temperature of the liquid stream cooler after the second equilibrium reactor of 80°C.

4.7 References

Arena, F., G. Mezzatesta, L. Spadaro and G. Trunfio (2014). Latest Advances in the Catalytic Hydrogenation of Carbon Dioxide to Methanol/Dimethylether. Transformation and Utilization of Carbon Dioxide. B. M. Bhanage and M. Arai. Berlin, Heidelberg, Springer Berlin Heidelberg: 103-130.

Atsonios, K., K. D. Panopoulos and E. Kakaras (2016). Thermocatalytic CO_2 hydrogenation for methanol and ethanol production: Process improvements. International Journal of Hydrogen Energy 41(2): 792-806.

B.Vaferi, M.Bahmani, S. M. Babakhani and M.A.Khademi (2014). Modification and optimization of the industrial methanol production process. Indian Journal of Chemical Technology 10(2): 051-059.

Basheer, I. A. and M. Hajmeer (2000). Artificial neural networks: fundamentals, computing, design, and application. Journal of Microbiological Methods 43(1): 3-31.

Bill, A. (1998). Carbon dioxide hydrogenation to methanol at low pressure and temperature, EPFL.

Borisut, P. and A. Nuchitprasittichai (2019). Methanol Production via CO_2 Hydrogenation: Sensitivity Analysis and Simulation—Based Optimization. Frontiers in Energy Research 7(81).

Bowker, M. (2019). Methanol Synthesis from CO_2 Hydrogenation. ChemCatChem 11(17): 4238-4246.

Eason, J. and S. Cremaschi (2014). Adaptive sequential sampling for surrogate model generation with artificial neural networks. Computers & Chemical Engineering 68: 220-232.

F.R.Machado, C., J. L. d. Medeiros and O. F. Q. Araújo (2014). comparative analysis of methanol production routes: synthesis gas versus CO_2 hydrogenation. International Conference on Industrial Engineering and Operations Management. Bali, Indonesia.

Jadhav, S. G., P. D. Vaidya, B. M. Bhanage and J. B. Joshi (2014). Catalytic carbon dioxide hydrogenation to methanol: A review of recent studies. Chemical Engineering Research and Design 92(11): 2557-2567.

Jenkins, S. (2018). CEPCI UPDATES: JANUARY 2018 (PRELIM.) AND DECEMBER 2017 (FINAL). January 2017. 2018.

Jin, Y., J. Li, W. Du and F. Qian (2016). Adaptive Sampling for Surrogate Modelling with Artificial Neural Network and its Application in an Industrial Cracking Furnace. The Canadian Journal of Chemical Engineering 94(2): 262-272.

Leonzio, G. (2017). Optimization through Response Surface Methodology of a Reactor Producing Methanol by the Hydrogenation of Carbon Dioxide. Processes 5(4).

Leonzio, G., E. Zondervan and P. U. Foscolo (2019). Methanol production by CO_2 hydrogenation: Analysis and simulation of reactor performance. International Journal of Hydrogen Energy 44(16): 7915-7933.

Liang, X.-L., X. Dong, G.-D. Lin and H.-B. Zhang (2009). Carbon nanotube-supported Pd–ZnO catalyst for hydrogenation of CO_2 to methanol. Applied Catalysis B: Environmental 88(3): 315-322.

Liu, C., X. Guo, Q. Guo, D. Mao, J. Yu and G. Lu (2016). Methanol synthesis from CO_2 hydrogenation over copper catalysts supported on MgO-modified TiO_2. Journal of Molecular Catalysis A: Chemical 425: 86-93.

Matr, D. L. (2018). Process modelling and simulation of a methanol synthesis plant using syngas streams obtained from biomass. Master of Science, Politecnico di Milano.

Mukherjee, A., J. A. Okolie, A. Abdelrasoul, C. Niu and A. K. Dalai (2019). Review of post-combustion carbon dioxide capture technologies using activated carbon. Journal of Environmental Sciences 83: 46-63.

Naims, H. (2016). Economics of carbon dioxide capture and utilization—a supply and demand perspective. Environmental Science and Pollution Research 23(22): 22226-22241.

Nexant. (2018). Market Analytics: Methanol and Derivatives - 2018.

Pellegrini, L. A., G. Soave, S. Gamba and S. Langè (2011). Economic analysis of a combined energy–methanol production plant. Applied Energy 88(12): 4891-4897.

Pérez-Fortes, M., J. C. Schöneberger, A. Boulamanti and E. Tzimas (2016). Methanol synthesis using captured CO_2 as raw material: Techno-economic and environmental assessment. Applied Energy 161: 718-732.

Roh, K., T. B. H. Nguyen, U. Suriyapraphadilok, J. H. Lee and R. Gani (2015). Development of sustainable CO_2 conversion processes for the methanol production. Computer Aided Chemical Engineering. K. V. Gernaey, J. K. Huusom and R. Gani, Elsevier. 37: 1145-1150.

Sudakov, O., D. Koroteev, B. Belozerov and E. Burnaev (2019). Artificial Neural Network Surrogate Modeling of Oil Reservoir: A Case Study. Advances in Neural Networks – ISNN 2019, Cham, Springer International Publishing.

Tidona, B., C. Koppold, A. Bansode, A. Urakawa and P. Rudolf von Rohr (2013). CO_2 hydrogenation to methanol at pressures up to 950 bar. The Journal of Supercritical Fluids 78: 70-77.

Timperley, J. (2019). Renewable hydrogen ‘already cost competitive’, say researchers. Retrieved November 2019.

Turton, R., R. C. Bailie, W. B. Whiting and J. A. Shaeiwitz (2003). Analysis, synthesis and design of chemical processes, Prentice Hall.

Ullmann's Encyclopedia of Industrial Chemistry (2003), VCH.

Ye, J. (2019). Artificial neural network modeling of methanol production from syngas. Petroleum Science and Technology 37(6): 629-632.

Zander, S., E. L. Kunkes, M. E. Schuster, J. Schumann, G. Weinberg, D. Teschner, N. Jacobsen, R. Schlögl and M. Behrens (2013). The Role of the Oxide Component in the Development of Copper Composite Catalysts for Methanol Synthesis. Angewandte Chemie International Edition 52(25): 6536-6540.

มหาวิทยาลัยเทคโนโลยีสุรนารี

CHAPTER V

ADAPTIVE LATIN HYPERCUBE SAMPLING FOR SURROGATE-BASED OPTIMIZATION WITH ARTIFICIAL NEURAL NETWORK

5.1 Abstract

A significant number of sample points are often required for surrogate-based optimization when utilizing process simulations to cover the entire system space. This necessity is particularly pronounced in complex simulations or high-dimensional physical experiments, where a large number of sample points is essential. The chapter represents the development of an adaptive Latin hypercube sampling (LHS) method that generates additional sample points from areas with the highest output deviations to optimize the required number of samples. The surrogate model used for the optimization problem is artificial neural networks (ANNs). The standard for measuring solution accuracy is the percent error of the optimal solution. The outcomes of the proposed algorithm were compared to those of random sampling for validation. As case studies, we chose three different chemical processes to illustrate problems of varying complexity and numbers of variables. The findings indicate that, for all case studies, the proposed LHS optimization algorithm required fewer sample points than random sampling to achieve optimal solutions of similar quality. To extend the application of this methodology, we recommend further applying it to fields beyond chemical engineering and higher-dimensional problems.

5.2 Introduction

For many engineering problems, simulation is an essential method to understand the behavior of real systems accurately. In numerous research projects, simulation is employed to interpret complex models, reducing the time and cost associated with real-world process operations. A surrogate model, also known as a meta-model, can be created using a set of input-output data obtained from simulations or experiments. In this context, the simulation is considered a 'black box,' where the

functions and underlying assumptions of the simulation are unknown, except for the process output (Crombecq, Laermans et al., 2011).

The popular surrogate model is Response Surface Methodology (RSM), which is evaluated through the regression of input-output data using low-order polynomials. In recent years, RSM has been applied in several chemical processes to study the effects of independent factors (Ahmadi, Mesbah et al., 2021; Bashir, Amr et al., 2015; Bezerra, Santelli et al., 2008; Hoseiny, Zare et al., 2016; Leonzio, 2017; Mohammad, Ghaemi et al., 2019; Veljković, Veličković et al., 2018). It has also been used in treatment processes to improve removal efficiency and reduce operating costs (Ahmadi, Mesbah et al., 2021). However, for complex processes, low-order polynomials have limitations in capturing highly nonlinear behavior (Simpson, Poplinski et al., 2001). Generally, RSM provides local optimization results. Therefore, global surrogate models such as Kriging interpolation and Artificial Neural Networks (ANNs) have been proposed to overcome these limitations. Kriging interpolation offers an accurate model that provides better global approximations compared to low-order polynomial models. It predicts output values at specific inputs that match the simulated output values (Beers and Kleijnen 2004). Kriging interpolation fits a spatial correlation function to a set of input-output pairs, and the data points are used in linear interpolation (Eason and Cremaschi, 2014). However, it's important to note that this surrogate model may have limitations due to available support software. Several surrogate models have been used in the past years, including Artificial Neural Networks (ANNs), Radial Basis Function (RBF), and Random Forest (RF) (Bliek, 2022). ANNs are a powerful tool for various applications, such as approximating nonlinear systems, process modeling, and optimization (Panerati, Schnellmann et al., 2019). They can fit many complex nonlinear functions and apply to numerous processes in chemical engineering (Jin, Li et al., 2016; Vaklieva-Bancheva, Vladova et al., 2019). ANNs were coupled with another machine learning technique such as the genetic algorithm (Hoseinian, Rezai et al., 2020; Bahrami, Ardejani et al., 2016) and simulated annealing (Bahrami, Ardejani et al., 2016; Mousavi, Mostafavi et al., 2017) for application in the engineering process. ANNs are commonly employed due to their simplicity and ability to handle challenging nonlinear mappings (Zendehboudi, Rezaei et al., 2018). These mathematical models have been used in both laboratory (Eslamimanesh, Gharagheizi et al., 2011; Mohammadpoor and Torabi 2018) and industry

(Jin, Li et al., 2016; Bhutani, Rangaiah et al., 2006; Zorzetto, Maciel Filho et al., 2000). In 2020, Tahkola et al. developed a surrogate model for electrical machine torque using grid sampling combined with ANNs, and the results demonstrated the effectiveness of this sampling approach in modeling torque behavior (Tahkola, Keränen et al., 2020). Many studies have shown that ANNs can provide accurate models for various engineering disciplines (Adeli, 2001; Arora, Shen et al., 2017; Himmelblau, 2000; Shahin, Jaksa et al., 2008; Nayak, Jain et al., 2001; Wang and Luo, 2022). Therefore, ANNs were employed to develop accurate models for the chemical process case studies in this work.

To build the model that describes the relationship between any input and output, the sampling technique is also required to construct the experiment which points of any responses. In order to generate the sample points, the design of experiment (DoE) is necessary. Therefore, the study of design of experiment (DoE) is necessary in order to select the numbers and locations of sample points. The development of modern DoE techniques can be categorized into two types which are static and adaptive (Garud, Karimi et al., 2017). Factorial design, Latin hyper-cube sampling, Monte Carlo method, and orthogonal array are classified as static DoE. Factorial design is widely used due to its simplest form of space-filling design, which covers most of the considered regions of variables (Morshed, Pervez et al., 2020; Villa Montoya, da Silva Mazareli et al., 2020). The first modern design of experiment is Monte Carlo or random sampling, which generates sample points in the design space using random numbers. This technique requires a large number of sample points to represent the entire problem space. Subsequently, Quasi-Monte Carlo was introduced to achieve a uniform distribution of sample points across the design space by using low-discrepancy sequences. Three popular quasi-random low-discrepancy sequences are Hal-ton, Hammersley, and Sobol sequences. However, these sampling techniques, including random sampling, demand a large sample size to achieve a highly accurate model, which results in high costs and time consumption during real process operations. Therefore, the proposed Latin hypercube sampling was studied to address these challenges. Latin hypercube sampling exhibits a beneficial property known as optimum non-collapsing. However, generating Latin hypercube sample points presents challenges, particularly in terms of achieving uniform distribution across the design

space. Additionally, in high-dimensional problems, a large number of sample points is needed to adequately cover the design space.

Therefore, this chapter introduced adaptive Latin hypercube sampling to determine the necessary sample points for representing the design space in simulation-based optimization. The objective of the algorithm is to generate the fewest sample points while achieving the best feasible optimal solution. The algorithm started with a small number of sample points from Latin hypercube sampling. Additional sample points were then generated and sequentially added to an original data set. Artificial Neural Networks (ANNs) were employed as a surrogate model. The optimal results obtained from the proposed algorithm were compared with those obtained from random sampling. Three chemical processes were used as case studies to represent problems with varying complexity and numbers of factors. Three replications of each case study were conducted to assess the consistency of the method.

Section 5.3 provides reviews of Latin hypercube sampling, random sampling, and artificial neural networks. Section 5.4 presents the proposed adaptive Latin hypercube sampling for surrogate-based optimization. Section 5.4.4 introduces details of three different case studies: (1) ammonia production from syngas, (2) methanol production via CO_2 hydrogenation, and (3) CO_2 capture using Rectisol process to represent three different types of surrogate-based optimization problems. Section 5.5 offers results, discussion, recommendations, and future work. Finally, Section 5.6 presents the conclusion.

5.3 Sampling Technique and Surrogate Modeling

This section provides information on sampling techniques and surrogate models. Section 5.3.1 describes Latin hypercube sampling, Section 5.3.2 provides information on random sampling. Information on the artificial neural network can be found in Chapter 4 (section 4.4.2). In this chapter, a single hidden layer with eight neurons was employed in the ANN network.

5.3.1 Latin Hypercube Sampling

Latin hypercube sampling was first proposed in 1979 by M.D. Mckey et al. (McKay, Beckman et al., 1979). It is a method for generating samples that cover the entire sample space without any replications. The technique involves dividing each dimension of the sample space into N equally likely intervals for N sample points. The fundamental principle of Latin hypercube sampling is to ensure that each stratum is sampled exactly once, thereby guaranteeing a comprehensive representation of the entire sample space. For instance, in Latin Hypercube Sampling (LHS) involving two factors and ten sample points, the range of each factor, typically from 0 to 1, is partitioned into ten equal intervals. Each sample point is then randomly chosen from one of these intervals, creating a distinctive and stratified LHS dataset. Each interval accommodates only one sample point, which is randomly paired with other variables. You can observe this LHS dataset in Figure 5.1(a).

One advantage of Latin Hypercube Sampling (LHS) is that, by selecting input points independently, it ensures that the sampled points are spread across the entire parameter space without clustering in any particular region. This reduces the risk of overemphasizing certain areas of the space, which can occur with other random sampling methods. Moreover, LHS ensures that once a point is sampled, it will not be selected again. This feature minimizes redundancy in the samples, allowing the system to focus on exploring new regions of the parameter space, leading to different output results. The illustration of Latin Hypercube Sampling is shown in Figure 5.1. However, the worst-case scenario for Latin Hypercube Sampling may result in poorly sampled spaces, as depicted in Figure 5.1(b), which may not adequately represent the entire domain space. Therefore, in any field that uses Latin Hypercube Sampling as a sampling technique for optimization problems, it is essential to ensure that samples cover the entire parameter space (space-filling).

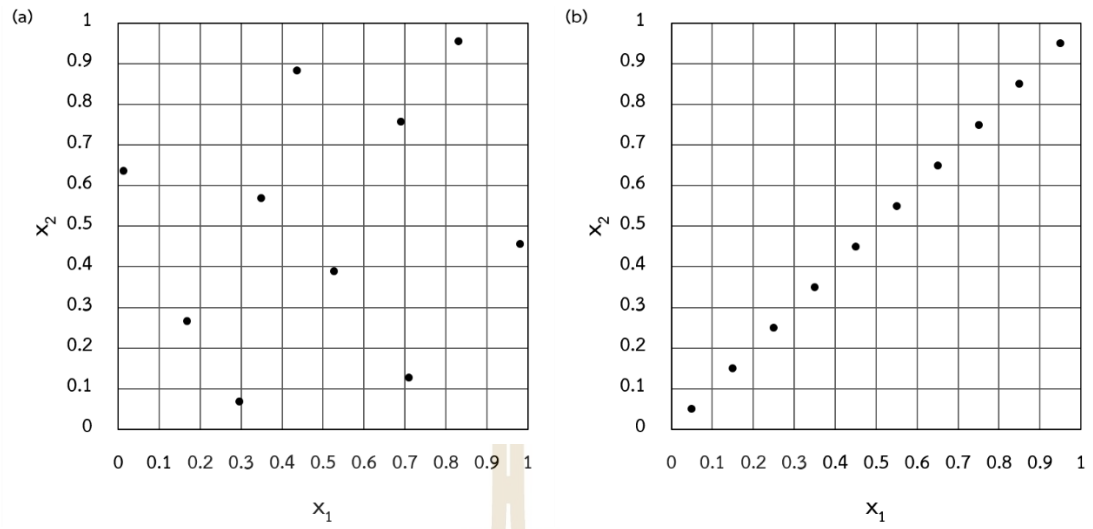

Figure 5.1 Illustration of Latin hypercube sampling for N = 10 of (a) good filling design (b) poor filling design.

To address the primary challenge in Latin Hypercube Sampling, researchers have explored various criteria to generate well-filling Latin Hypercube designs, aiming to enhance their performance. Table 5.1 summarizes the criteria used in Latin Hypercube Sampling. The two most common criteria used in Latin Hypercube Sampling (LHS) involve maximizing the minimum inter-point distance between pairs of sample points and minimizing the correlation between pairs of columns in the sample matrix (Sheikholeslami and Razavi, 2017). By maximizing the minimum distance, LHS avoids the problem of points clustering in certain regions of the parameter space. Clustering can lead to bias in estimation and might cause important regions of the space to be overlooked. By minimizing the correlation between pairs of columns in the LHS matrix, it ensures that the selected variables or factors are as orthogonal as possible. This means that the variables are as independent as possible, and each factor has less influence on the others. This makes it easier to identify the individual impact of each variable on the system's output. However, when dealing with a large number of sample points or when integrating them with the optimization of a specific case study, these algorithms may require more computational time and become complex.

Table 5.1 The approach for constructing optimal latin hypercube sampling

Algorithm	Criteria	Pros.	Cons.
Simulated annealing (Grosso, Jamali et al., 2009; Morris and Mitchell, 1995; Pholdee and Bureerat, 2015)	Maximize the inter-point distance	Effective for small-size problems	Converge very slowly
Exchange type and Newton-type (Park, 1994)	Maximize entropy	Fast to find optimal design for large-size problems	
Columnwise-pairwise (Ye, Li et al., 2000)	Maximize the inter-point distance and Maximize entropy	Retain some orthogonality and high efficiency for small designs	Does not significantly reduce the searching time
Threshold accepting (Fang, 2002)	Minimize L_2-discrepancy	Can be applied to both factorial and computer experiment	Cannot give a good design for small dimension
Genetic algorithm (Bates, Sienz et al., 2004)	Maximize the inter-point distance	Require a small amount of computational time	
Enhanced stochastic evolutionary algorithm (Jin, Chen et al., 2005)	Maximize the inter-point distance, Maximize entropy and Minimize L_2-discrepancy	Needs small number of exchanges Effective for large-size problem	
Branch-and-bound (van Dam, Husslage et al., 2007)	Maximize the inter-point distance	Can be used for non-collapsing designs	Obtain the optimum design for N < 70

Table 5.1 The approach for constructing optimal Latin hypercube sampling (continued)

Algorithm	Criteria	Pros.	Cons.
Translational propagation (Viana, Venter et al., 2010)	Maximize the inter-point distance	Obtain near optimum LHDs up to medium dimensions	High computational cost for large number of sample points
Particle swarm optimization (Aziz and Tayarani- N, 2014; Chen, Hsieh et al., 2013)	Maximize the inter-point distance	Fast accessibility to reach solutions	Local search algorithms get trapped in local optima
Translational propagation (Pan, Ye et al., 2014)	Maximize the inter-point distance and Minimize L_2-discrepancy	Effective in terms of the computation time and space-filling and projective properties	Not good in terms of performance of sampling points
Enhanced stochastic evolutionary algorithm (Husslage, Rennen et al., 2011)	Maximize the inter-point distance	Effective for large-size problem	

In order to reduce computational time, the adaptive Latin hypercube with sequential design is an intriguing choice for case studies involving process simulation. Adaptive sampling strategies typically begin with a small sample size and then sequentially add points based on specific criteria. In 2003, Wang proposed an adaptive response surface methodology model using inherited Latin hypercube sampling points (Wang, 2003). This sampling approach involves adding new sample points in underrepresented areas. Subsequently, in 2018, Chang applied this technique instead of central composite design to calculate the failure probability of a complex turbine blade structure (Chang, Sun et al., 2018). The results demonstrated the effectiveness of this approach when combined with Gaussian Process Regression for

structural reliability analysis. Another variation of adaptive Latin hypercube sampling, which initially identifies the region of interest, was introduced by Roussouly (Roussouly, Petitjean et al., 2013). After marking the location and sampling the first point, the region is subdivided to add two more sample points. Finally, two additional sample points are introduced using another two-point Latin hypercube. This technique offers advantages for reliability analysis by focusing sampling efforts solely on the areas of interest. Zhi-zhao Liu and colleagues proposed two general extension algorithms for Latin hypercube sampling: basic general extension and general extension based on the greedy algorithm (Liu, Yang et al., 2016). These algorithms aim to preserve the majority of the original Latin hypercube points. While the general extension approach can be time-consuming, the general extension based on the greedy algorithm reduces computational time, though it may lead to the removal of some of the original points. In 2016, a rigorous Latin hypercube sampling method was coupled with a sophisticated algorithm to ensure the retention of all initial points (Liu, Yang et al., 2016).

5.3.2 Random Sampling

Monte Carlo or random sampling was the first modern sampling design for computer experiments, proposed by Metropolis and Ulam in 1949 (Metropolis and Ulam, 1949). Random sampling requires a large number of sample points (N) to achieve a high level of accuracy in surrogate modeling. However, this approach consumes more computational time and is time-consuming in terms of data collection. Figure 5.2 illustrates random sampling.

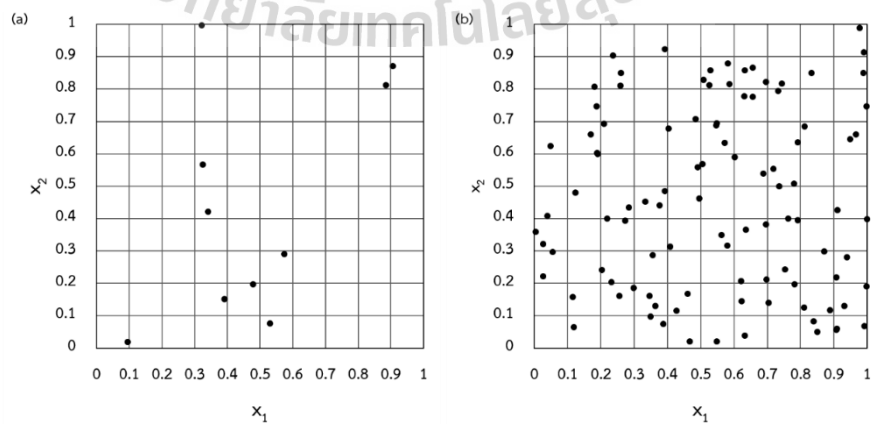

Figure 5.2 Illustration of random sampling for (a) N = 10, (b) N = 100.

5.4 Methodology

The methodology of this work is divided into three sections. In Section 5.4.1, we introduce the adaptive Latin Hypercube sampling approach for surrogate-based optimization, which focuses on solving optimization problems using a small set of sample points. The algorithm's optimal solutions are validated through outcomes obtained via random sampling. Section 5.4.2 covers the details of Adaptive LHS in the proposed surrogate-based optimization, while Section 5.4.3 offers detailed insights into optimization using random sampling. Adaptive Latin Hypercube sampling is a sequential sampling method that in-creases the number of sample points one by one until it meets the algorithm's criteria. In contrast, random sampling is a one-time operation that generates the entire set of sample points at once without the option to add more. In this work, if the number of sample points in random sampling cannot adequately represent the entire surface, the algorithm will generate a new initial dataset with twice the number of sample points as in the previous set.

5.4.1 Proposed Adaptive Latin Hypercube Sampling for Surrogated-based Optimization

Figure 5.4 represents the proposed adaptive Latin hypercube sampling for surrogate-based optimization. At the beginning of the algorithm, ranges of factors that have effects on the output value were assigned. Then, the first dataset of x_{kn} (with desired number of sample points) was generated using Latin hypercube sampling where k = 1, 2, 3, ..., K and n = 1, 2, 3, ..., N_0, (K is number of decision variable, N is number of sample point). The initial number of sample points was set at seven times the number of factors. The corresponding output values, y_n, were obtained from process simulation combined with an economic analysis. The sets of input and output were normalized in the range of -1 to 1 for ANNs training using MATLAB with a three-layer design (input layer, hidden layer, and output layer).

For ANNs training, the Levenberg-Marquardt algorithm was used. The dataset was split into 70% for training, 15% for validation, and 15% for testing. The criteria used to determine the accuracy of the ANN model are the mean square error (MSE) (Borisut and Nuchitprasittichai 2020) and the R-squared (R^2) value. The training loop for ANNs was terminated when the MSE value of the ANN model remained at a

minimum for 5 consecutive iterations, and the R^2 value of the model was greater than or equal to 0.995. The weights and biases of the most recent ANN model were then used as the objective function for the optimization problem to determine the optimal solution ($x_{i,opt}$ and $\hat{y}_{opt}$). The optimal operating conditions ($x_{i,opt}$) were then input into the process simulation to obtain the corresponding output value (y_{opt}). The accuracy of the obtained optimal solution is deemed acceptable if the percent error between the predicted output value (obtained from the ANN model) and the actual output value (obtained from process simulation), as shown in Equation (5.1), is within a preset value of 1 percent. If the percent error is less than one, the optimization algorithm is terminated, and the most recent optimal solution is reported as the optimal solution of the problem.

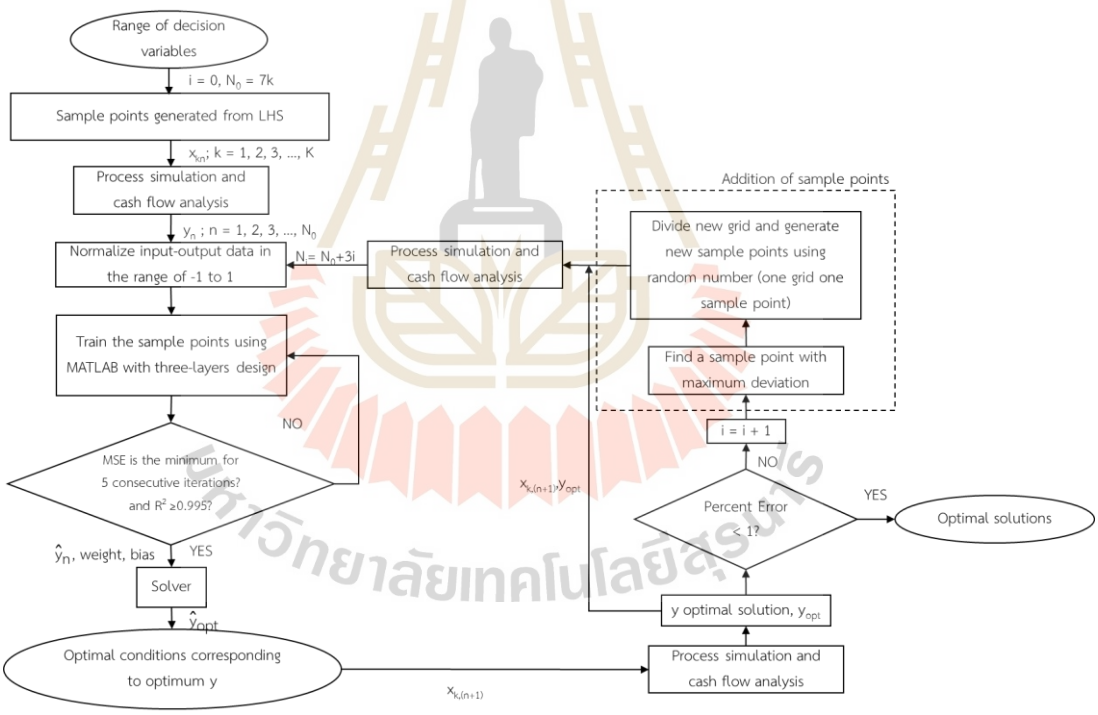

Figure 5.3 Proposed adaptive Latin hypercube sampling for surrogate-based optimization.

$$\text{Percent error} = \frac{\left|y_{n+1} - \hat{y}_{n+1}\right|}{y_{n+1}} \times 100 \qquad (5.1)$$

5.4.2 Adaptive Latin Hypercube Sampling for Optimization

In the step involving the addition of sample points in adaptive LHS, two additional sample points are generated during each iteration. To determine these sample points, the deviation from their respective actual values for all (N_0+3i) predicted outputs is calculated for each sample point in the dataset. Where i represents the number of iterations. The sample point that exhibits the highest deviation, denoted as (x_n, $y_{n,max\ deviation}$) is selected. Subsequently, the intervals corresponding to the sample point with the highest deviation (x_n, $y_{n,max\ deviation}$) are evenly divided into two intervals. Two additional sample points are then randomly selected from each of these intervals.

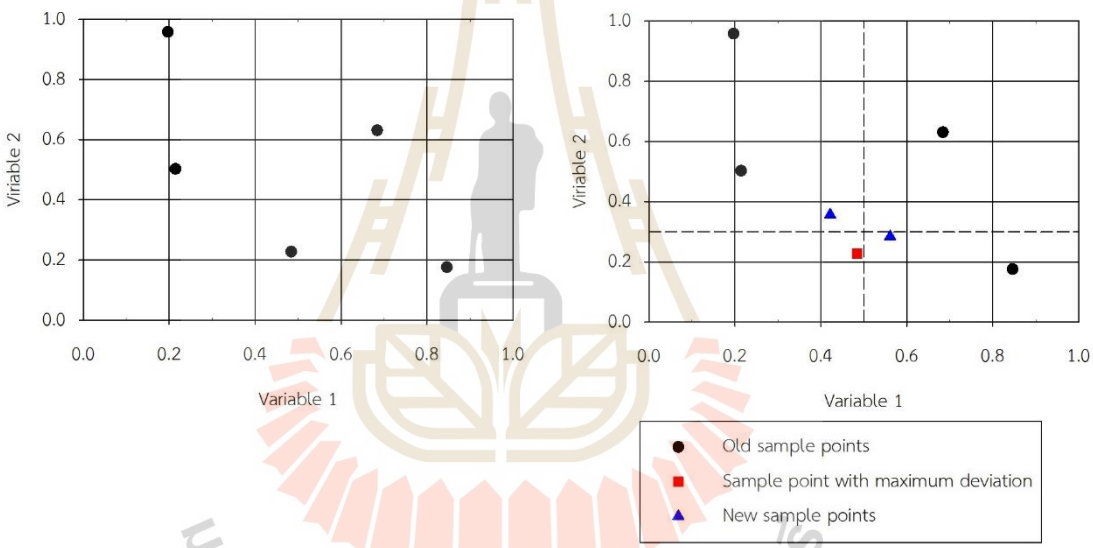

Figure 5.4 Additional sample points using maximum deviation.

Figure 5.4 illustrates an example of generating two additional sample points from the highest deviation output sample point. This example showcases the generation of sample points for two factors, denoted as x_1 and x_2. The highest deviation sample point (x_n, $y_{n,max\ deviation}$) is represented as a red dot. The intervals corresponding to these sample points are within the ranges of 0.4 to 0.6 for factor 1 and 0.2 to 0.4 for factor 2. Both factors are evenly divided into two intervals: 0.4 to 0.5 and 0.5 to 0.6 for factor 1, and 0.2 to 0.3 and 0.3 to 0.4 for factor 2 (as indicated by dashed lines). Next,

one sample point is randomly selected from each interval of the factors. A total of two additional sample points are obtained and represented as blue dots.

5.4.3 Verification of the Optimal Solution Using Random Sampling Technique

Figure 5.5 illustrates the simulation-optimization algorithm using the random sampling technique. The algorithm commenced with the same input ranges and factors as the proposed simulation-optimization method employing adaptive LHS. Initially, 50 sample points were used. Output data was collected, and ANNs were trained using the same stopping criterion as in the proposed method. The resulting ANN model was then subjected to optimization using a nonlinear solver to obtain the optimal solution. The accuracy of the optimal solution was evaluated using the same criteria as in the proposed algorithm. The algorithm terminated and reported the optimal solution if the percent error of the solution was less than one. If not, additional points were generated and added to the original samples, doubling the recent sample size (N x 2). These additional points were then processed through the simulation, and the steps were repeated until the determined optimal solution achieved a percent error of less than one.

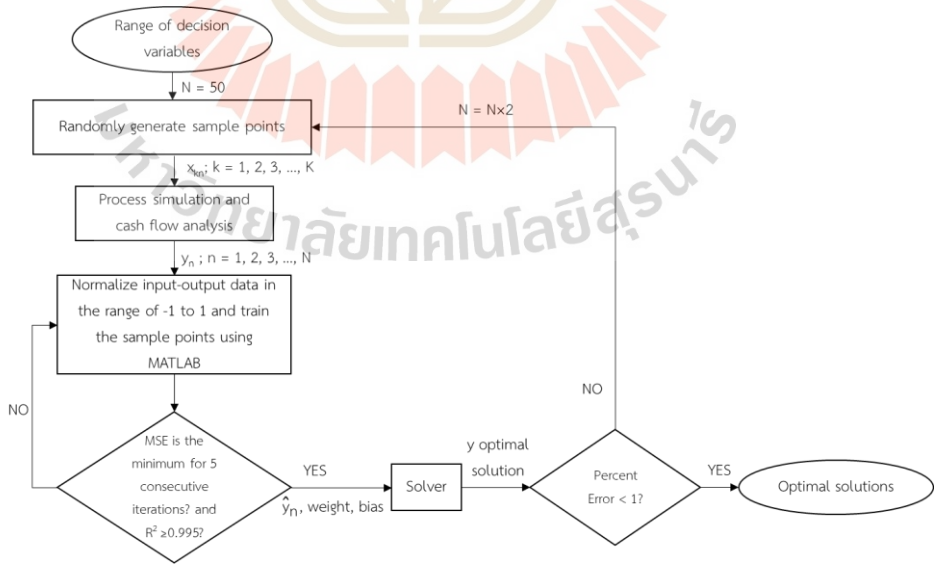

Figure 5.5 Random sampling for optimization.

5.4.4 Case Studies

To illustrate the varying complexity and number of factors in the problem, this section examines three distinct chemical processes as case studies. Case Study I focuses on ammonia production from syngas, which involves three factors. Case Study II explores methanol production via carbon dioxide hydrogenation, which deals with four factors. Case Study III addresses CO_2 absorption by methanol using the Rectisol process, which involves five factors. The details of each case study are provided below.

5.4.4.1 Case Study 1: Ammonia Production from Syngas

The first case study addresses an optimization problem with three decision variables. Figure 5.6 depicts the process simulation of ammonia production based on the Haber process. The process involves feeds of 31,900 kilograms per hour of natural gas at 35 bar and 25°C, as well as 95,800 kilograms per hour of high-pressure steam at 150 bar. Further de-tails on the process simulation and conditions can be found in the work of Janosovsky (Janosovský, Danko et al., 2019). Ammonia production comprises two main parts: the production of syngas and the production of ammonia (Equation (5.14)). The syngas production includes steps such as steam reforming (Equations (5.2)-(5.5)), air reforming (Equations (5.7)-(5.10)), high and low shift conversion (Equation (5.11)), CO_2 removal, and methanation (Equations (5.12)-(5.13)). The reaction for each step are as follows.

Steam reforming (Reformer unit)

$$CH_4 + H_2O \longrightarrow CO + 3H_2 \quad (5.2)$$

$$C_2H_6 + 2H_2O \longrightarrow 2CO + 5H_2 \quad (5.3)$$

$$C_3H_8 + 3H_2O \longrightarrow 3CO + 7H_2 \quad (5.4)$$

$$C_4H_8 + 4H_2O \longrightarrow 4CO + 9H_2 \quad (5.5)$$

Air reforming (Combuster unit)

$$2CO + O_2 \longrightarrow 2CO_2 \quad (5.6)$$

$$2H_2 + O_2 \longrightarrow 2H_2O \quad (5.7)$$

$$CH_4 + 2O_2 \longrightarrow 2H_2O + CO_2 \quad (5.8)$$

$$2C_2H_6 + 7O_2 \longrightarrow 6H_2O + 4CO_2 \quad (5.9)$$

$$C_3H_8 + 5O_2 \longrightarrow 4H_2O + 3CO_2 \quad (5.10)$$

Water gas shift reaction

$$CO + H_2O \leftrightarrow CO_2 + H_2 \quad (5.11)$$

Methanation (Methanizer unit)

$$CO + 3H_2 \leftrightarrow CH_4 + H_2O \quad (5.12)$$

$$CO_2 + 4H_2 \leftrightarrow CH_4 + 2H_2O \quad (5.13)$$

Ammonia production (PFR-100, PFR-101, and PFR-102 units)

$$N_2 + 3H_2 \longrightarrow 2NH_3 \quad (5.14)$$

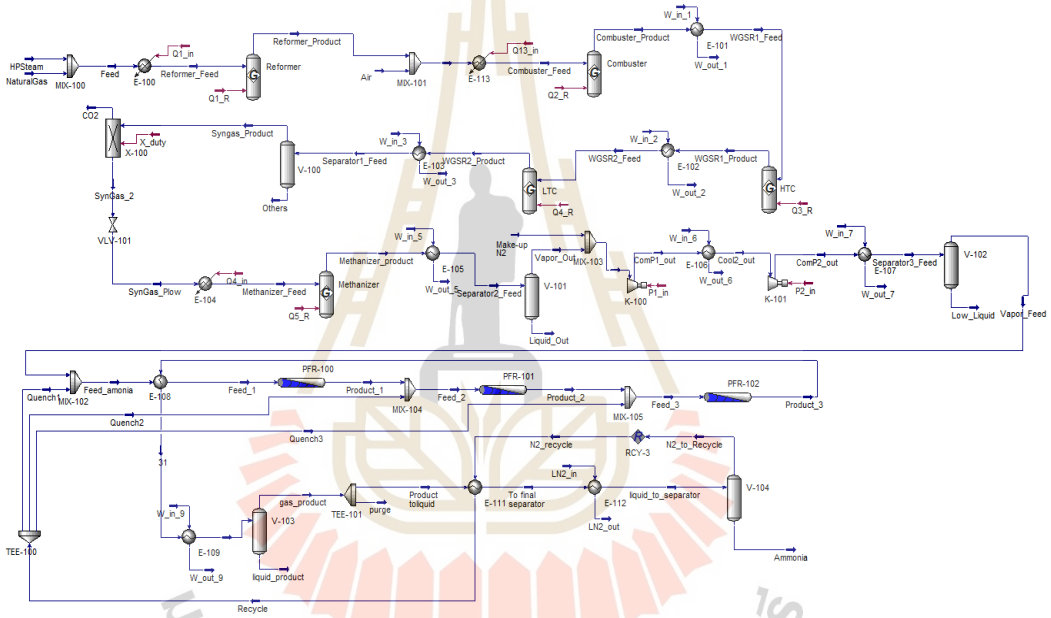

Figure 5.6 Process simulation of ammonia production from syngas.

For the process optimization, three decision variables are the reformer temperature, the combuster temperature, and the low-temperature conversion reactor temperature. The ranges of these decision variables are shown in Table 5.2. The temperatures of the high temperature conversion reactor, methanizer, and ammonia reactor were fixed at 450°C, 340°C and 450°C, respectively. A two-stage compressor was used to increase the pressure of the stream up to 150 bar before entering the ammonia synthesis loop. The ammonia synthesis system was modeled using three plug flow reactors in series with three quenching sections. The final product,

ammonia, was separated by a separation unit at 45°C, with ammonia content exceeding 98 mol%. More details for replicating the process simulation are provided in Appendix A.7.

Table 5.2 Range of decision variables of case study 1

Decision variables	Range	
	Lower	Upper
Reformer temperature (°C)	900	1,200
Combuster temperature (°C)	1,400	1,700
Low temperature conversion reactor temperature (°C)	160	290

5.4.4.2 Case Study 2: Methanol Production via Carbon Dioxide Hydrogenation

The second case study represents an optimization problem with four decision variables. Figure 5.7 depicts the process simulation of methanol production via carbon dioxide hydrogenation with a recycling process. The decision variables were (1) pressure of the equilibrium reactor, (2) temperature of the equilibrium reactor, (3) temperature of the steam entering a separator, and (4) the recycle ratio. This simulation used the Peng-Robinson thermodynamics package. The feed stream of the process consisted of 1,000 kmoles per hour of carbon dioxide and 3,000 kmoles per hour of hydrogen at conditions of 20 bar and 40°C. The process's specification was to achieve a methanol product purity of 99.5% by mole. The range of each decision variable is shown in Table 5.3. Details of the economic evaluation assumptions for this process can be found in the work of Borisut & Nuchitprasittichai (Borisut and Nuchitprasittichai 2020). Additional information for reproducing the process simulation is provided in Appendix A.8.

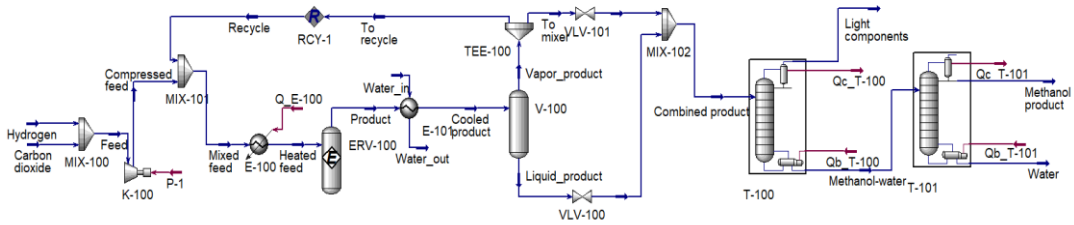

Figure 5.7 Process simulation of methanol production via carbon dioxide hydrogenation.

Table 5.3 Range of decision variables of case study 2

Decision variables	Range	
	Lower	Upper
Pressure of the equilibrium reactor (bar)	50	70
Temperature of the equilibrium reactor (°C)	190	210
Temperature of the steam entering a separator (°C)	60	80
Recycle ratio	0	1

5.4.4.3 Case Study 3: CO_2 Absorption by Methanol via Rectisol Process

The third case study represents an optimization problem with five decision variables. Figure 5.8 illustrates the process of CO_2 absorption by methanol via the Rectisol process. The process consists of three main sections: water removal, absorption, and CO_2/methanol separation. The syngas feed contains a mole fraction of 0.2462 of CO_2, 0.0002 of NH_3, 0.0044 of CO, 0.0050 of Ar, 0.4148 of N_2, 0.3186 of H_2, 0.0035 of H_2O, and 0.0073 of CH_4 at 17.24 bar and 18.30°C (Adams, Salkuyeh et al. 2014). A small amount of methanol was mixed with the syngas feed and sent to the first separator to separate water from the feed gas. Subsequently, the syngas was fed to an absorber column, where CO_2 gas was captured by chilled methanol added at the top of the column. The rich methanol then passes through a three-stage separator and is fed into a stripper column to separate CO_2 from methanol. The lean methanol leaving the stripper was mixed with 40 kmoles per hour of makeup methanol and recycled to the absorber. The vapor product from the stripper, primarily containing CO_2 was

combined to others CO_2 product streams from the second and third separators. Details for replicating the process simulation are provided in Appendix A.9.

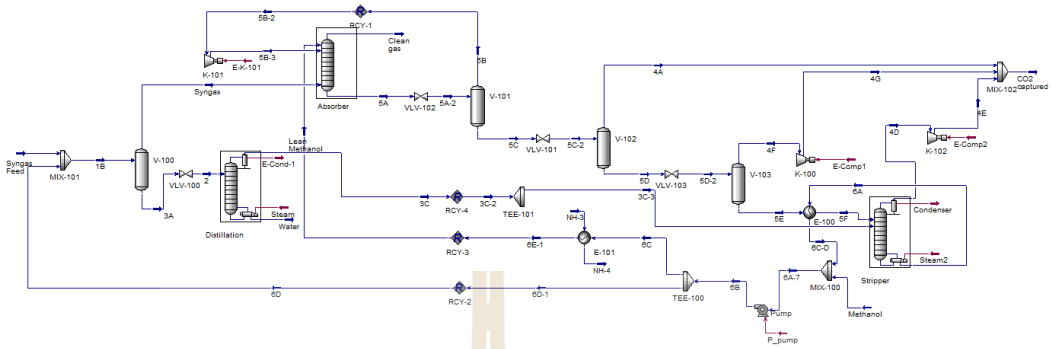

Figure 5.8 Process simulation of CO_2 captured via Rectisol process.

In the optimization of this process, the decision variables included the lean methanol temperature, the third-stage separator pressure, stripper reflux ratio, stripper inlet temperature, and distillation reflux ratio. The ranges of these decision variables are detailed in Table 5.4.

Table 5.4 Range of decision variables of case study 3

Decision variables	Range	
	Lower	Upper
Lean methanol temperature (°C)	-55	-20
The 3rd stage separator pressure (bar)	1.2	2
Stripper reflux ratio	5	20
Stripper inlet temperature (°C)	10	40
Distillation reflux ratio	1	10

5.5 Results and Discussion

The results and discussions are presented in four sections. In Section 5.5.1, we describe the optimal results obtained from random sampling, which started with an initial number of 50 sample points. Section 5.5.2 discusses the convergence of the proposed adaptive Latin Hypercube Sampling (LHS) algorithm. In Section 5.5.3, we

provide a comparison between the optimal results obtained from the random sampling technique and those obtained from the proposed adaptive sampling method. Section 5.5.4 includes recommendations for Future Work. The dataset for all three case studies can be found in Appendix A (Table A.13 to A.15).

5.5.1 The Results of Random Sampling

The Monte Carlo or random sampling was used to verify the optimal results obtained from the proposed adaptive sampling LHS optimization algorithm. The starting sample points for random sampling were set at 50, and they were then doubled until the solution satisfied the criteria. Table 5.5 shows the results obtained from random sampling technique for each iteration for all three case studies. The criterion for the ANN model is that the R^2 value of the model has to be greater than or equal to 0.995. The criterion for the optimal solution is the percent error of the optimal cost has to be less than one (1).

Table 5.5 Result of random sampling of three case studies

Case studies	Case study I		Case study II		Case study III			
sample points	50	100	50	100	50	100	200	400
R-squared	0.9998	0.9999	1.0000	1.0000	0.9951	0.9999	0.9912	0.9998
Minimum cost	495.87	495.87	942.45	942.45	49.70	43.66	43.20	43.40
Predicted cost	505.89	496.73	926.29	948.23	39.37	42.83	45.88	43.66
Error	2.02%	0.17%	1.71%	0.61%	20.80%	1.91%	6.21%	0.59%

The results showed that in the case of Case Study I (ammonia production from syngas) and Case Study II (methanol production via carbon dioxide hydrogenation), 100 sample points were required to meet the criteria. The obtained minimum ammonia production cost was $495.87 for Case study I, and the minimum methanol production cost was $495.87 for Case study II. For the results of Case study III (CO_2 absorption by methanol via Rectisol process), the optimization problem required 400 sample points to meet the criteria. The minimum CO_2 capture cost was $43.40.

5.5.2 The Convergence of the Proposed Adaptive LHS Optimization

Figure 5.9 illustrates the convergence of the proposed algorithm for all three case studies. In the figure, the symbols triangle, black circle, and white circle

represent the actual cost (obtained from process simulation), predicted cost (obtained from the optimization problem), and the percent error, respectively. The percent error between actual and predicted costs is depicted as a dashed line. The proposed algorithm terminates when the percent error of the optimal cost was less than one percent (1%).

มหาวิทยาลัยเทคโนโลยีสุรนารี

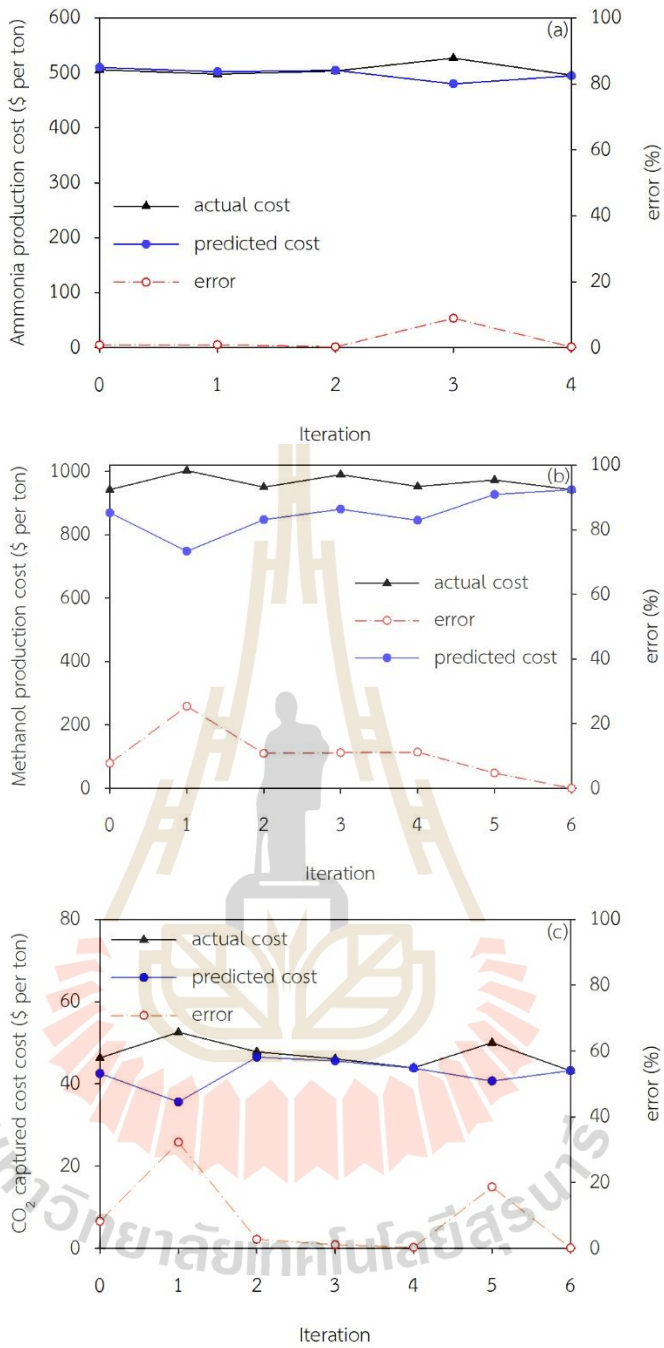

Figure 5.9 The convergence of the proposed algorithm for all three case studies: (a) ammonia production from syngas, (b) the production of methanol from carbon dioxide hydrogenation, (c) carbon dioxide absorption by methanol via Rectisol process.

For Case studies I and III (Figure 5.9(a) and 5.9(c)), the outcomes exhibited a similar pattern, where the percent error decreased as more iterations were added. There were a few points where the percent error sharply rose before the algorithm converged. This was due to the fact that sample points for ANN training, testing, and validation were randomly chosen from the data set, resulting in an insufficient number of data points before the algorithm converged. For Case study II, as shown in Figure 5.9(b), the percent error of the optimal solution decreased as the number of iterations (or sample points) increased until it eventually became less than one percent. In all three case studies, each of which featured a different number of independent parameters, the proposed method consistently converged to provide optimal results that met the necessary criteria. Details on the ANNs, including the weights and biases, for all three case studies, can be found in Appendix A.10 and A.11.

Considering the scale of the case studies, the first case study, which included three studied factors, reached convergence after four iterations. Case studies II and III, which had four and five studied factors, respectively, converged after six iterations. The results showed that the algorithm required more iterations to converge when dealing with higher-dimensional problems.

5.5.3 Comparison of Optimal Solutions Between Proposed Sampling and Random Sampling

This section compares the outcomes of the proposed adaptive LHS optimization algorithm with those of random sampling to verify the results. Additionally, the number of sample points required to obtain the optimal solution is compared in this section. The number of sample points used in constructing the ANN model is crucial. Having a sufficient number of sample points to represent the relationship between independent and dependent variables allows the mathematical model to accurately depict the system, enabling the solver to find the true optimal solutions for the optimization problem.

Table 5.6 provides a comparison of the optimal results obtained from random sampling and the proposed algorithm. Three replications of the proposed algorithm were conducted to ensure consistency. For Case study I (ammonia production from syngas), the optimal operating conditions for all three variables

obtained from the proposed algorithm matched those determined by random sampling. The optimal operating conditions were temperatures of 900°C for the reformer, 1400°C for the combuster, and 160°C for the low-temperature conversion reactor, resulting in a minimum production cost of $495.87 per ton of generated ammonia, which was consistent with the results from random sampling. Notably, the proposed technique required only 38 sample points to find the optimal solution for this problem with three decision variables, compared to the 100 sample points needed by random sampling.

Table 5.6 Comparison the results of proposed adaptive Latin hypercube sampling and random sampling

Case study 1: ammonia production from syngas										
Sampling Techniques	Total number of sample points	R^2	x_1 (°C)	x_2 (°C)	x_3 (°C)	x_4	x_5	$y_{predicted}$ ($\hat{y}$) ($ per ton)	y_{actual} (y) ($ per ton)	% error
Random sampling	100	0.9999	900	1400	160	N/A	N/A	496.73	495.87	0.17
Proposed algorithm										
Replication 1	38	0.9928	900	1400	160	N/A	N/A	498.40	495.87	0.51
Replication 2	30	0.9995	900	1400	160	N/A	N/A	495.22	495.87	0.13
Replication 3	30	0.9987	900	1400	160	N/A	N/A	492.14	495.83	0.74
Case study 2: methanol production via carbon dioxide hydrogenation										
Sampling Techniques	Total number of sample points	R^2	x_1 (bar)	x_2 (°C)	x_3 (°C)	x_4 (-)	x_5	$y_{predicted}$ ($\hat{y}$) ($ per ton)	y_{actual} (y) ($ per ton)	% error
Random sampling	100	1.0000	70	190	80	1	N/A	942.80	942.45	0.61
Proposed algorithm										
Replication 1	46	1.0000	70	190	80	1	N/A	942.37	942.45	0.01
Replication 2	46	0.9993	70	190	80	1	N/A	943.85	942.45	0.15
Replication 3	40	0.9991	70	190	76	1	N/A	944.31	945.94	0.17
Case study 3: carbon dioxide absorption by methanol via Rectisol process										
Sampling Techniques	Total number of sample points	R^2	x_1 (°C)	x_2 (bar)	x_3 (-)	x_4 (°C)	x_5 (-)	$y_{predicted}$ ($\hat{y}$) ($ per ton)	y_{actual} (y) ($ per ton)	% error
Random sampling	400	0.9998	-29.0	1.20	5	40	1	43.66	43.40	0.59
Proposed algorithm										
Replication 1	53	0.9958	-20.0	1.20	5	40	1	45.74	45.47	0.60
Replication 2	50	0.9987	-20.0	1.27	5	40	1	45.91	45.67	0.51
Replication 3	53	0.9980	-26.7	1.28	5	40	1	43.25	43.19	0.14

The optimal operating conditions for Case Study II (methanol production from car-bon dioxide hydrogenation) were determined using the proposed algorithm for three replications, and they matched those determined by random sampling, with the exception of the temperature of the steam entering the separator (x_3) in the third replication. In the third replication, the steam's temperature entering the separator (x_3) is 76°C, which was slightly different from the temperatures obtained in the other replications (80°C). A slight decrease in the temperature of the stream entering the separator resulted in an increase in the methanol production cost. This change did not have a significant impact in terms of model prediction error. Furthermore, the third replication used only 40 sample points to represent the entire surface, while the other two replications used 46 sample points. This indicates that the model with 40 sample points found a local optimum. The optimal operating conditions for this case study were a pressure of 70 bar for the equilibrium reactor, a temperature of 190°C for the reactor, a temperature of 80°C for the steam entering a separator, and a recycling ratio of 1. The lowest cost to generate methanol was $942.45 per tonne of methanol. While random sampling required 100 sample points to find the optimal solution for this problem with four decision variables, the proposed adaptive LHS optimization approach only required 46 sample points.

For Case study III (carbon dioxide absorption by methanol via Rectisol process), the values of the optimal operating conditions were identical to those obtained from random sampling, except for the value of the lean methanol temperature (x_1). The results for the lean methanol temperature (x_1) from three replications varied from – 26.70 to – 20.0°C, which was slightly different from the values obtained from random sampling (– 29.0°C). The lowest CO_2 capture costs identified by the proposed algorithm for three replications ranged from $43.25 to $45.91 per ton of CO_2 capture, consistent with the lowest cost identified by random sampling ($43.40 per ton of CO_2 capture). The optimal operating parameters for this case study included a lean methanol temperature of – 26.70°C, a third-stage separator pressure of 1.28 bar, a stripper reflux ratio of 5, a stripper input temperature of 40°C, and a distillation reflux ratio of 1. The minimum cost for CO_2 capture was $43.19 per tonne of CO_2. The proposed technique required only 53 sample points for this problem with five decision

variables, while random sampling needed 400 sample points to achieve the same level of ANN model accuracy and obtain the optimal solutions.

Based on the results of the three different case studies, adaptive Latin Hypercube sampling required fewer sample points than random sampling to accurately represent the entire surface using ANN models. The model accuracy and optimal conditions achieved using adaptive sampling were comparable to random sampling but required fewer sample points.

5.6 Conclusions

This chapter proposes an adaptive Latin hypercube sampling method for simulation-based optimization problems. The algorithm uses the deviation of the output as a criterion for generating new sample points. After each iteration, three additional sample points are added to the existing dataset. The first additional sample point is the optimal solution from the previous optimization dataset, while the other two additional data points are selected from a grid area with the maximum deviation in output. Artificial neural networks (ANNs) were employed as the surrogate model for the optimization problem. The accuracy of the ANN model was assessed using the mean square error (MSE) and R-squared (R^2) values. The criterion for determining the accuracy of the optimal solution was that the percent error should be less than one percent. The results demonstrate that the proposed algorithm is capable of obtaining optimal solutions that are similar to the random sampling approach but require fewer sample points.

One of the primary advantages of the developed algorithm is its versatility. While in this work we exclusively applied adaptive sampling with ANNs, we envision broader applications across various surrogate models. The adaptability of the Latin hypercube sampling method makes it a valuable tool for optimizing complex systems where obtaining accurate models is crucial. Looking forward, we recommend further exploration of adaptive Latin hypercube sampling in comparison to other adaptive sampling methods, particularly in the context of high-dimensional optimization problems. These future investigations will provide more insights into the algorithm's scalability and efficiency.

5.7 References

Adams, T. A., Y. K. Salkuyeh and J. Nease (2014). Chapter 6 - Processes and simulations for solvent-based CO_2 capture and syngas cleanup. Reactor and Process Design in Sustainable Energy Technology. F. Shi. Amsterdam, Elsevier: 163-231.

Adeli, H. (2001). Neural Networks in Civil Engineering: 1989–2000. Computer-Aided Civil and Infrastructure Engineering 16(2): 126-142.

Ahmadi, S., M. Mesbah, C. A. Igwegbe, C. D. Ezeliora, C. Osagie, N. A. Khan, G. L. Dotto, M. Salari and M. H. Dehghani (2021). Sono electro-chemical synthesis of $LaFeO_3$ nanoparticles for the removal of fluoride: Optimization and modeling using RSM, ANN and GA tools. Journal of Environmental Chemical Engineering 9(4): 105320.

Anawkar, S. and A. Panchwadkar (2022). Comparison between Levenberg Marquart, Bayesian and scaled conjugate algorithm for prediction of cutting forces in face milling operation. AIP Conference Proceedings, AIP Publishing.

Arora, S., W. Shen and A. Kapoor (2017). Neural network based computational model for estimation of heat generation in $LiFePO_4$ pouch cells of different nominal capacities. Computers & Chemical Engineering 101: 81-94.

Aziz, M. and M.-H. Tayarani- N (2014). An adaptive memetic Particle Swarm Optimization algorithm for finding large-scale Latin hypercube designs. Engineering Applications of Artificial Intelligence 36: 222-237.

Bahrami, S., F. D. Ardejani and E. Baafi (2016). Application of artificial neural network coupled with genetic algorithm and simulated annealing to solve groundwater inflow problem to an advancing open pit mine. Journal of Hydrology 536: 471-484.

Bashir, M. J., S. A. Amr, S. Q. Aziz, N. C. Aun and S. Sethupathi (2015). Wastewater treatment processes optimization using response surface methodology (RSM) compared with conventional methods: Review and comparative study. Middle-East Journal of Scientific Research 23(2): 244-252.

Bates, S., J. Sienz and V. Toropov (2004). Formulation of the Optimal Latin Hypercube Design of Experiments Using a Permutation Genetic Algorithm. 45th AIAA/ASME/ASCE/AHS/ASC Structures, Structural Dynamics & Materials Conference, American Institute of Aeronautics and Astronautics.

Beers, W. C. M. v. and J. P. C. Kleijnen (2004). Kriging interpolation in simulation: a survey. Proceedings of the 2004 Winter Simulation Conference, 2004.

Bezerra, M. A., R. E. Santelli, E. P. Oliveira, L. S. Villar and L. A. Escaleira (2008). Response surface methodology (RSM) as a tool for optimization in analytical chemistry. Talanta 76(5): 965-977.

Bhutani, N., G. Rangaiah and A. Ray (2006). First-principles, data-based, and hybrid modeling and optimization of an industrial hydrocracking unit. Industrial & engineering chemistry research 45(23): 7807-7816.

Bliek, L. (2022) A Survey on Sustainable Surrogate-Based Optimisation. Sustainability 14 DOI: 10.3390/su14073867.

Borisut, P. and A. Nuchitprasittichai (2020). Process Configuration Studies of Methanol Production via Carbon Dioxide Hydrogenation: Process Simulation-Based Optimization Using Artificial Neural Networks. Energies 13(24).

Chang, Y., Z. Sun, W. Sun and Y. Song (2018). A New Adaptive Response Surface Model for Reliability Analysis of 2.5D C/SiC Composite Turbine Blade. Applied Composite Materials 25(5): 1075-1091.

Chen, R.-B., D.-N. Hsieh, Y. Hung and W. Wang (2013). Optimizing Latin hypercube designs by particle swarm. Statistics and Computing 23(5): 663-676.

Crombecq, K., E. Laermans and T. Dhaene (2011). Efficient space-filling and non-collapsing sequential design strategies for simulation-based modeling. European Journal of Operational Research 214(3): 683-696.

Eason, J. and S. Cremaschi (2014). Adaptive sequential sampling for surrogate model generation with artificial neural networks. Computers & Chemical Engineering 68: 220-232.

Eslamimanesh, A., F. Gharagheizi, A. H. Mohammadi and D. Richon (2011). Artificial neural network modeling of solubility of supercritical carbon dioxide in 24 commonly used ionic liquids. Chemical engineering science 66(13): 3039-3044.

Fang, K.-T. (2002). THEORY, METHOD AND APPLICATIONS OF THE UNIFORM DESIGN. International Journal of Reliability, Quality and Safety Engineering 09(04): 305-315.

Garud, S. S., I. A. Karimi and M. Kraft (2017). Design of computer experiments: A review. Computers & Chemical Engineering 106: 71-95.

Grosso, A., A. R. M. J. U. Jamali and M. Locatelli (2009). Finding maximin latin hypercube designs by Iterated Local Search heuristics. European Journal of Operational Research 197(2): 541-547.

Himmelblau, D. M. (2000). Applications of artificial neural networks in chemical engineering. Korean Journal of Chemical Engineering 17(4): 373-392.

Hoseinian, F. S., B. Rezai, E. Kowsari and M. Safari (2020). A hybrid neural network/genetic algorithm to predict Zn (II) removal by ion flotation. Separation Science and Technology 55(6): 1197-1206.

Hoseiny, S., Z. Zare, A. Mirvakili, P. Setoodeh and M. R. Rahimpour (2016). Simulation–based optimization of operating parameters for methanol synthesis process: Application of response surface methodology for statistical analysis. Journal of Natural Gas Science and Engineering 34: 439-448.

Husslage, B. G. M., G. Rennen, E. R. van Dam and D. den Hertog (2011). Space-filling Latin hypercube designs for computer experiments. Optimization and Engineering 12(4): 611-630.

Janosovský, J., M. Danko, J. Labovský and L. Jelemenský (2019). Software approach to simulation-based hazard identification of complex industrial processes. Comput. Chem. Eng. 122: 66-79.

Jin, R., W. Chen and A. Sudjianto (2005). An efficient algorithm for constructing optimal design of computer experiments. Journal of Statistical Planning and Inference 134(1): 268-287.

Jin, Y., J. Li, W. Du and F. Qian (2016). Adaptive Sampling for Surrogate Modelling with Artificial Neural Network and its Application in an Industrial Cracking Furnace. The Canadian Journal of Chemical Engineering 94(2): 262-272.

Leonzio, G. (2017). Optimization through Response Surface Methodology of a Reactor Producing Methanol by the Hydrogenation of Carbon Dioxide. Processes 5(4).

Liu, Z.-z., W. Li and M. Yang (2015). Two General Extension Algorithms of Latin Hypercube Sampling. Mathematical Problems in Engineering 2015: 450492.

Liu, Z., M. Yang and W. Li (2016). A Sequential Latin Hypercube Sampling Method for Metamodeling. Theory, Methodology, Tools and Applications for Modeling and Simulation of Complex Systems, Singapore, Springer Singapore.

McKay, M. D., R. J. Beckman and W. J. Conover (1979). A Comparison of Three Methods for Selecting Values of Input Variables in the Analysis of Output from a Computer Code. Technometrics 21(2): 239-245.

Metropolis, N. and S. Ulam (1949). The Monte Carlo Method. Journal of the American Statistical Association 44(247): 335-341.

Mohammad, N. K., A. Ghaemi and K. Tahvildari (2019). Hydroxide modified activated alumina as an adsorbent for CO_2 adsorption: Experimental and modeling. International Journal of Greenhouse Gas Control 88: 24-37.

Mohammadpoor, M. and F. Torabi (2018). A new soft computing-based approach to predict oil production rate for vapour extraction (VAPEX) process in heavy oil reservoirs. The Canadian Journal of Chemical Engineering 96(6): 1273-1283.

Morris, M. D. and T. J. Mitchell (1995). Exploratory designs for computational experiments. Journal of Statistical Planning and Inference 43(3): 381-402.

Morshed, M. N., M. N. Pervez, N. Behary, N. Bouazizi, J. Guan and V. A. Nierstrasz (2020). Statistical modeling and optimization of heterogeneous Fenton-like removal of organic pollutant using fibrous catalysts: a full factorial design. Scientific Reports 10(1): 16133.

Mousavi, S. M., E. S. Mostafavi and P. Jiao (2017). Next generation prediction model for daily solar radiation on horizontal surface using a hybrid neural network and simulated annealing method. Energy conversion and management 153: 671-682.

Nayak, R., L. C. Jain and B. K. H. Ting (2001). Artificial Neural Networks in Biomedical Engineering: A Review. Computational Mechanics–New Frontiers for the New Millennium. S. Valliappan and N. Khalili. Oxford, Elsevier: 887-892.

Nuchitprasittichai, A. and S. Cremaschi (2013). An algorithm to determine sample sizes for optimization with artificial neural networks. AIChE Journal 59(3): 805-812.

Pan, G., P. Ye and P. Wang (2014). A Novel Latin hypercube algorithm via translational propagation. The Scientific World Journal 2014: 163949-163949.

Panerati, J., M. A. Schnellmann, C. Patience, G. Beltrame and G. S. Patience (2019). Experimental methods in chemical engineering: Artificial neural networks–ANNs. The Canadian Journal of Chemical Engineering 97(9): 2372-2382.

Park, J.-S. (1994). Optimal Latin-hypercube designs for computer experiments. Journal of Statistical Planning and Inference 39(1): 95-111.

Pholdee, N. and S. Bureerat (2015). An efficient optimum Latin hypercube sampling technique based on sequencing optimisation using simulated annealing. International Journal of Systems Science 46(10): 1780-1789.

Roussouly, N., F. Petitjean and M. Salaun (2013). A new adaptive response surface method for reliability analysis. Probabilistic Engineering Mechanics 32: 103-115.

Shahin, M. A., M. B. Jaksa and H. R. Maier (2008). State of the art of artificial neural networks in geotechnical engineering. Electronic Journal of Geotechnical Engineering 8(1): 1-26.

Sheikholeslami, R. and S. Razavi (2017). Progressive Latin Hypercube Sampling: An efficient approach for robust sampling-based analysis of environmental models. Environmental Modelling & Software 93: 109-126.

Simpson, T. W., J. D. Poplinski, P. N. Koch and J. K. Allen (2001). Metamodels for Computer-based Engineering Design: Survey and recommendations. Engineering with Computers 17(2): 129-150.

Tahkola, M., J. Keränen, D. Sedov, M. F. Far and J. Kortelainen (2020). Surrogate Modeling of Electrical Machine Torque Using Artificial Neural Networks. IEEE Access 8: 220027-220045.

Vaklieva-Bancheva, N. G., R. K. Vladova and E. G. Kirilova (2019). Simulation of heat-integrated autothermal thermophilic aerobic digestion system operating under uncertainties through artificial neural network. Chemical Engineering Transactions 76: 325-330.

van Dam, E. R., B. Husslage, D. den Hertog and H. Melissen (2007). Maximin Latin Hypercube Designs in Two Dimensions. Operations Research 55(1): 158-169.

Veljković, V. B., A. V. Veličković, J. M. Avramović and O. S. Stamenković (2018). Modeling of biodiesel production: Performance comparison of Box–Behnken, face central composite and full factorial design. Chinese Journal of Chemical Engineering.

Viana, F. A. C., G. Venter and V. Balabanov (2010). An algorithm for fast optimal Latin hypercube design of experiments. International Journal for Numerical Methods in Engineering 82(2): 135-156.

Villa Montoya, A. C., R. C. da Silva Mazareli, T. P. Delforno, V. B. Centurion, V. M. de Oliveira, E. L. Silva and M. B. A. Varesche (2020). Optimization of key factors affecting hydrogen production from coffee waste using factorial design and

metagenomic analysis of the microbial community. International Journal of Hydrogen Energy 45(7): 4205-4222.

Wang, C. and Z. Luo (2022). A Review of the Optimal Design of Neural Networks Based on FPGA. Applied Sciences 12 DOI: 10.3390/app122110771.

Wang, G. G. (2003). Adaptive Response Surface Method Using Inherited Latin Hypercube Design Points. Journal of Mechanical Design 125(2): 210-220.

Ye, K. Q., W. Li and A. Sudjianto (2000). Algorithmic construction of optimal symmetric Latin hypercube designs. Journal of Statistical Planning and Inference 90(1): 145-159.

Zendehboudi, S., N. Rezaei and A. Lohi (2018). Applications of hybrid models in chemical, petroleum, and energy systems: A systematic review. Applied energy 228: 2539-2566.

Zorzetto, L. F. M., R. Maciel Filho and M. Wolf-Maciel (2000). Processing modelling development through artificial neural networks and hybrid models." Computers & Chemical Engineering 24(2-7): 1355-1360

มหาวิทยาลัยเทคโนโลยีสุรนารี

CHAPTER VI
CONCLUSIONS AND RECOMMENDATIONS

6.1 Conclusions

This dissertation presents a thorough investigation of the optimization of carbon dioxide adsorption in a fixed bed column with longan seed-derived activated carbon, with particular attention to the effects of alkali loading (NaOH) and mesoporosity. In addition, GCMC simulation was employed to gain insight into the role of alkali on adsorption performance of activated carbon. Finally a new adaptive sampling technique was proposed for studying the simulation-based optimization problems. Conclusions from the present work can be drawn as follows.

The dynamic adsorption of carbon dioxide in fixed bed columns using microporous- and mesoporous-activated carbons impregnated with sodium hydroxide solution was covered in Chapter 2. It was discovered that the key parameters that enhanced the adsorption capacity of CO_2 were the proportional amounts of micropores and mesopores, and the addition of proper amount of the alkali into activated carbon. Empirical correlations were developed through the response surface methods (RSM) to correlate the CO_2 adsorption capacity with the process variables that led to the determination of optimum alkali loading for maximum adsorption capacity.

Chapter 3 expanded on the investigation of CO_2 adsorption by characterizing various activated carbons and assessing their response to NaOH impregnation. Emphasizing the critical role of pore size distribution, the impact of NaOH loading on porous properties and CO_2 adsorption capacity was studied using GCMC. The micropores of activated carbon rapidly decreased after being impregnated with NaOH. However, the pore size distribution of mesoporous-activated carbon can enhance the CO_2 adsorption capacity after being impregnated with the proper amount of NaOH. Micropores were found to be crucial for CO_2 adsorption, while mesopores influenced molecular diffusion within the carbon structure.

In Chapter 4, different process configurations for methanol production via

carbon dioxide hydrogenation were compared, employing Latin hypercube sampling and artificial neural networks for optimization. The findings demonstrated that a configuration of methanol production with two reactors in series offered the most cost-effective solution. This finding indicate the importance of process optimization for sustainable chemical production.

Finally, Chapter 5 proposed an adaptive Latin hypercube sampling method for simulation-based optimization problems. By iteratively refining the sampling strategy based on output deviation, the algorithm exhibited superior efficiency in obtaining optimal solutions with fewer sample points. It was successfully applied to optimization problems with complexity that involve three to five studied factors.

6.2 Recommendations

6.2.1 The Proper Amount of Micropores and Mesopores

The influence of relative amounts of micropores and mesopores in activated carbon on maximizing CO_2 adsorption should be further investigated experimentally using activated carbons prepared by the OTA method from various biomass precursors. Furthermore, the OTA method can be extended to prepare activated carbon with optimum pore size distributions for accommodating the possible maximum amount of NaOH active sites to enhance the CO_2 adsorption capacity.

6.2.2 Applying Adaptive LHS Approach to Advanced Surrogate Model Techniques

For future work, it is recommended to compare the performance of this adaptive LHS approach with other adaptive sampling techniques or advanced surrogate model techniques. Implementing Bayesian optimization to enhance the optimization method is suggested. Performance tests that incorporate various adaptive sampling criteria, such as distance, space-filling metrics, gradient information, and prediction uncertainty, can be applied to the algorithm. Furthermore, the results have demonstrated that as the number of samples increased, the solution converged to the true optimal solution. To enhance the performance of the algorithm, convergence guarantees can be further implemented.

6.2.3 Comparison of the Adaptive LHS Approach with Other Sequential Sampling and Application to More Complex Problems

To assess the performance of the current algorithm and establish its generalizability, it should compared to incremental Latin Hypercube Sampling (LHS), which was developed by Nuchitprasittichai and Cremaschi (2013), for ANN-based optimization. However, it is important to note that the incremental Latin Hypercube Sampling applied to more complex problems involving six and seven decision variables. To comprehensively compare the performance of both methods, it is recommended to apply the current algorithm to optimization problems with higher dimensionality.

6.2.4 Application of Adaptive LHS to Various Fields of Study

The application of the proposed algorithm should be extended to different fields of study, such as engineering design, materials discovery, etc. Additionally, it is essential to study the limitations of ANNs, particularly in terms of their consistency during the training process.

มหาวิทยาลัยเทคโนโลยีสุรนารี

APPENDIX A

SUPPLEMENTARY INFORMATION

มหาวิทยาลัยเทคโนโลยีสุรนารี

CHAPTER IV – PROCESS CONFIGURATION STUDIES OF METHANOL PRODUCTION VIA CARBON DIOXIDE HYDROGENATION: PROCESS SIMULATION-BASED OPTIMIZATION USING ARTIFICIAL NEURAL NETWORKS

A.1 The detailed simulation of the once-through reactor methanol production

HYSYS Documentation

The decision variables in this case are

Pressure of the equilibrium reactor (ERV-100): 70 bar

Temperature of the equilibrium reactor (ERV-100): 190°C

Temperature of cooler (E-101): 60°C

Fluid package: Peng Robinson

Component: CO_2, Hydrogen, Methanol, CO, H_2O

Reactions:

Set-1

Rxn-1 Type: Equilibrium	Stoich Coeff
CO_2	-1
H_2O	1
Methanol	1
Hydrogen	-3
Rxn-2 Type: Equilibrium	Stoich Coeff
CO	-1
Methanol	1
Hydrogen	-2
Rxn-3 Type: Equilibrium	Stoich Coeff
CO_2	-1
CO	1

Methanol 1

Hydrogen -1

Streams:

Hydrogen

Composition Mole fraction

Hydrogen 1.0000

Temperature = 25°C

Pressure = 20 bar

Carbon dioxide

Composition Mole fraction

CO_2 1.0000

Temperature = 40°C

Pressure = 20 bar

Compressed feed (decision variable)

Pressure = 70 bar

Heated feed (decision variable)

Temperature = 190°C

Water_in

Composition Mole fraction

H_2O 1.0000

Temperature = 20°C

Pressure = 1 bar

Water_out

Composition Mole fraction

H_2O 1.0000

Temperature = 35°C

Pressure = 1 bar

Cooled product (decision variable)

Temperature = 60°C

Vessel:

ERV-100

Reaction Set: Set-1

มหาวิทยาลัยเทคโนโลยีสุรนารี

Towers:

T-100

Number of stages: 10

Inlet Stream

Stream: Cooled product (decision variable)

Inlet Stage: 5_Main Tower

Condenser: Full Reflux

Condenser Pressure = 4 bar

Condenser Delta P = 0 bar

Reboiler Pressure = 4 bar

Reboiler Delta P = 0 bar

Specifications:

Condenser Temperature = 25°C

Reflux Ratio = 0.6

T-101

Number of stages: 10

Inlet Stream

Stream: Methanol-water

Inlet Stage: 5_Main Tower

Condenser: Total

Condenser Pressure = 4 bar

Condenser Delta P = 0 bar

Reboiler Pressure = 4 bar

Reboiler Delta P = 0 bar

Specifications:

Comp Fraction

Stage: Condenser

Flow Basis: Mole Fraction

Phase: Liquid

Spec Value: 0.9950

Component: Methanol

Reflux Ratio = 30

มหาวิทยาลัยเทคโนโลยีสุรนารี

Heat Exchanger:

For all heat exchangers:

Heat Exchanger Model: Simple Weighted

Tube Side Dalta P = 0 bar

Shell Side Delta P = 0 bar

Mixer:

MIX-100

Feed

Composition	Mole fraction
Hydrogen	0.7500
CO_2	0.2500

A.2 The detailed simulation of the methanol production with a recycle

HYSYS Documentation

The decision variables in this case are

Pressure of the equilibrium reactor (ERV-100): 70 bar

Temperature of the equilibrium reactor (ERV-100): 190°C

Temperature of a separator (E-101): 60°C

Recycle ratio (RCY-1): 1

Fluid package: Peng Robinson

Component: CO_2, Hydrogen, Methanol, CO, H_2O

Reactions:

Set-1

Rxn-1 Type: Equilibrium	Stoich Coeff
CO_2	-1
H_2O	1
Methanol	1
Hydrogen	-3
Rxn-2 Type: Equilibrium	**Stoich Coeff**
CO	-1
Methanol	1

มหาวิทยาลัยเทคโนโลยีสุรนารี

Hydrogen	-2
Rxn-3 Type: Equilibrium	Stoich Coeff
CO_2	-1
CO	1
Methanol	1
Hydrogen	-1

Streams:

Hydrogen

Composition Mole fraction

Hydrogen 1.0000

Temperature = 25°C

Pressure = 20 bar

Carbon dioxide

Composition Mole fraction

CO_2 1.0000

Temperature = 40°C

Pressure = 20 bar

Compressed feed (decision variable)

Pressure = 70 bar

Heated feed (decision variable)

Temperature = 190°C

Water_in

Composition Mole fraction

H_2O 1.0000

Temperature = 20°C

Pressure = 1 bar

Water_out

Composition Mole fraction

H_2O 1.0000

Temperature = 35°C

Pressure = 1 bar

Cooled product (decision variable)

มหาวิทยาลัยเทคโนโลยีสุรนารี

Temperature = 60°C

<u>Vessel:</u>

ERV-100

Reaction Set: Set-1

<u>Towers:</u>

T-100

Number of stages: 10

Inlet Stream

Stream: Cooled product (decision variable)

Inlet Stage: 5_Main Tower

Condenser: Full Reflux

Condenser Pressure = 4 bar

Condenser Delta P = 0 bar

Reboiler Pressure = 4 bar

Reboiler Delta P = 0 bar

Specifications:

Condenser Temperature = 25°C

Reflux Ratio = 0.6

T-101

Number of stages: 10

Inlet Stream

Stream: Methanol-water

Inlet Stage: 5_Main Tower

Condenser: Total

Condenser Pressure = 4 bar

Condenser Delta P = 0 bar

Reboiler Pressure = 4 bar

Reboiler Delta P = 0 bar

Specifications:

Comp Fraction

Stage: Condenser

มหาวิทยาลัยเทคโนโลยีสุรนารี

Flow Basis: Mole Fraction

Phase: Liquid

Spec Value: 0.9950

Component: Methanol

Reflux Ratio = 30

<u>Heater:</u>

Inlet Stream: Mixed feed

Outlet: Heated feed

Delta P: 0 bar

<u>Heat Exchanger:</u>

For all heat exchangers:

Heat Exchanger Model: Simple Weighted

Tube Side Dalta P = 0 bar

Shell Side Delta P = 0 bar

<u>Mixer:</u>

MIX-100

Feed

Composition	Mole fraction
Hydrogen	0.7500
CO_2	0.2500

MIX-101

Mixed feed

Composition	Mole fraction
Hydrogen	0.8053
CO_2	0.1886
CO	0.0013
Methanol	0.0039
H_2O	0.0009

MIX-102

Combined product

Composition	Mole fraction
Hydrogen	0.0025

มหาวิทยาลัยเทคโนโลยีสุรนารี

CO_2	0.0154
CO	0.0000
Methanol	0.4911
H_2O	0.4910

TEE:

TEE-100

Split Fraction

To recycle = 1.00

To mixer = 0.00

Recycle:

RCY-1

Inlet Stream: To recycle

Outlet Stream: Recycle

Valves:

VLV-101

Inlet stream: To mixer

Outlet stream:

Pressure = 4 bar

VLV-102

Inlet stream: Liquid_product

Outlet stream

Pressure = 4 bar

มหาวิทยาลัยเทคโนโลยีสุรนารี

A.3 The detailed simulation of the methanol production with two reactors in series

HYSYS Documentation

The decision variables in this case are

Pressure of the first equilibrium reactor (ERV-100): 70 bar

Temperature of the first equilibrium reactor (ERV-100): 190°C

Temperature of a separator after the first equilibrium reactor (E-101): 60°C

Pressure of the second equilibrium reactor (ERV-101): 140 bar

Outlet temperature of the liquid stream cooler after the second equilibrium reactor: 60°C

Fluid package: Peng Robinson

Component: CO_2, Hydrogen, Methanol, CO, H_2O

Reactions:

Set-1

Rxn-1 Type: Equilibrium	Stoich Coeff
CO_2	-1
H_2O	1
Methanol	1
Hydrogen	-3
Rxn-2 Type: Equilibrium	**Stoich Coeff**
CO	-1
Methanol	1
Hydrogen	-2
Rxn-3 Type: Equilibrium	**Stoich Coeff**
CO_2	-1
CO	1
Methanol	1
Hydrogen	-1

Streams:

Hydrogen

Composition	Mole fraction
Hydrogen	1.0000

Temperature = 25°C

Pressure = 20 bar

Carbon dioxide

Composition	Mole fraction
CO_2	1.0000

Temperature = 40°C

Pressure = 20 bar

Compressed feed (decision variable)

มหาวิทยาลัยเทคโนโลยีสุรนารี

Pressure = 70 bar

Heated feed (decision variable)

Temperature = 190°C

Water_in_E-101

Composition	Mole fraction
H_2O	1.0000

Temperature = 20°C

Pressure = 1 bar

Water_out_E-101

Composition	Mole fraction
H_2O	1.0000

Temperature = 35°C

Pressure = 1 bar

Water_in_E-102

Composition	Mole fraction
H_2O	1.0000

Temperature = 20°C

Pressure = 1 bar

Water_out_E-102

Composition	Mole fraction
H_2O	1.0000

Temperature = 80°C

Pressure = 1 bar

Water_in_E-103

Composition	Mole fraction
H_2O	1.0000

Temperature = 20°C

Pressure = 1 bar

Water_out_E-103

Composition	Mole fraction
H_2O	1.0000

Temperature = 40°C

มหาวิทยาลัยเทคโนโลยีสุรนารี

Pressure = 1 bar

Cooled product (decision variable)

Temperature = 60°C

Cooled_vapor_product

Temperature = 190°C

Cooled_vapor_product

Temperature = 190°C

Vessel:

ERV-100

Reaction Set: Set-1

ERV-101

Reaction Set: Set-1

Towers:

T-100

Number of stages: 10

Inlet Stream

Stream: Cooled product (decision variable)

Inlet Stage: 5_Main Tower

Condenser: Full Reflux

Condenser Pressure = 4 bar

Condenser Delta P = 0 bar

Reboiler Pressure = 4 bar

Reboiler Delta P = 0 bar

Specifications:

Condenser Temperature = 25°C

Reflux Ratio = 0.6

T-101

Number of stages: 10

Inlet Stream

Stream: Methanol-water

Inlet Stage: 5_Main Tower

มหาวิทยาลัยเทคโนโลยีสุรนารี

Condenser: Total

Condenser Pressure = 4 bar

Condenser Delta P = 0 bar

Reboiler Pressure = 4 bar

Reboiler Delta P = 0 bar

Specifications:

Comp Fraction

Stage: Condenser

Flow Basis: Mole Fraction

Phase: Liquid

Spec Value: 0.9950

Component: Methanol

Reflux Ratio = 30

<u>Heater:</u>

Inlet Stream: Mixed feed

Outlet: Heated feed

Delta P: 0 bar

<u>Heat Exchanger:</u>

For all heat exchangers:

Heat Exchanger Model: Simple Weighted

Tube Side Dalta P = 0 bar

Shell Side Delta P = 0 bar

<u>Mixer:</u>

MIX-100

Feed

Composition	Mole fraction
Hydrogen	0.7500
CO_2	0.2500

MIX-101

Mixed_product

Composition	Mole fraction
Hydrogen	0.0041

มหาวิทยาลัยเทคโนโลยีสุรนารี

CO_2	0.0145
CO	0.0000
Methanol	0.5116
H_2O	0.4698

MIX-102

Purge

Composition	Mole fraction
Hydrogen	0.9966
CO_2	0.0001
CO	0.0000
Methanol	0.0030
H_2O	0.0003

<u>Valves:</u>

VLV-100

Inlet stream: Liquid_product

Outlet stream

Pressure = 4 bar

VLV-101

Inlet stream: Liquid_product3

Outlet stream

Pressure = 4 bar

VLV-102

Inlet stream: Liquid_product4

Outlet stream

Pressure = 4 bar

มหาวิทยาลัยเทคโนโลยีสุรนารี

A.4 An artificial neural network with eight nodes for the once-through methanol production

Table A.1 Mean square errors of training ANN

Data set	MSE
Training	6.88E-05
Validation	2.71E-03
Testing	1.01E-03

Table A.2 Weight of hidden layer, $W1_{rn}$

Neurons	Input nodes		
	1	2	3
1	0.01838	-1.70034	-1.20367
2	-1.68858	1.95475	0.00519
3	-0.08469	2.77145	-2.02880
4	-0.27928	3.05352	0.98175
5	1.21379	-2.16699	0.51323
6	-0.87896	-1.12092	2.95081
7	-0.94691	-0.92281	2.73080
8	1.99345	0.69224	1.74543

Table A.3 Weight of output layer, $W2_r$

Neurons	Output node
1	-0.22146
2	-1.71827
3	0.08519
4	-0.06928
5	-0.14825
6	0.73373

Table A.3 Weight of output layer, $W2_r$ (continued)

Neurons	Output node
7	-0.64427
8	0.03067

Table A.4 Bias of input layer, $B1_r$

Neurons	Output node
1	-3.47132
2	2.46352
3	0.92364
4	-0.04140
5	1.52651
6	-1.48586
7	-1.48669
8	2.84496

Bias of output layer = 0.62038

A.5 An artificial neural network with eight nodes for the methanol production with a recycle

Table A.5 Mean square errors of training ANN

Data set	MSE
Training	8.72E-21
Validation	1.16E-02
Testing	1.42E-03

Table A.6 Weight of hidden layer, $W1_{rn}$

Neurons	Input nodes			
	1	2	3	4
1	-1.00968	1.73126	-0.10196	0.75399
2	1.11953	-0.31624	1.09309	1.26681

Table A.6 Weight of hidden layer, $W1_{rn}$ (continued)

Neurons	Input nodes			
	1	2	3	4
3	-1.42018	-1.63466	-1.01587	-0.06575
4	0.11041	-0.09164	0.17686	-0.41533
5	-1.86229	3.54757	-0.26787	-1.78728
6	-1.88872	0.45065	-2.79983	-1.75360
7	-0.82886	0.56948	-0.12020	-1.32130
8	-1.94827	-1.58476	1.28377	-1.77149

Table A.7 Weight of output layer, $W2_r$

Neurons	Output node
1	-2.80948
2	-1.15408
3	0.61432
4	0.20542
5	-1.10762
6	-1.68792
7	-1.05462
8	2.49677

Table A.8 Bias of input layer, $B1_r$

Neurons	Output node
1	-2.80948
2	-1.15408
3	0.61432
4	0.20542
5	-1.10762
6	-1.68792
7	-1.05462
8	2.49677

มหาวิทยาลัยเทคโนโลยีสุรนารี

Bias of output layer = -0.33351

A.6 An artificial neural network with eight nodes for the methanol production with two reactors in series

Table A.9 Mean square errors of training ANN

Data set	MSE
Training	4.71E-03
Validation	1.62E-02
Testing	7.21E-03

Table A.10 Weight of hidden layer, $W1_{rn}$

Neurons	Input nodes				
	1	2	3	4	5
1	1.6740	0.8355	0.9769	0.3482	1.0151
2	0.9246	0.1406	-0.9624	-1.6217	-0.9027
3	1.0726	-0.0086	-0.3173	1.4694	0.9207
4	-0.4479	0.2063	-1.2073	1.4524	1.1261
5	0.8234	-1.2615	-0.4674	0.2023	-1.9366
6	0.1548	-0.3474	-0.0050	-0.6043	-0.1140
7	-1.2164	0.1393	-1.5386	-0.1769	-1.3954
8	0.9263	-0.9053	1.4689	0.3428	-0.4674

Table A.11 Weight of output layer, $W2_r$

Neurons	Output node
1	-0.23179
2	0.09440
3	-0.04781
4	0.11484
5	0.15391
6	-1.20436

Table A.11 Weight of output layer, $W2_r$ (continued)

Neurons	Output node
7	0.15647
8	0.13893

Table A.12 Bias of input layer, $B1_r$

Neurons	Output node
1	-2.70132
2	-1.22765
3	-1.84862
4	0.22289
5	0.09772
6	0.36272
7	-1.60834
8	2.25577

Bias of output layer = -0.08487

มหาวิทยาลัยเทคโนโลยีสุรนารี

CHAPTER V – ADAPTIVE LATIN HYPERCUBE SAMPLING FOR SURROGATE-BASED OPTIMIZATION WITH ARTIFICIAL NEURAL NETWORK

A.7 The detailed simulation of ammonia production from syngas

HYSYS Documentation

The decision variables in this case are:

Reformer temperature: 900°C

Combuster temperature: 1400°C

Low temperature conversion reactor temperature (LTC): 160°C

Fluid package: Peng-Robinson

Component: Methane, Ethane, Propane, i-Butane, n-Butane, Nitrogen, CO, CO_2, H_2O, Oxygen, Hydrogen, Ammonia, Methanol

Reactions:

Set-1

Rxn-1 Type: Equilibrium	Stoich Coeff
Methane	-1
H_2O	-1
CO	1
Hydrogen	3
Rxn-2 Type: Equilibrium	Stoich Coeff
Ethane	-1
H_2O	-2
CO	2
Hydrogen	5
Rxn-3 Type: Equilibrium	Stoich Coeff
Propane	-1
H_2O	-3
CO	3
Hydrogen	7
Rxn-4 Type: Equilibrium	Stoich Coeff

i-Butane	-1
H_2O	-4
CO	4
Hydrogen	9
Rxn-5 Type: Equilibrium	Stoich Coeff
n-Butane	-1
H_2O	-4
CO	4
Hydrogen	9

Set-2

Rxn-1 Type: Equilibrium	Stoich Coeff
CO	-2
Oxygen	-1
CO_2	2
Rxn-2 Type: Equilibrium	Stoich Coeff
Hydrogen	-2
Oxygen	-1
H_2O	2
Rxn-3 Type: Equilibrium	Stoich Coeff
Methane	-1
Oxygen	-2
H_2O	2
CO_2	1
Rxn-4 Type: Equilibrium	Stoich Coeff
Ethane	-2
Oxygen	-7
H_2O	6
CO_2	4
Rxn-5 Type: Equilibrium	Stoich Coeff
Propane	-1
Oxygen	-5
H_2O	4

มหาวิทยาลัยเทคโนโลยีสุรนารี

CO_2	3

Set-3

Rxn-1 Type: Equilibrium	Stoich Coeff
CO	-1
Hydrogen	-3
Methane	1
H_2O	1

Rxn-2 Type: Equilibrium	Stoich Coeff
CO_2	-1
Hydrogen	-4
Methane	1
H_2O	2

Set-4

Rxn-1 Type: Kinetic	Stoich Coeff
Ammonia	2
Hydrogen	-3
Nitrogen	-1

Set-5

Rxn-1 Type: Equilibrium	Stoich Coeff
CO	-1
H_2O	-1
CO_2	1
Hydrogen	1

<u>Streams:</u>

HPSteam

Composition	Mole fraction
H_2O	1.0000

Temperature = 350°C

Pressure = 120 bar

NaturalGas

Composition	Mole fraction
Methane	0.9575

มหาวิทยาลัยเทคโนโลยีสุรนารี

Ethane	0.0267
Propane	0.0065
i-Butane	0.0010
n-Butane	0.0011
Nitrogen	0.0072

Temperature = 25°C

Pressure = 35 bar

Air

Composition	Mole fraction
Nitrogen	0.7900
Oxygen	0.2100

Temperature = 800°C

Pressure = 35 bar

Reformer_Feed (decision variable)

Temperature = 900°C

Combuster_Feed (decision variable)

Temperature = 1400°C

W_in_1

Composition	Mole fraction
H_2O	1.0000

Temperature = 25°C

Pressure = 1 bar

W_out_1

Composition	Mole fraction
H_2O	1.0000

Temperature = 80°C

Pressure = 1 bar

WSGR1_Feed

Temperature = 450°C

W_in_2

Composition Mole fraction

มหาวิทยาลัยเทคโนโลยีสุรนารี

H_2O 1.0000

Temperature = 25°C

Pressure = 1 bar

W_out_2

Composition Mole fraction

H_2O 1.0000

Temperature = 80°C

Pressure = 1 bar

WSGR2_Feed (decision variable)

Temperature = 160°C

W_in_3

Composition Mole fraction

H_2O 1.0000

Temperature = 25°C

Pressure = 1 bar

W_out_3

Composition Mole fraction

H_2O 1.0000

Temperature = 80°C

Pressure = 1 bar

Separator1_Feed

Temperature = 100°C

Methanizer_Feed

Temperature = 340°C

W_in_5

Composition Mole fraction

H_2O 1.0000

Temperature = 25°C

Pressure = 1 bar

W_out_5

Composition Mole fraction

H_2O 1.0000

มหาวิทยาลัยเทคโนโลยีสุรนารี

Temperature = 80°C

Pressure = 1 bar

Separator2_Feed

Temperature = 40°C

Make-up N2

Composition	Mole fraction
Nitrogen	1.0000

Temperature = 0°C

Pressure = 140 bar

Molar Flow = 1000 kgmole/hr

ComP1_out

Pressure = 80 bar

W_in_6

Composition	Mole fraction
H_2O	1.0000

Temperature = 25°C

Pressure = 1 bar

W_out_6

Composition	Mole fraction
H_2O	1.0000

Temperature = 80°C

Pressure = 1 bar

Cool2_out

Temperature = 90°C

ComP2_out

Pressure = 150 bar

W_in_7

Composition	Mole fraction
H_2O	1.0000

Temperature = 25°C

Pressure = 1 bar

W_out_7

มหาวิทยาลัยเทคโนโลยีสุรนารี

Composition Mole fraction

H_2O 1.0000

Temperature = 80°C

Pressure = 1 bar

Separator3_Feed

Temperature = 40°C

Feed_1

Temperature = 450°C

W_in_9

Composition Mole fraction

H_2O 1.0000

Temperature = 25°C

Pressure = 1 bar

W_out_9

Composition Mole fraction

H_2O 1.0000

Temperature = 80°C

Pressure = 1 bar

Product_separator

Vapor-Phase Fraction = 1.0000

Recycle

Temperature = 20°C

LN2_in

Composition Mole fraction

Nitrogen 1.0000

Temperature = -196.2°C

Pressure = 1 bar

LN2_out

Composition Mole fraction

Nitrogen 1.0000

Temperature = -80°C

Pressure = 1 bar

มหาวิทยาลัยเทคโนโลยีสุรนารี

Liquid_to_separator

Temperature = -45°C

Vessel:

Reformer

Reaction Set: Set-1

Combuster

Reaction Set: Set-2

HTC

Reaction Set: Set-5

LTC

Reaction Set: Set-5

Methanizer

Reaction Set: Set-3

For all plug flow reactors

Reaction Set: Set-4

Heater:

E-100

Inlet Stream: Feed

Outlet: Reformer_Feed

Delta P: 0 bar

E-113

Inlet Stream: Heated_re_pro

Outlet: Combuster_Feed

Delta P: 0 bar

E-104

Inlet Stream: SynGas_Flow

Outlet: Methanizer_Feed

Delta P: 0 bar

Heat Exchanger:

For all heat exchangers:

Heat Exchanger Model: Simple Weighted

มหาวิทยาลัยเทคโนโลยีสุรนารี

Tube Side Dalta P = 0 bar

Shell Side Delta P = 0 bar

Mixer:

MIX-100

Feed

Composition	Mole fraction
Methane	0.2522
Ethane	0.0070
Propane	0.0017
i-Butane	0.0003
n-Butane	0.0003
Nitrogen	0.0019
H_2O	0.7366

MIX-101

Heated_re_pro

Composition	Mole fraction
Methane	0.0326
Nitrogen	0.1192
CO	0.1294
H_2O	0.3066
Oxygen	0.0314
Hydrogen	0.3809

MIX-102

Feed_ammonia

Composition	Mole fraction
Methane	0.0147
Nitrogen	0.6462
H_2O	0.0005
Hydrogen	0.3319
Ammonia	0.0066

MIX-103

32

มหาวิทยาลัยเทคโนโลยีสุรนารี

Composition	Mole fraction
Methane	0.0012
Nitrogen	0.2585
H_2O	0.0027
Hydrogen	0.7376

MIX-104

Feed_2

Composition	Mole fraction
Methane	0.0189
Nitrogen	0.6882
H_2O	0.0006
Ammonia	0.2922

MIX-105

Feed_3

Composition	Mole fraction
Methane	0.0190
Nitrogen	0.6887
H_2O	0.0006
Ammonia	0.2917

<u>TEE:</u>

TEE-100

Split Fraction

Quench1 = 0.9950

Quench2 = 0.0025

Quench3 = 0.0025

TEE-101

Split Fraction

Purge = 0.0100

Product to liquid = 0.9900

<u>Recycle:</u>

RCY-3

Inlet Stream: N2_to_Recycle

มหาวิทยาลัยเทคโนโลยีสุรนารี

Outlet Stream: N2_recycle

A.8 The detailed simulation of methanol production with a recycle

HYSYS Documentation

The decision variables in this case are:

Pressure of the equilibrium reactor (ERV-100): 70 bar

Temperature of the equilibrium reactor (ERV-100): 190°C

Temperature of a separator (E-101): 60°C

Recycle ratio (RCY-1): 1

Fluid package: Peng Robinson

Component: CO_2, Hydrogen, Methanol, CO, H_2O

Reactions:

Set-1

Rxn-1 Type: Equilibrium	Stoich Coeff
CO_2	-1
H_2O	1
Methanol	1
Hydrogen	-3
Rxn-2 Type: Equilibrium	**Stoich Coeff**
CO	-1
Methanol	1
Hydrogen	-2
Rxn-3 Type: Equilibrium	**Stoich Coeff**
CO_2	-1
CO	1
Methanol	1
Hydrogen	-1

Streams:

Hydrogen

Composition	Mole fraction
Hydrogen	1.0000

Temperature = 25°C

Pressure = 20 bar

Carbon dioxide

Composition	Mole fraction
CO_2	1.0000

Temperature = 40°C

Pressure = 20 bar

Compressed feed (decision variable)

Pressure = 70 bar

Heated feed (decision variable)

Temperature = 190°C

Water_in

Composition	Mole fraction
H_2O	1.0000

Temperature = 20°C

Pressure = 1 bar

Water_out

Composition	Mole fraction
H_2O	1.0000

Temperature = 35°C

Pressure = 1 bar

Cooled product (decision variable)

Temperature = 60°C

<u>Vessel:</u>

ERV-100

Reaction Set: Set-1

<u>Towers:</u>

T-100

Number of stages: 10

Inlet Stream

Stream: Cooled product (decision variable)

Inlet Stage: 5_Main Tower

มหาวิทยาลัยเทคโนโลยีสุรนารี

Condenser: Full Reflux

Condenser Pressure = 4 bar

Condenser Delta P = 0 bar

Reboiler Pressure = 4 bar

Reboiler Delta P = 0 bar

Specifications:

Condenser Temperature = 25°C

Reflux Ratio = 0.6

T-101

Number of stages: 10

Inlet Stream

Stream: Methanol-water

Inlet Stage: 5_Main Tower

Condenser: Total

Condenser Pressure = 4 bar

Condenser Delta P = 0 bar

Reboiler Pressure = 4 bar

Reboiler Delta P = 0 bar

Specifications:

Comp Fraction

Stage: Condenser

Flow Basis: Mole Fraction

Phase: Liquid

Spec Value: 0.9950

Component: Methanol

Reflux Ratio = 30

<u>Heater:</u>

Inlet Stream: Mixed feed

Outlet: Heated feed

Delta P: 0 bar

<u>Heat Exchanger:</u>

For all heat exchangers:

มหาวิทยาลัยเทคโนโลยีสุรนารี

Heat Exchanger Model: Simple Weighted

Tube Side Dalta P = 0 bar

Shell Side Delta P = 0 bar

Mixer:

MIX-100

Feed

Composition	Mole fraction
Hydrogen	0.7500
CO_2	0.2500

MIX-101

Mixed feed

Composition	Mole fraction
Hydrogen	0.8053
CO_2	0.1886
CO	0.0013
Methanol	0.0039
H_2O	0.0009

MIX-102

Combined product

Composition	Mole fraction
Hydrogen	0.0025
CO_2	0.0154
CO	0.0000
Methanol	0.4911
H_2O	0.4910

TEE:

TEE-100

Split Fraction

To recycle = 1.00

To mixer = 0.00

Recycle:

RCY-1

Inlet Stream: To recycle

Outlet Stream: Recycle

Valves:

VLV-101

Inlet stream: To mixer

Outlet stream:

Pressure = 4 bar

VLV-102

Inlet stream: Liquid_product

Outlet stream

Pressure = 4 bar

A.9 The detailed simulation of CO_2 absorption by methanol via Rectisol process

HYSYS Documentation

The decision variables in this case are:

Lean methanol temperature: -25.0°C

The 3rd stage separator pressure: 1.2 bar

Stripper reflux ratio: 5

Stripper inlet temperature: 40°C

Distillation reflux ratio: 1

Fluid package: PRSV

Component: Methanol, CO_2, Ammonia, CO, Argon, Nitrogen, Hydrogen, H_2O, Methane

Streams:

Syngas Feed

Composition	Mole fraction
CO_2	0.4590
Ammonia	0.0001
CO	0.0052
Argon	0.0085
Nitrogen	0.4923

Hydrogen 0.0272

H_2O 0.0027

Methane 0.0050

Temperature = 18.30°C

Pressure = 17.24 bar

Lean Methanol

Composition Mole fraction

Methanol 0.9998

H_2O 0.0002

Temperature (decision variable) = -25°C

Pressure = 17.20 bar

5F (decision variable)

Temperature = 40°C

Methanol

Composition Mole fraction

Methanol 1.0000

Temperature = 21 °C

Pressure = 1.1 bar

NH-3

Composition Mole fraction

Ammonia 1.0000

Temperature = -70°C

Pressure = 1 bar

NH-4

Composition Mole fraction

Ammonia 1.0000

Temperature = -50°C

Pressure = 1 bar

<u>Towers:</u>

Absorber

Number of stages: 15

Inlet Stream

มหาวิทยาลัยเทคโนโลยีสุรนารี

Stream: 5B-3

Inlet Stage: 15_Main Tower

Top Stage Inlet: Lean Methanol

Stripper

Number of stages: 10

Inlet Stream

Stream: 5F (decision variable)

Inlet Stage: 10_Main Tower

Stream: 3C-3 (decision variable)

Inlet Stage: 11_Main Tower

Condenser: Full Reflux

Condenser Pressure = 1.1 bar

Condenser Delta P = 0 bar

Reboiler Pressure = 1.1 bar

Reboiler Delta P = 0 bar

Specifications:

Comp Ratio = 0.9500

Reflux Ratio (decision variable) = 5

Distillation

Number of stages: 12

Inlet Stream

Stream: 2

Inlet Stage: 5_Main Tower

Condenser: Full Reflux

Condenser Pressure = 3.4 bar

Condenser Delta P = 0 bar

Reboiler Pressure = 3.4 bar

Reboiler Delta P = 0 bar

Specifications:

Comp Ratio = 0.99

Reflux Ratio (decision variable) = 1

<u>Heat Exchanger:</u>

มหาวิทยาลัยเทคโนโลยีสุรนารี

For all heat exchangers:

Heat Exchanger Model: Simple Weighted

Tube Side Dalta P = 0 bar

Shell Side Delta P = 0 bar

<u>Mixer:</u>

MIX-100

6A-7

Composition	Mole fraction
Methanol	0.9999
H_2O	0.0001

MIX-101

1B

Composition	Mole fraction
Methanol	0.1862
CO_2	0.2004
Ammonia	0.0002
CO	0.0036
Argon	0.0041
Nitrogen	0.3376
Hydrogen	0.2593
H_2O	0.0029
Methane	0.0059

MIX-102

4H

Composition	Mole fraction
Methanol	0.0146
CO_2	0.9476
Ammonia	0.0008
CO	0.0001
Argon	0.0006
Nitrogen	0.0344
Hydrogen	0.0001

มหาวิทยาลัยเทคโนโลยีสุรนารี

Methane 0.0019

TEE:

TEE-100

Split Fraction

6C = 0.9400

6D-1 = 0.0600

Valve:

VLV-100

Inlet stream: 3A

Outlet stream: 2

Pressure =3.4 bar

VLV-101

Inlet stream: 5C

Outlet stream: 5C-2

Pressure = 4.5 bar

VLV-102

Inlet stream: 5A

Outlet stream: 5A-2

Pressure = 10.5 bar

VLV-103

Inlet stream: 5D

Outlet stream: 5D-2

Pressure = 4.5 bar (decision variable)

Recycle:

RCY-1

Inlet Stream: 5B

Outlet Stream: 5B-2

RCY-2

Inlet Stream: 6D-1

Outlet Stream: 6D

RCY-3

Inlet Stream: 6E-1

Outlet Stream: Lean Methanol

RCY-4

Inlet Stream: 3C-2

Outlet Stream: 3C

มหาวิทยาลัยเทคโนโลยีสุรนารี

Table A.13 Final data set of case study 1: ammonia production from syngas

Sample no.	Decision variables			Response
	x_1	x_2	x_3	Ammonia production cost
1	1153.47	1522.43	190.06	576.03
2	989.12	1467.24	281.62	556.63
3	1164.99	1672.82	254.31	648.00
4	1124.42	1567.96	202.96	588.94
5	922.86	1406.41	205.68	505.25
6	1048.96	1547.33	264.13	585.45
7	1037.08	1505.91	167.29	549.42
8	1016.11	1603.51	162.43	583.59
9	976.84	1690.36	196.72	621.42
10	1095.54	1455.63	223.08	548.77
11	933.05	1417.36	173.66	506.26
12	906.22	1653.35	228.98	607.52
13	1189.02	1576.66	287.31	632.67
14	1180.29	1593.89	219.19	611.34
15	971.01	1620.26	245.53	599.96
16	1135.40	1495.11	270.62	583.39
17	1007.10	1665.00	271.47	633.36
18	1061.01	1536.71	248.98	577.83
19	1100.68	1481.80	184.73	552.14
20	955.61	1628.75	211.49	595.98
21	1074.02	1433.58	234.38	538.25
22	1121.60	1567.94	201.16	588.01
23	1114.70	1564.07	198.40	585.01
24	900.00	1432.03	160.00	507.48
25	1007.20	1666.77	275.99	636.49
26	1006.64	1659.79	272.91	631.79
27	900.00	1400.00	183.04	497.62
28	996.40	1468.40	283.43	559.07
29	990.83	1459.03	278.79	552.75
30	900.00	1400.00	177.05	497.13

มหาวิทยาลัยเทคโนโลยีสุรนารี

Table A.14 Final data set of case study 2: methanol production via carbon dioxide hydrogenation

Sample no.	Decision variables				Response
	x_1	x_2	x_3	x_4	Methanol production cost
1	68.43	201.98	62.00	0.6046	1618.57
2	57.86	201.15	65.57	0.1721	2898.02
3	55.86	193.07	70.48	0.1395	2760.07
4	53.27	191.74	79.37	0.4834	2001.59
5	58.77	194.46	74.66	0.9282	1090.09
6	57.50	207.15	67.57	0.5387	2084.13
7	52.28	208.60	67.01	0.0128	4381.01
8	59.75	202.47	77.17	0.0714	3133.65
9	52.09	202.88	78.28	0.8561	1330.76
10	63.86	194.20	72.25	0.4568	1836.09
11	50.06	200.68	64.56	0.3766	2663.30
12	63.43	206.21	61.16	0.8169	1329.13
13	66.12	196.73	76.52	0.3568	2020.91
14	54.46	209.62	71.58	0.5097	2337.28
15	60.69	190.78	78.95	0.7016	1416.77
16	62.18	196.04	60.13	0.8650	1182.66
17	50.88	198.26	70.79	0.3058	2758.26
18	61.03	190.33	66.12	0.6630	1475.46
19	64.87	203.78	76.19	0.9625	1042.72
20	53.93	199.99	63.15	0.1054	3290.48
21	66.77	198.71	69.36	0.6396	1534.88
22	69.29	207.04	68.78	0.4074	2073.98
23	67.25	208.23	75.44	0.2771	2465.39
24	61.46	205.53	73.76	0.2200	2757.53
25	56.66	195.45	63.60	0.7194	1493.37
26	65.43	197.38	68.18	0.9656	1023.04
27	55.05	204.88	62.47	0.1968	3153.04
28	68.94	192.66	73.35	0.7778	1239.14

มหาวิทยาลัยเทคโนโลยีสุรนารี

Table A.14 Final data set of case study 2: methanol production via carbon dioxide hydrogenation (continued)

Sample no.	Decision variables				Response
	x_1	x_2	x_3	x_4	Methanol production cost
29	52.70	209.22	66.89	0.0189	4355.37
30	52.44	208.65	66.68	0.0089	4386.29
31	70.00	190.00	80.00	1.0000	942.45
32	56.17	193.42	70.66	0.1289	2784.44
33	55.83	193.07	70.06	0.1238	2801.24
34	68.41	204.98	60.00	1.0000	1002.55
35	55.54	204.82	62.81	0.2136	3063.39
36	55.20	204.34	62.14	0.1939	3127.63
37	70.00	190.00	70.96	1.0000	950.13
38	52.02	203.43	78.36	0.8399	1375.90
39	51.43	203.04	78.12	0.8220	1423.52
40	70.00	207.99	76.01	1.0000	989.75
41	52.46	208.82	66.99	0.0167	4359.64
42	52.27	208.64	66.90	0.0026	4435.38
43	65.91	191.32	80.00	1.0000	952.13
44	68.48	201.93	61.83	0.6047	1617.03
45	68.11	201.56	61.67	0.5767	1667.13
46	67.24	194.77	60.00	1.0000	972.79

มหาวิทยาลัยเทคโนโลยีสุรนารี

Table A.15 Final data set of case study 3: CO_2 absorption by methanol via Rectisol process

Sample no.	Decision variables					Response
	x_1	x_2	x_3	x_4	x_5	Capture cost
1	-49.23	1.229	8.771	16.72	6.136	112.46
2	-23.43	1.606	6.422	22.06	9.323	117.24
3	-46.37	1.479	16.311	26.65	9.631	176.00
4	-52.99	1.939	5.777	26.26	4.232	98.36
5	-43.91	1.304	9.989	27.30	5.244	105.41
6	-35.83	1.734	11.425	33.87	6.573	122.39
7	-29.26	1.774	16.645	29.45	5.769	136.68
8	-20.29	1.630	5.076	29.81	3.585	72.66
9	-25.61	1.724	15.599	31.89	9.765	154.00
10	-33.49	1.407	14.172	14.41	2.664	102.97
11	-26.56	1.499	14.933	37.13	1.862	90.03
12	-47.20	1.701	12.639	11.87	8.579	163.88
13	-36.66	1.753	15.806	38.20	7.604	151.40
14	-51.74	1.209	8.156	21.18	2.375	85.44
15	-21.51	1.571	19.422	28.41	2.183	115.72
16	-45.17	1.360	11.636	23.43	4.487	112.75
17	-54.88	1.318	6.779	32.88	8.186	117.28
18	-27.94	1.908	17.157	25.36	5.035	139.27
19	-28.85	1.545	10.494	34.67	6.920	109.08
20	-40.91	1.453	13.837	13.33	1.080	102.48
21	-41.45	1.405	19.922	31.09	6.322	156.90
22	-22.28	1.876	8.943	19.14	2.952	90.87
23	-37.87	1.639	9.499	15.73	8.247	129.13
24	-39.25	1.285	10.769	35.07	7.702	116.51
25	-32.00	1.967	18.855	24.06	3.465	145.87
26	-50.41	1.909	14.659	17.47	5.441	169.91
27	-31.20	1.999	7.858	14.24	4.605	100.30
28	-48.86	1.858	17.927	39.68	6.867	189.42
29	-30.46	1.260	6.016	20.01	3.300	70.23

Table A.15 Final data set of case study 3: CO_2 absorption by methanol via Rectisol process (continued)

Sample no.	Decision variables					Response
	x_1	x_2	x_3	x_4	x_5	Capture cost
30	-42.96	1.542	13.111	18.21	3.837	121.05
31	-53.77	1.450	13.157	10.62	8.903	170.07
32	-38.17	1.811	7.449	20.61	7.288	114.72
33	-44.51	1.678	12.252	36.21	9.039	151.20
34	-34.99	1.339	18.361	11.32	1.331	110.01
35	-24.48	1.821	17.773	38.30	1.602	110.28
36	-48.02	1.858	18.145	39.71	6.791	188.79
37	-48.63	1.844	17.895	39.53	6.679	187.08
38	-31.21	1.200	5.000	33.95	1.000	46.35
39	-28.21	1.560	10.533	34.84	7.057	110.19
40	-28.71	1.549	10.237	34.10	7.031	109.09
41	-20.00	1.200	5.000	23.67	1.000	52.59
42	-54.08	1.337	6.945	33.02	8.083	117.89
43	-54.86	1.322	6.803	32.38	8.018	116.86
44	-35.74	1.200	5.000	33.89	1.000	47.83
45	-34.31	1.351	18.645	11.61	1.513	112.37
46	-34.72	1.346	18.324	10.94	1.279	110.24
47	-20.00	1.281	5.000	39.31	1.000	46.12
48	-40.07	1.474	13.826	13.09	1.129	102.81
49	-40.84	1.455	13.619	12.96	1.042	99.59
50	-26.47	1.280	5.000	40.00	1.000	43.95
51	-24.38	1.829	17.729	38.81	1.694	111.06
52	-24.87	1.827	17.530	38.38	1.617	109.80
53	-37.16	1.511	5.000	40.00	1.000	50.04

A.10 Weights and biases of an artificial neural networks for training the data set of random sampling.

A.10.1 Case study 1: Ammonia production from syngas

Table A.16 Mean square errors of training ANN

Data set	MSE
Training	1.52E-05
Validation	1.19E-04
Testing	4.52E-05

Table A.17 Weight of hidden layer, $W1_m$

Neurons	Input nodes		
	1	2	3
1	-2.3682	0.6228	0.5254
2	-0.1803	-0.0498	-1.3409
3	0.1440	0.2659	-0.0401
4	-1.4446	1.7557	0.5200
5	-0.1177	0.1200	0.4391
6	-1.3274	0.0407	-1.3057
7	-0.2760	-1.7613	0.0743
8	2.0677	-1.8151	-0.6159

มหาวิทยาลัยเทคโนโลยีสุรนารี

Table A.18 Weight of output layer, $W2_r$

Neurons	Output node
1	-0.0416
2	-0.3629
3	2.3181
4	0.0745
5	0.8902
6	-0.0186
7	-0.0540
8	-0.1241

Table A.19 Bias of input layer, $B1_r$

Neurons	Output node
1	2.3922
2	1.3427
3	-0.2083
4	-0.3426
5	1.4267
6	-0.1934
7	-1.8252
8	2.5504

Bias of output layer = 0.0129

มหาวิทยาลัยเทคโนโลยีสุรนารี

A.10.2 Case study 2: Methanol production via carbon dioxide hydrogenation

Table A.20 Mean square errors of training ANN

Data set	MSE
Training	3.20E-07
Validation	8.24E-06
Testing	4.61E-06

Table A.21 Weight of hidden layer, $W1_{rn}$

Neurons	Input nodes			
	1	2	3	4
1	0.9948	0.6365	-0.1825	-0.1942
2	0.3067	0.2540	-0.2935	-2.6807
3	-0.9732	1.3545	1.0360	-1.0357
4	0.7542	-0.6835	0.0090	-0.7380
5	0.0794	-0.0215	-0.0181	0.7138
6	1.0944	-0.9190	0.0708	-0.6277
7	-0.2468	0.2019	-0.0045	-0.4551
8	-1.1972	0.5411	-0.0324	-1.2129

Table A.22 Weight of output layer, $W2_r$

Neurons	Output node
1	0.0225
2	0.0272
3	-0.0055
4	0.0792
5	-0.3989
6	0.1319
7	2.1486
8	0.2470

มหาวิทยาลัยเทคโนโลยีสุรนารี

Table A.23 Bias of input layer, $B1_r$

Neurons	Output node
1	-0.8868
2	2.1283
3	1.4075
4	0.2115
5	-0.1466
6	1.9636
7	-1.0273
8	-2.7433

Bias of output layer = 1.3462

A.10.3 Case study 3: CO_2 absorption by methanol via Rectisol process

Table A.24 Mean square errors of training ANN

Data set	MSE
Training	2.85E-05
Validation	5.50E-05
Testing	4.22E-05

Table A.25 Weight of hidden layer, $W1_{rn}$

Neurons	Input nodes				
	1	2	3	4	5
1	-1.1612	0.4267	0.6170	0.0776	-0.0070
2	-2.0083	-0.0265	-0.0583	0.0438	-0.1383
3	0.0076	0.0483	-0.0250	0.0230	-0.1016
4	-0.1773	0.2575	0.0805	0.0104	-0.0002
5	2.2137	0.0507	0.0991	-0.0537	0.1723
6	0.1480	-0.3700	0.1323	-0.0025	-0.0004
7	-0.6150	0.1493	-0.2343	0.0470	0.0128
8	-1.7773	0.5226	2.2852	0.3430	-0.1023

มหาวิทยาลัยเทคโนโลยีสุรนารี

Table A.26 Weight of output layer, $W2_r$

Neurons	Output node
1	0.3551
2	-0.8543
3	-3.6878
4	2.6417
5	-0.6012
6	1.1263
7	-1.2372
8	-0.0256

Table A.27 Bias of input layer, $B1_r$

Neurons	Output node
1	-1.5419
2	1.4949
3	-0.0233
4	-0.2838
5	-1.4584
6	0.6507
7	-1.7367
8	-2.5763

Bias of output layer = -0.9123

มหาวิทยาลัยเทคโนโลยีสุรนารี

A.11 Weights and biases of an artificial neural networks for training the data set of adaptive Latin hypercube sampling.

A.11.1 Case study 1: Ammonia production from syngas

Table A.28 Mean square errors of training ANN

Data set	MSE
Training	9.92E-07
Validation	2.85E-04
Testing	6.46E-04

Table A.29 Weight of hidden layer, $W1_{rn}$

Neurons	Input nodes		
	1	2	3
1	0.7357	-1.3657	2.1587
2	-2.0546	-0.9905	-1.7479
3	2.0853	0.3863	1.8296
4	1.6385	2.1145	0.0074
5	1.9052	-1.9173	-1.3953
6	1.7018	-2.2192	-0.4386
7	1.0337	1.9477	-0.0395
8	-2.0165	1.2170	0.9853

มหาวิทยาลัยเทคโนโลยีสุรนารี

Table A.30 Weight of output layer, $W2_r$

Neurons	Output node
1	-0.0577
2	-0.2594
3	-0.0703
4	0.3227
5	-0.1809
6	-0.0355
7	0.4293
8	0.2925

Table A.31 Bias of input layer, $B1_r$

Neurons	Output node
1	-2.9187
2	2.0097
3	-1.4948
4	-0.6331
5	-0.1269
6	1.0142
7	2.1234
8	-3.1478

Bias of output layer = 0.1989

มหาวิทยาลัยเทคโนโลยีสุรนารี

A.11.2 Case study 2: methanol production via carbon dioxide hydrogenation

Table A.32 Mean square errors of training ANN

Data set	MSE
Training	3.06E-08
Validation	1.29E-04
Testing	1.02E-05

Table A.33 Weight of hidden layer, $W1_{rn}$

Neurons	Input nodes			
	1	2	3	4
1	-0.3066	-1.5063	-0.9558	0.7309
2	1.0728	-0.4369	0.0888	-1.6636
3	0.0529	-0.0215	0.0344	1.5948
4	0.4170	-1.7917	-0.8440	-1.9836
5	1.4311	-1.3899	1.1017	0.9473
6	-0.2295	0.2196	0.0183	-0.9931
7	2.1562	-0.3368	-0.8320	1.2068
8	-0.9796	0.7576	-0.3045	-1.2917

Table A.34 Weight of output layer, $W2_r$

Neurons	Output node
1	-0.0626
2	-0.0206
3	-0.2198
4	0.0139
5	-0.0210
6	0.7670
7	-0.0847
8	0.6752

มหาวิทยาลัยเทคโนโลยีสุรนารี

Table A.35 Bias of input layer, $B1_r$

Neurons	Output node
1	-2.9615
2	-0.4146
3	-0.9196
4	0.5101
5	1.2467
6	-0.7789
7	3.0020
8	-3.3325

Bias of output layer = 0.6054

มหาวิทยาลัยเทคโนโลยีสุรนารี

A.11.3 Case study 3: CO_2 absorption by methanol via Rectisol process

Table A.36 Mean square errors of training ANN

Data set	MSE
Training	1.32E-04
Validation	4.27E-04
Testing	2.33E-03

Table A.37 Weight of hidden layer, $W1_{rn}$

Neurons	Input nodes				
	1	2	3	4	5
1	-2.0167	0.7220	-0.6211	-0.7957	-1.0699
2	-0.0506	0.3918	-0.0145	-1.3910	1.2934
3	-1.0740	0.0579	1.1195	-0.2202	-0.1242
4	0.4088	-0.3947	0.7916	0.9237	-1.1863
5	1.7848	-0.5047	-0.3678	1.4842	1.2589
6	0.2225	0.4808	0.9969	-0.0013	0.7223
7	0.3278	0.1813	0.4486	1.1427	-0.6860
8	-1.0223	0.9647	1.4222	0.1476	0.2411

Table A.38 Weight of output layer, $W2_r$

Neurons	Output node
1	-0.3738
2	0.2561
3	0.4370
4	-0.2361
5	0.1715
6	0.2842
7	0.0372
8	0.3227

มหาวิทยาลัยเทคโนโลยีสุรนารี

Table A.39 Bias of input layer, $B1_r$

Neurons	Output node
1	2.9622
2	-2.1864
3	0.0097
4	-0.7930
5	0.4856
6	0.7373
7	2.5068
8	-1.8019

Bias of output layer = 0.5801

มหาวิทยาลัยเทคโนโลยีสุรนารี

APPENDIX B

ESTIMATION OF EQUIPMENT COSTS

มหาวิทยาลัยเทคโนโลยีสุรนารี

For cost estimation, the cost includes cost capital and operating costs. These costs are determined through the estimation and data from the capital equipment-costing program.

The capital cost is estimated using the module costing technique. This technique depends on the following:

- The specific equipment type
- The specific system pressure
- The specific material of construction

B.1 Calculation of the total module cost

The total module cost can be evaluated from

$$C_{TM} = \sum_{i=1}^{n} C_{TM,i} = 1.18 \sum_{i=1}^{n} C_{BM,i} \quad \text{(B.1)}$$

B.2 Calculation of the bare module cost

$$C_{BM} = C_p^0 F_{BM} = C_p^0 \left[B_1 + B_2 F_P F_M\right] \quad \text{(B.2)}$$

where C_{BM} is the bare module equipment cost

F_{BM} is the bare module cost factor

C_p^0 is the purchased cost for base conditions

$$\log_{10} C_p^0 = K_1 + K_2 \log_{10}(A) + K_3 \left(\log_{10}(A)\right)^2 \quad \text{(B.3)}$$

where A is the capacity or size parameter for the equipment

Table B.1 The values of based equipment cost parameters of each equipment

Equipment	K_1	K_2	K_3
Compressor	2.2897	1.3604	-0.1027
Condenser	4.8306	-0.8509	0.3187
Reboiler	4.3247	-0.3030	0.1634
Vertical vessel	3.4974	0.4485	0.1074
Horizontal vessel	3.5565	0.3776	0.0905
Tower	3.4974	0.4485	0.1074
Packing	2.4493	0.9744	0.0055
Trays	2.9949	0.4465	0.3961

The pressure, F_p, is obtained from

$$\log_{10} F_p = C_1 + C_2 \log_{10} P + C_3 \left(\log_{10} P\right)^2 \quad \text{(B.4)}$$

Foe vessel

$$F_{P,vessel} = \frac{\frac{(P+1)D}{2[850-0.6(P+1)]} + 0.00315}{0.0063} \text{ for } t_{vessel} > 0.0063 \text{ m} \quad \text{(B.5)}$$

where P is the pressure in barg

Table B.2 The values of bare module cost parameters of each equipment

Equipment	C_1	C_2	C_3	B_1	B_2	F_M	F_{BM}
Compressor	0	0	0	-	-	-	2.7
Condenser P < 5	0	0	0	1.63	1.66	1.8	-
5 < P < 140	0.03881	-0.11272	0.08183	1.63	1.66	1.8	-
Reboiler P < 5	0	0	0	1.63	1.66	1.8	-
5 < P < 140	0.03881	-0.11272	0.08183	1.63	1.66	1.8	-
Vertical vessel	-	-	-	2.25	1.82	3.1	
Horizontal vessel	-	-	-	2.25	1.82	3.1	
Tower	-	-	-	2.25	1.82	3.1	
Packing	0	0	0	-	-	-	7.1
Trays	0	0	0	-	-	-	1.8

APPENDIX C

LIST OF PUBLICATIONS

มหาวิทยาลัยเทคโนโลยีสุรนารี

LIST OF PUBLICATIONS

1. International Publications

Borisut, P. and A. Nuchitprasittichai (2019). Methanol Production via CO_2 Hydrogenation: Sensitivity Analysis and Simulation-Based Optimization. Frontiers in Energy Research 7(81).

Borisut, P. and A. Nuchitprasittichai (2020). Process Configuration Studies of Methanol Production via Carbon Dioxide Hydrogenation: Process Simulation-Based Optimization Using Artificial Neural Networks. Energies 13(24).

Tangsathitkulchai, C., S. Naksusuk, A. Wongkoblap, P. Phadungbut and **P. Borisut** (2021). Equilibrium and Kinetics of CO_2 Adsorption by Coconut Shell Activated Carbon Impregnated with Sodium Hydroxide. Processes 9(2).

Borisut, P. and A. Nuchitprasittichai (2023). Adaptive Latin Hypercube Sampling for a Surrogate-Based Optimization with Artificial Neural Network. Processes 11(11).

Borisut, P., C. Tangsathitkulchai and A. Nuchitprasittichai (2024). Dynamic of CO_2 adsorption in a fixed bed of microporous and mesoporous activated carbon impregnated with sodium hydroxide and the application of response surface methodology (RSM) for determining optimal adsorption conditions. Environmental Science and Pollution Research.

2. Conference Proceeding

Borisut, P. and A. Nuchitprasittichai (2020). Optimization of Methanol Production via Carbon Dioxide Hydrogenation: Comparison of Sampling Techniques for Process Modeling. IOP Conference Series: Materials Science and Engineering.

มหาวิทยาลัยเทคโนโลยีสุรนารี

BIOGRAPHY

Prapatsorn Borisut was born on June 7, 1996, in Ranong province, Thailand. She attended Sriyapai School for her high school education and graduated in 2014. She then pursued a Bachelor of Engineering in Chemical Engineering at Suranaree University of Technology in Nakhon Ratchasima, graduating with First Class Honors in July 2018. After completing her undergraduate studies, Prapatsorn enrolled in the graduate school of Chemical Engineering at Suranaree University of Technology, where she worked under the supervision of Dr. Aroonsri Nuchitprasittichai and Dr. Chaiyot Tangsathitkulchai. She was awarded a scholarship from the Royal Golden Jubilee Ph.D. Program (RJG-Ph.D.) through the National Research Council of Thailand (NRCT). Her Ph.D. research focused on the adsorption of carbon dioxide using longan-seed activated carbon and the development of an adaptive sampling technique for simulation-based optimization. During her Ph.D. program, Prapatsorn joined the Department of Chemical Engineering at Auburn University in Alabama, USA, as a visiting scholar from June 2023 to May 2024. Under the supervision of Dr. Selen Cremaschi, she worked on incorporating an optimization algorithm into process simulations using the Aspen process simulator. Prapatsorn successfully defended her doctoral dissertation in June 2024.

มหาวิทยาลัยเทคโนโลยีสุรนารี